# Precipitation Analysis in Microalloyed X70 Steels and Heat Treated L80 and T95 Steels

by

Corentin Chatelier

A thesis submitted in partial fulfillment of the requirements for the degree of

Master of Science

in
Materials Engineering

Department of Chemical and Materials Engineering
University of Alberta

## Abstract

Microalloyed steels and heat treated steels are widely used in the pipeline industry. Microalloyed steels are a type of high strength low alloy steels containing small additions of C, N, Nb, Ti and other elements in amounts less than 0.1 wt%. They may also contain additions of other elements in amounts exceeding 0.1 wt%, such as Mo or Cr. Precipitation of secondary phases has a significant contribution to the overall steel properties and is dependent on steel composition and processing conditions. Changing the steel composition or processing conditions noticeably affects precipitation and therefore affects steel properties. For example, recently thicker wall pipes are being produced. It is legitimate to wonder how this change in design affects precipitation.

Because of the small sizes and low volume fractions, conventional techniques, such as electron microscopy, are not suitable to characterize precipitates in steels. Alternative techniques, such as matrix dissolution methods combined with quantitative X-ray diffraction (QXRD) analysis, have to be used. These techniques allow for collection of a statistically significant amount of precipitates. In this thesis, scanning electron microscopy (SEM) is used to characterize 2 X70 microalloyed steels and 3 heat treated steels. Matrix dissolution techniques are used and

improved to extract precipitates from the steels. QXRD analysis is done on the extracted precipitates to quantify the relative abundance of precipitates, compositions and size distributions. Energy-dispersive X-ray spectroscopy (EDX) analysis is also done to confirm the QXRD analysis. In addition, a model of NbC precipitation during laminar cooling is developed to predict volume fraction and particle size distribution of nanoscale precipitates. The effect of X70 pipe wall thickness on precipitation is discussed and the experimental results are compared to NbC precipitation simulation results. The volume fraction of large precipitates (1 to 4 μm) appears to be twice as high in thick walled X70 steel than the thinner X70 steel. The HCl solution was not successful for extracting Cr and most of the Mo based precipitates for the heat treated steels. Meanwhile, the mathematical model of NbC precipitates showed reasonable trends with the nanoprecipitates (<5 nm) extracted in the microalloyed steels.

## Acknowledgments

I would like to thank and acknowledge my supervisors Pr. H. Henein and Pr. D.G. Ivey for their support and guidance throughout my research project. I would also like to thank Dr. Wiskel for his advice and counsel on my analyses.

I would also like to thank all the members of the AMPL research group for their support and friendship over the past two years: Kartik, Justin, William, Antoine, Patrick, Dylan, Mohsen, and of course, Aziz and Jonas. My thanks also to Dr. Laurie Collins of EVRAZ NA for the discussions on my research.

I would like to extend my thanks to EVRAZ NA Inc. and TransCanada Pipeline for their financial sponsorship of this work along with the Natural Sciences and Engineering Research Council (NSERC) of Canada.

Finally, I would like to thank my familly along with my friends back in France, for their distant encouragement and constant support. It would have been much more difficult without all of them.

# Contents

**1 Introduction** **1**

1.1 Statement of the problem . . . . . 1

1.2 Relevance of precipitation . . . . . 2

1.3 Objectives . . . . . 3

1.4 Outline . . . . . 4

**2 Literature review** **5**

2.1 Microalloyed steels, heat treated steels, Q&T and TMCP . . . . . 5

2.2 Types of precipitates in steels . . . . . 8

2.3 Strengthening mechanisms . . . . . 11

2.4 Precipitate characterization . . . . . 12

2.4.1 Scanning and transmission electron microscopy (SEM and TEM) . . . . . 12

2.4.2 Atom probe tomography . . . . . 12

2.4.3 Small angle neutron scattering . . . . . 13

2.4.4 Matrix dissolution . . . . . 13

2.4.5 X-ray diffraction – Rietveld refinement (QXRD) . . . . . 14

2.5 NbC precipitation modeling . . . . . 14

2.5.1 Thermodynamic data available . . . . . 15

2.5.2 Different approaches . . . 15
2.5.3 Validation of the methods . . . 16
2.6 Summary . . . 17

**3 Experimental procedures** **19**
3.1 Steels analyzed . . . 19
3.2 Microstructure analysis . . . 21
3.3 Chemical dissolution . . . 21
3.3.1 Experimental set-up . . . 22
3.3.2 Modification of Lu's set-up . . . 23
3.3.3 Centrifuge process . . . 23
3.4 ICP analysis of supernatant solution . . . 24
3.5 XRD analysis of the precipitates . . . 25
3.5.1 XRD Measurements . . . 25
3.5.2 Rietveld refinement and QXRD analysis . . . 26
3.6 SEM-EDX analysis of collected precipitates . . . 28
3.7 Error analysis . . . 29

**4 Modeling of NbC precipitation kinetics during laminar cooling** **31**
4.1 Lagrange "Multipreci" approach . . . 31
4.2 Assumptions . . . 32
4.3 Classical nucleation theory . . . 33
4.3.1 Nucleation . . . 33
4.3.2 Growth . . . 34

4.3.3 Coarsening . . . 36
4.4 Input parameters . . . 36
4.5 Laminar cooling parameters . . . 36
4.6 Numerical resolution . . . 38
4.6.1 Nucleation . . . 38
4.6.2 Growth and dissolution . . . 39
4.6.3 Timestep . . . 40
4.7 Results . . . 40
4.7.1 Lu's steels [2] . . . 41
4.7.2 Conventional and thick wall X70 steels . . . 41
4.8 Summary . . . 42

**5 X70 and TWX70 steels** **45**

5.1 Microstructural analysis - grain size measurement . . . 46
5.1.1 SEM secondary electron (SE) imaging analysis . . . 46
5.1.2 EBSD analysis . . . 47
5.1.3 Mean linear intercept measurements . . . 47
5.2 Chemical dissolution of the steel matrix . . . 48
5.3 ICP measurements . . . 48
5.3.1 X70 steel . . . 49
5.3.2 TWX70 steel . . . 50
5.3.3 ICP summary . . . 50
5.4 SEM-EDX analysis of the collected precipitates . . . 51

5.4.1 X70 steel . . . . . 52

5.4.2 TWX70 steel . . . . . 54

5.5 X-ray diffraction of the extracted precipitates . . . . . 57

5.5.1 X70 . . . . . 57

5.5.2 TWX70 . . . . . 58

5.5.3 XRD analysis summary . . . . . 58

5.6 Rietveld refinement and QXRD analysis . . . . . 59

5.6.1 Adaptation of the refinement procedure . . . . . 59

5.6.2 QXRD analysis for X70 steel . . . . . 63

5.6.3 QXRD analysis for TWX70 steel . . . . . 66

5.7 Summary . . . . . 69

**6 L80, ML80 and T95 steels** **70**

6.1 Microstructural analysis and grain size measurements . . . . . 70

6.1.1 SEM analysis . . . . . 70

6.1.2 EBSD analysis . . . . . 72

6.1.3 Mean linear intercept (m.l.i.) measurements . . . . . 73

6.2 Chemical dissolution of steel matrix . . . . . 73

6.3 ICP measurements . . . . . 74

6.3.1 L80 steel . . . . . 74

6.3.2 ML80 steel . . . . . 75

6.3.3 T95 steel . . . . . 76

6.3.4 Summary of ICP analysis . . . . . 77

6.4 SEM-EDX analysis of the extracted precipitates . . . . . 77
6.4.1 L80 steel . . . . . 77
6.4.2 ML80 steel . . . . . 79
6.4.3 T95 steel . . . . . 81
6.5 X-ray diffraction of the extracted precipitates . . . . . 83
6.5.1 L80 steel . . . . . 83
6.5.2 ML80 steel . . . . . 84
6.5.3 T95 steel . . . . . 85
6.5.4 Summary of XRD analysis . . . . . 86
6.6 Rietveld refinement and quantitative XRD analysis . . . . . 86
6.6.1 L80 steel . . . . . 86
6.6.2 ML80 steel . . . . . 89
6.6.3 T95 steel . . . . . 91
6.7 Summary . . . . . 94

**7 Discussion** **96**

7.1 Modification of the dissolution set-up . . . . . 96
7.2 Rietveld refinement 'multi-peaks' technique . . . . . 97
7.3 Precipitate suspension analysis . . . . . 98
7.4 Effect of Mo and Cr on precipitation in heat treated steels . . . . . 98
7.4.1 L80 precipitate analysis . . . . . 98
7.4.2 ML80 precipitate analysis . . . . . 100
7.4.3 T95 precipitate analysis . . . . . 101

7.4.4 Carbide precipitation in Mo-Cr heat treated steels . . . 102

7.5 Effect of wall thickness on precipitation in X70 steels . . . 103

7.5.1 Effect of the thickness on the precipitation of large particles . . . 104

7.5.2 Effect of thickness on nanoprecipitation . . . 105

7.5.3 Discussion of model assumptions . . . 107

7.5.4 Comparison between the simulation and experimental results . . . 108

7.6 Temperature optimization . . . 111

7.7 Summary . . . 113

**8 Conclusions and future work** **114**

8.1 Experimental and computational improvements . . . 114

8.2 Effects of wall thickness and composition . . . 115

8.3 Recommendations and future work . . . 116

8.3.1 Improvements to the model . . . 116

8.3.2 Validation of the model . . . 116

8.3.3 Site specific dissolution . . . 117

8.3.4 Determination of the role of Cr and Mo in precipitation . . . 117

**Bibliography** **118**

**A Modeling of NbC precipitation: python implementation** **124**

**B QXRD Results** **129**

B.1 TWX70 . . . 129

B.2 X70 . . . 130

B.3 L80 . . . . . 131

B.4 T95 . . . . . 132

B.5 Mass balance calculation example . . . . . 133

**C SEM SE images and EDX spectra** **135**

C.1 SEM . . . . . 135

C.2 EDX . . . . . 137

**D ThermoCalc simulations** **141**

# List of Figures

2.1 Schematic of a TMCP schedule [5]. . . . . 6

2.2 Hardness as a function of tempering temperature and (A) carbon content [12] (B) alloying content [14], in different Fe-C alloys. . . . . 8

2.3 Comparison of the solubility products $K_S$ for different carbides and nitrides in austenite and ferrite [1]. . . . . 10

2.4 Comparison of the solubility products $K_S$ for different carbides in austenite and ferrite [23]. . . . . 10

2.5 SANS results and NbC precipitation model results for low-Nb and high-Nb laboratory steels [31]. . . . . 17

3.1 Experimental set-up (schematic and photograph). . . . . 22

3.2 XRD pattern of residues form T95-2 (bubbling $N_2$ ) and T95-3 ($N_2$ atmosphere) . 23

4.1 Laminar cooling temperature profile (centerline of TWX70 steel). . . . . 37

4.2 Nucleation and growth sequence [44]. . . . . 39

4.3 Simulation of the mean radius over time for X70 steel, for different $\Delta$t values: (A) Overall results and (B) zoom. . . . . 40

4.4 Modeling of NbC precipitation during laminar cooling for X70 steel. . . . . 43

4.5 Modeling of NbC precipitation during laminar cooling for TWX70 steel. . . . . 44

5.1 SEM SE images of X70 steel: (A) Lower magnification and (B) higher magnification. 46

5.2 SEM SE images of TWX70 steel: (A) SE image and (B) in-lens SE image. . . . . 46

5.3 EBSD images: (A) X70 steel and (B) TWX70 steel. . . . . 47

5.4 Mean linear intercept for X70 and TWX70 steels. . . . . 48

5.5 ICP results for X70 steel: (A) wt% and (B) relative amounts. . . . . 50

5.6 ICP results for TWX70 steel: (A) wt% and (B) relative amounts. . . . . 51

5.7 SEM SE image of precipitates collected from an X70 steel (TiN in blue, false color). 52

5.8 SEM SE images of precipitates collected from an X70 steel: (A) TiN and (B) suspension (preparation #2). . . . . 53

5.9 X70 steel precipitate size distribution from a total of 82 particles. . . . . 53

5.10 EDX analysis for precipitates extracted from X70 steel. The Nb content of the large precipitates is shown in red and the Mo content is shown in blue. The Nb content of the small precipitates is shown in green and the Mo content is shown in yellow. . . . . 54

5.11 SEM SE images of precipitates collected from TWX70 steel: (A) TiN (in blue, false color) and (B) suspension (preparation #2). . . . . 55

5.12 TWX70 steel precipitate size (particle radii) distribution from a total of 112 particles from preparation #2. . . . . 55

5.13 EDX analysis for precipitates extracted from TWX70 steel. The Nb content of the large precipitates is shown in red and the Mo content is shown in blue. The Nb content of the small precipitates is shown in green and the Mo content is shown in yellow. . . . . 56

5.14 XRD pattern for collected precipitates from X70 steel. . . . . 57

5.15 XRD pattern for collected precipitates from TWX70 steel. . . . . 58

5.16 Part of the XRD pattern for sample X70-2 showing the first set of TiN-rich (111) peaks between $2\theta = 41.9^\circ$ and $2\theta = 42.7^\circ$. . . . . 59

5.17 Step 1 of Rietveld refinement process showing addition of 9 TiN-rich phases evenly spread out between $2\theta = 41.9^\circ$ and $2\theta = 42.7^\circ$. The blue line represents the experimental XRD pattern. The red dots represent the calculated XRD pattern. The ticks below the curves represent the position of each diffraction peak. . . . . 61

5.18 Step 2 of Rietveld refinement process showing refinement of the lattice parameters and scale factors for 9 phases. . . . . 61

5.19 Step 3 of Rietveld refinement process showing refinement of the strain and size parameters for 9 phases. . . . . 62

5.20 Step 4 of Rietveld refinement process showing refinement of the phase compositions for 9 phases. . . . . 62

5.21 QXRD analysis for precipitates in X70 steel. . . . . 63

5.22 Lattice parameters for the precipitates as a function of Ti content for X70 steel. . . 64

5.23 Comparison between ICP and QXRD results for precipitates in X70 steel. . . . . 66

5.24 QXRD analysis for the precipitates in TWX70 steel. . . . . 67

5.25 Lattice parameters for the precipitates as a function of Ti contents for TWX70 steel. 68

5.26 Comparison between ICP and QXRD results for precipitates in TWX70 steel. . . . 69

6.1 SEM SE images of L80 steel: (A) lower and (B) higher magnification. . . . . 71

6.2 SEM SE images of ML80 steel: (A) lower and (B) higher magnification. . . . . 71

6.3 SEM SE images of T95 steel: (A) lower and (B) higher magnification. . . . . 71

6.4 EBSD images for (A) L80, (B) ML80 and (C) T95 steels. . . . . 72

6.5 Mean linear intercept measurements for L80, ML80 and T95 steels. . . . . 73

6.6 ICP results for L80 steel: (A) composition in wt% and (B) relative amounts. . . . 74

6.7 ICP results for ML80 steel: (A) composition in wt% and (B) relative amounts. . . 75

6.8 ICP results for T95 steel: (A) composition in wt% and (B) relative amounts. . . . 76

6.9 SEM SE images of collected precipitates from L80 steel: (A) large TiN particle and (B) nanosize precipitates. . . . . 77

6.10 L80 steel precipitate size (particle radii) distribution from a total of 1526 particles. 78

6.11 EDX analysis for precipitates extracted from L80 steel. The Cr content of the large precipitates is shown in red and the Mo content is shown in blue. The Cr content of the small precipitates is shown in green and the Mo content is shown in yellow. 79

6.12 SEM SE images for collected precipitates from ML80 steel: (A) Agglomerates and (B) suspension sample. . . . . 79

6.13 ML80 steel precipitate size (particle radii) distribution from a total of 1841 particles. The blue curve is the sum of the green and red distributions. . . . . 80

6.14 EDX analysis for precipitates extracted from ML80 steel. The Cr content of the small precipitates is shown in green and the Ti content is shown in yellow. . . . . 80

6.15 SEM SE images of collected precipitates from T95 steel: (A) TiN and (B) suspension sample. . . . . 81

6.16 T95 steel precipitate size (particle radii) distribution from a total of 1414 particles. The blue curve is the sum of the green and red distributions. . . . . 82

6.17 EDX analysis for precipitates extracted from T95 steel. The Cr content of the large precipitates is shown in red and the Mo content is shown in blue. The Cr content of the small precipitates is shown in green and the Mo content is shown in yellow. 83

6.18 XRD pattern for collected precipitates from L80 steel. . . . . 84

6.19 XRD pattern for collected precipitates from ML80 steel. . . . . 85

6.20 XRD pattern for collected precipitates from T95 steel. . . . . 85

6.21 QXRD analysis for collected precipitates from L80 steel. . . . . 87

6.22 Lattice parameters for precipitates as a function of Ti contents for L80 steel. . . . 88

6.23 Comparison between ICP and QXRD results for collected precipitates from L80 steel. . . . 88

6.24 QXRD analysis for collected precipitates from ML80 steel. . . . 89

6.25 Comparison between ICP and QXRD results for ML80 steel. . . . 91

6.26 QXRD analysis for collected precipitates from T95 steel. . . . 92

6.27 Lattice parameters for precipitates as a function of Ti contents for T95 steel. . . . 93

6.28 Comparison between ICP and QXRD results for T95 steel. . . . 94

7.1 Comparison between QXRD and simulation results: (A) Mean radius $R_{mean}$ and (B) volume fraction $f_v$. . . . 109

7.2 Nominal and initial calculated concentrations for X70 and TWX70 steels: (A) wt% Nb and (B) wt% C. . . . 110

7.3 Comparison between QXRD and simulation results: (A) Volume fraction $f_v$ and (B) mean radius $R_{mean}$. . . . 110

7.4 Mean precipitate radius and volume fraction as a function of finish rolling temperature: (A) Volume fraction and (B) mean radius. . . . 111

7.5 Precipitation strengthening as a function of finish rolling temperature. . . . 112

7.6 Precipitation strengthening as a function of coiling interupt temperature. . . . 113

B.1 QXRD analysis for precipitates in TWX70 steel. . . . 129

B.2 QXRD analysis for precipitates in X70 steel. . . . 130

B.3 QXRD analysis for precipitates in X70 steel. . . . 130

B.4 QXRD analysis for precipitates in L80 steel. . . . 131

B.5 QXRD analysis for precipitates in L80 steel. . . . 131

B.6 QXRD analysis for precipitates in T95 steel. . . . . 132

B.7 QXRD analysis for precipitates in T95 steel. . . . . 132

C.1 SEM SE image of a large TiN particle in X70 steel. . . . . 135

C.2 SEM SE image of precipitates collected from L80 steel (TiN precipitates are in blue, oxides particle in are red). . . . . 136

C.3 SEM SE image of small precipitates collected from T95 steel. . . . . 136

C.4 EDX spectrum of an agglomerate of small precipitates from X70 steel. . . . . 137

C.5 EDX spectrum of an agglomerate of small precipitates from TWX70 steel. . . . . 137

C.6 EDX spectrum of an agglomerate of small precipitates from T95 steel. . . . . 138

C.7 EDX spectrum of an agglomerate of small precipitates from ML80 steel. . . . . 138

C.8 EDX spectrum of an agglomerate of small precipitates from L80 steel showing the presence of As and O. . . . . 139

C.9 EDX spectrum of an agglomerate of small precipitates from L80 steel showing the presence of As, Al and O. . . . . 139

C.10 EDX spectrum of an agglomerate of small precipitates from L80 steel showing the presence of Al, Mg and O (one unknown peak at 0.7 keV). . . . . 140

D.1 Phase diagram of the system Fe-Mo-Cr-Ti-C calculated with ThermoCalc for L80 steel. L80 Cr composition is 0.14 wt%. For this composition, (Fe,Mo,Cr,Ti)3C2 phase exists. Database : TCFE6. . . . . 142

D.2 Phase diagram of the system Fe-Mo-Cr-Ti-C calculated with ThermoCalc for ML80 steel. ML80 Cr composition is 0.22 wt%. For this composition, (Cr,Fe,Mo,Ti)C and (Mo,Cr)3C2 phases exist. Database : TCFE6. . . . . 143

D.3 Phase diagram of the system Fe-Mo-Cr-Ti-C calculated with ThermoCalc for T95 steel. T95 Cr composition is 0.9 wt%. For this composition, (Cr,Fe,Mo,Ti)C and (Cr,Mo)3C2 phases exist. Database : TCFE6. . . . . 144

# List of Tables


2.1 Lattice parameters of the main precipitate types. . . . . 9

2.2 Thermodynamic data for NbC in ferrite [43]. . . . . 15

3.1 Steel compositions (wt%) . . . . . 19

3.2 Mechanical properties of the steels studied . . . . . 20

3.3 Dissolution parameters and results for X70, TWX70, L80, ML80 and T95 steels. . 25

3.4 X-ray diffraction data . . . . . 26

4.1 Input parameters [43]. . . . . 37

4.2 Results for Lu's steels [2]. . . . . 41

4.3 Simulation results for the X70 and TWX70 steels. . . . . 41

5.1 Mean linear intercept (m.l.i.) measurements for X70 and TWX70 steels . . . . . 48

5.2 ICP measurements and calculated amount in precipitate form for X70 steel. . . . 49

5.3 ICP measurements and calculated amount in precipitate form for TWX70 steel. . 50

5.4 EDX analysis for large (total of 30 particles) and small (total of 42 agglomerates) precipitates $(Ti_xNb_yMo_{1-x-y})(C,N)$ extracted from X70 steel (values in atomic fraction). . . . . 54

5.5 EDX analysis for large precipitates $(Ti_xNb_yMo_{1-x-y})(C,N)$ from TWX70 steel (total of 29 particles). Values in atomic fraction. . . . . 56

5.6 EDX analysis for small precipitates ($Ti_xNb_yMo_{1-x-y}$)(C,N) from TWX70 steel (total of 37 agglomerates, values in atomic fraction). . . . . 56

5.7 Initial parameters for Rietveld refinement for TiN-rich precipitates from X70-2 sample (values of Ti and Nb contents in atomic fraction). . . . . 60

5.8 QXRD results for precipitates in X70 steel. . . . . 64

5.9 QXRD results for precipitates in TWX70 steel. . . . . 68

6.1 Mean linear intercept results for L80, ML80 and T95 steels. . . . . 73

6.2 ICP measurements and calculated amounts in precipitate form for L80 steel. . . . 74

6.3 ICP measurements and calculated amounts in precipitate form for ML80 steel. . 75

6.4 ICP measurements and calculated amounts in precipitate form for T95 steel. . . . 76

6.5 EDX analysis of large precipitates (total of 25 particles) and small precipitates (total of 18 agglomerates) for L80 steel (values in atomic fraction). . . . . 78

6.6 EDX analysis for small precipitates (total of 18 agglomerates) from ML80 steel (values in atomic fraction). . . . . 81

6.7 EDX analysis for the small precipitates (total of 40 agglomerates) from T95 steel (values in atomic fraction). . . . . 82

6.8 EDX analysis for T95 large precipitates (total of 34 particles). Values in atomic fraction. . . . . 82

6.9 QXRD results for precipitates in L80 steel. . . . . 87

6.10 QXRD results for extracted precipitates in ML80 steel. . . . . 90

6.11 QXRD results for extracted precipitates in T95 steel. . . . . 92

6.12 Nanosize precipitates characteristics for the L80, ML80 and T95 steels. . . . . 95

6.13 Large precipitates characteristics for the L80 and T95 steels. . . . . 95

7.1 Characteristics of precipitates collected from L80 steel. . . . . 99

7.2 Characteristics of precipitates collected from ML80 steel. . . . . 100

7.3 Characteristics of precipitates collected from T95 steel. . . . . 101

7.4 Characteristics of large precipitates in X70 steel. . . . . 104

7.5 Characteristics of large precipitates in TWX70 steel. . . . . 105

7.6 QXRD/SEM nanoscale precipitation summary for X70 and TWX70 steels. . . . . 106

B.1 Data used for X70 mass balance calculations. . . . . 134

B.2 Mass balance calculations for precipitates collected from X70 steel. Only the Nb calculations are shown as an example. . . . . 134

# List of Symbols and Abbreviations

| | |
|---|---|
| **CIT** | Coiling interrupt temperature |
| **EBSD** | Electron Backscatter Diffraction |
| **EDX** | EDX or EDS, Energy-Dispersive X-ray Spectroscopy |
| **FRT** | Finish rolling temperature |
| **ICP** | ICP or ICP-MS, Inductively Coupled Plasma Mass Spectroscopy |
| **m.l.i.** | Mean linear intercept |
| **OM** | Optical Miscrocopy |
| **SANS** | Small Angle Neutron Scattering |
| **SEM** | Scanning Electron Miscrocopy |
| **TMCP** | Thermo-Mechanical Controlled Process |
| **Q&T** | Quench and Temper |
| **QXRD** | Quantitative X-ray Diffraction (Rietveld method) |
| **UTS** | Ultimate tensile strength in MPa |
| **XRD** | X-ray Diffraction |
| **YS** | Yield strength in MPa |

| | |
|---|---|
| $D_X$ | Diffusion coefficient of X in $m^2/s$ |
| %El. | Percentage of elongation |
| HCl | Hydrochloric acic |
| $K_S$ | Solubility product |
| $L_{vol}$ | Crystallite size in nm |
| $M_X$ | Molar mass of X in g/mol |
| $N_0$ | Number of nucleation sites per volume unit |
| $Q_X$ | Activation energy of X in ferrite in kJ/mol |
| $R^*$ | Critical radius in nm |
| $R_0$ | Capillary radius in nm |
| $T_{nr}$ | Non-recrystallization temperature |
| $[X]_o$ | Nominal composition of X in wt% |
| $[X]_{MX}$ | X content in MX form in wt% |
| Z | Zeldovich factor |
| a or (a,b,c) | Lattice parametter in Å |
| c | Dispersion coefficient |
| $f_v$ | Precipitate volume fration |
| $m_{steel}$ | Mass of dissolved steel in g |
| $m_{residues}$ | Mass of collected residues in mg |

| | |
|---|---|
| $v_{NbC}$ | Atomic volume of NbC in atom per cubic meter |
| $w_{\varphi}$ | Relative abundance of $\varphi$ in % |
| wt% | weigth fraction |
| $\alpha - Fe$ | Ferrite |
| $\gamma - Fe$ | Austenite |
| $\gamma$ | Interface energy between NbC and ferrite in $J/m^2$ |
| $\rho$ | Dislocation density in $m/m^3$ |
| $\sigma_{ppt}$ | Precipitation strengthening in MPa |

# Chapter 1

# Introduction

## 1.1 Statement of the problem

Microalloyed steels are a particular subclass of High-Strength Low-Alloy (HSLA) steels where alloying elements such as Nb, Ti, or V are added in small amounts (less than 0.1 wt%) to the steel. These additions improve the properties of the steels (such as strength and weldability) by, for example, refining the microstructure and enhancing precipitation strengthening. Properties such as high strength or corrosion resistance are needed in order to support the transportation of oil and gas over long distances, under extreme temperature and pressure conditions and over the time.

Steelmakers can work on many aspects to improve the above mentioned steel properties such as the alloy composition or thermo-mechanical controlled processing (TMCP). For example in the past few years thicker wall pipes have been produced (17, 19 or even 20 mm thick pipes). A regular X70 steel (pipeline steel with a specified minimum yield strength of 483 MPa or 70 ksi) and a thick wall X70 steel would inherently have about the same strength since both are X70 steels, but the design would be different.

Over the past few years many different heat treated (quench and temper, Q&T) steels have been produced with the aim of improving the corrosion resistance of pipelines. Their main differences lie in the amount of alloying content, i.e. Mn, S, B, Mo and Cr added. For instance, L80 and ML80 (specified minimum yield strength of 550 MPa or 80 ksi) are two heat treated

steels used in sour environments. ML80 is a Mo enriched L80 steel. This addition of Mo has an impact on the steel properties. T95 (specified minimum yield strength of 655 MPa or 95 ksi) is another example of heat treated steel with a high Cr content used in sour services. Modifying the composition of a steel has many consequences on its performance.

## 1.2 Relevance of precipitation

A change in composition or in the processing conditions can affect the onset and kinetics of precipitation and ultimately microstructure refinement and precipitation strengthening which play major roles in the strengthening of a steel. Knowing the morphology of precipitates that are present in the steels gives insight into how precipitation kinetics are affected by changing composition.

The volume fraction of precipitates in microalloyed steels is very low (usually lower than 0.1 wt%), which complicates their characterization. In addition, the size of the precipitates can also be very small (less than 10 nm), which further complicates the analysis. Thus, conventional characterization techniques such as scanning or transmission electron microscopy (SEM or TEM) are not able to provide statistically relevant information on precipitation. No data, i.e, volume fraction or mean precipitate size, is available regarding precipitates in heat treated steels.

The size distribution of precipitates and volume fraction of nanosized precipitates can also be determined using small angle neutron scattering (SANS). However, neither the chemical composition nor the morphology can be determined easily using SANS. Other techniques are thus needed such as quantitative X-ray diffraction (QXRD).

The best way to fully determine the precipitate morphology and composition is to extract the precipitates using matrix dissolution techniques. Following extraction it is easier to characterize the collected particles through microscopy, or even XRD.

## 1.3 Objectives

In light of the aforementioned statements, there are three objectives in the present work.

### 1) Modeling of NbC precipitation during laminar cooling

NbC-rich precipitates are the main types of particles that are relevant in the grain refinement and precipitation strengthening of X70 steels. It is known that they form at the end of TMCP in the final stages of the rolling or during laminar cooling due to their solubility in austenite and ferrite [1]. A first objective of this work is to develop a model to predict the precipitation of NbC-rich particles during this last stage of the processing, i.e., the laminar cooling. The modeling combined with experimental results should help in understanding how processing conditions and composition affect precipitation.

### 2) Effect of wall thickness and/or chemistry on precipitation

The second objective is to apply matrix dissolution techniques to different steels in order to characterize their precipitates. Two X70 steels, 11 mm and 17 mm thick, and three different heat treated steels (L80, ML80 and T95) with three different Mo and Cr contents are analyzed. The objective is to determine how the thickness (which dictates the cooling rate) of the steel affects precipitation in X70 steels, and how the Mo and Cr content affect precipitation in heat treated steels.

### 3) Effect of morphology on microstructures and mechanical properties

Finally, the third objective is to determine the effect of precipitate morphology (size, volume fraction, composition and shape) on the microstructures and mechanical properties in order to understand the consequences of a change in chemistry or processing conditions (linked to precipitation) on macroscale properties.

## 1.4 Outline

Chapter 2 of this thesis presents general information regarding microalloyed and heat-treated steels, the precipitation kinetics and some detailed information concerning precipitate characterization. Chapter 3 presents the experimental procedures used for this study to collect and characterize the precipitates. Chapter 4 covers the modeling of NbC precipitation during laminar cooling and presents some preliminary results. Chapters 5 and 6 present the experimental results respectively for the X70 steels and the heat-treated steels. A discussion section is presented in Chapter 7 detailing the effect of the pipe thickness and composition on the morphology of the precipitates. The last chapter (Chapter 8) presents the conclusions of the study and provides some recommendations for future work.

# Chapter 2

# Literature review

To improve the properties of a steel, steelmakers can play with different characteristics such as steel compositions or processing conditions. Any change in composition or processing conditions will result in changes in precipitation behaviour. Precipitate characterization is the only way to determine the precipitation contribution to the strength of a steel. Due to the small size and low volume fraction of precipitates in steels, many characterization techniques have been used (e.g., SEM [2], QXRD [3], etc.). This chapter presents a literature review of the research works available.

First of all, some general information regarding microalloyed steels, heat treated steels, quench and temper (Q&T) and thermo-mechanical controlled processing (TMCP) will be introduced. Information regarding precipitation, precipitation strengthening and the type of precipitates are then presented, followed by a review of the different techniques that are available for precipitate characterization. Finally a review of different precipitation models is covered.

## 2.1 Microalloyed steels, heat treated steels, Q&T and TMCP

The combination of composition and TMCP/Q&T is important to produce high-strength steels such as microalloyed steels or heat-treated steels. TMCP is well-established for producing steel in the pipeline industry [4, 5]. Figure 2.1 shows a schematic of a TMCP schedule. TMCP is a combination of controlled thermal and deformation treatments occurring simultaneously. After

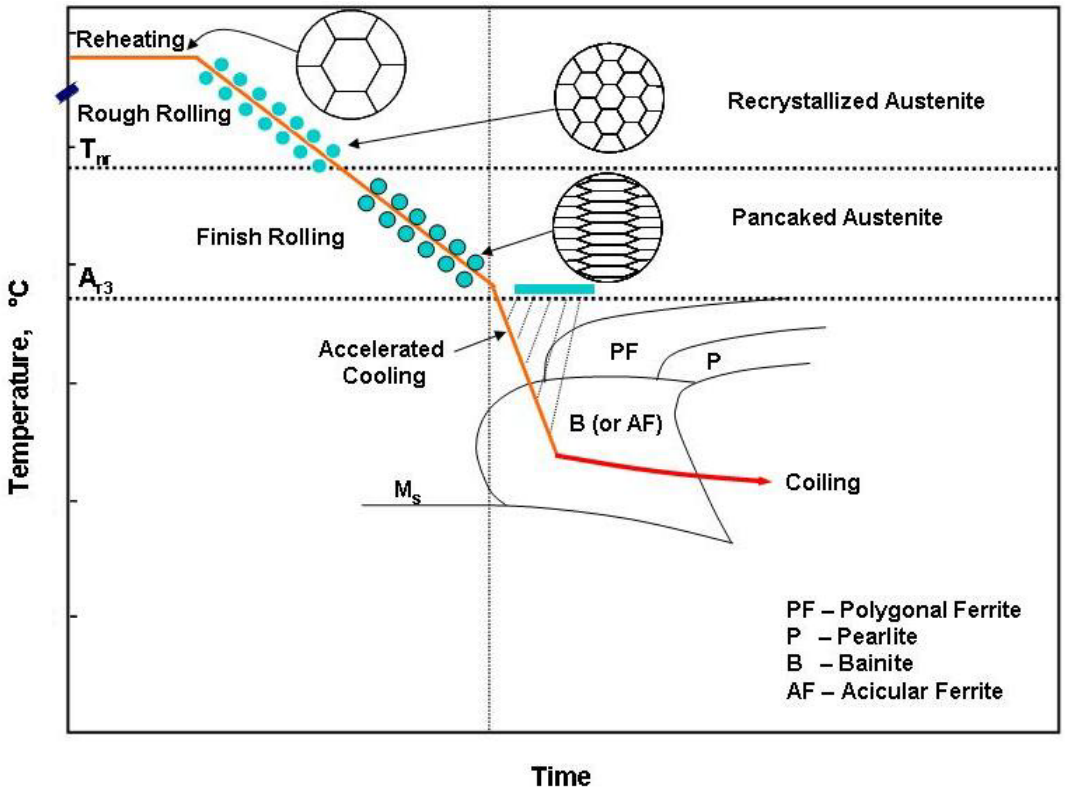


FIG. 2.1 – Schematic of a TMCP schedule [5].

casting, the steel is reheated to a high temperature (about 1250°C) for austenite homogenization so that elements that will form precipitates during subsequent processing (e.g., Nb, Mo, etc.) are dissolved in the steel. Rough rolling occurs then at temperature above the non-recrystallization temperature $T_{nr}$ to break down the austenite grains through multiple recrystallization cycles. Below $T_{nr}$, but above the austenite to ferrite transformation temperature ($A_{r3}$) is carried out finish rolling (no more recrystallization). The purpose of finish rolling is to produce pancaked austenite. Austenite pancaking allows augmentation of surface area over volume ratio, i.e., elongation of austenite grains and formation of deformation bands, to enhance nucleation and refinement of ferrite grains. In order to control the microstructure, the steel undergoes accelerated cooling from a temperature above the austenite to ferrite transformation temperature to an interrupted cooling temperature (ICT). Accelerated cooling, also referred as run-out table, consists of a succession of water banks that discharge water onto the skelp and allow control of the cooling rate that determines the microstructure evolution, i.e., austenite to polygonal ferrite

and/or bainite [5]. The main temperature parameters of TMCP are the reheating temperature (RT), finish rolling temperature (FRT), cooling rate (CR) during accelerated cooling and coiling interrupt temperature (CIT). All these temperatures noticeably affect the microstructure, grain refinement and precipitation in the steel [2]. Microalloyed steels contain small additions (in amounts less than 0.1 wt%) of C, N, Nb, Ti and V. Carbon level is kept low because of low carbon solubility in iron. At room temperature, the maximum solubility of carbon is 0.005 wt% [6]. They also may contain other alloying elements such as Mo, Cr, Mn or Si in amounts exceeding 0.1 wt%. Each of these additions has an effect on the steel properties. Lu [2] described the effect of each individual alloying addition. It is well known that the addition of Nb, Ti and V helps to refine the microstructure by allowing the formation of nanosized (less than 10 nm) precipitates that control recrystallization [7]. The presence of Nb nanosize precipitates also adds a precipitation strengthening effect. It has also been shown that the addition of Mo retards the dynamic precipitation of Nb(C,N) in austenite [8].

Quenching and tempering (Q&T) refers to a succession of different heat treatments, i.e., austenitization at high temperature (around 900°C), quenching then tempering at a lower temperature for several hours (e.g., 600°C for 3 h) and finally air cooling. After forming the pipe, it is austenitized thus transforming ferrite to austenite where carbon is much more soluble. The carbides that were present in ferrite are also dissolved through austenitization [9]. Then quenching allows the formation of martensite from austenite [10]. Finally, the steel is tempered in order to achieve the desired properties in terms of toughness, strength and hardness. The structural changes involve the formation of tempered martensite [11]. Q&T conditions such as the tempering temperature or the tempering time considerably affect the heat treated steel properties [11]. Q&T heat treated steels have a much higher carbon content (around 0.25-0.5 wt%) than microalloyed steels. This high carbon content increases hardenability of the steel. They also may contain high amounts (exceeding 0.25 wt%) of Mo or Cr to retard the rate of softening during tempering by forming carbides [12]. Figure 2.2 shows the evolution of hardness as a function of the alloying content and tempering temperature. The higher the carbon content and the lower the tempering temperature the higher the hardness. The addition of Mo, Ti, Cr or V allows the increase of hardness at higher tempering temperature (linked to carbides formation).

It was shown that Mo and Cr can form complex (Fe,Cr,Mo)C phases in heat treated steels [13]. However, it is still not clear how Cr exactly affects the microstructure or precipitation in heat treated steels.

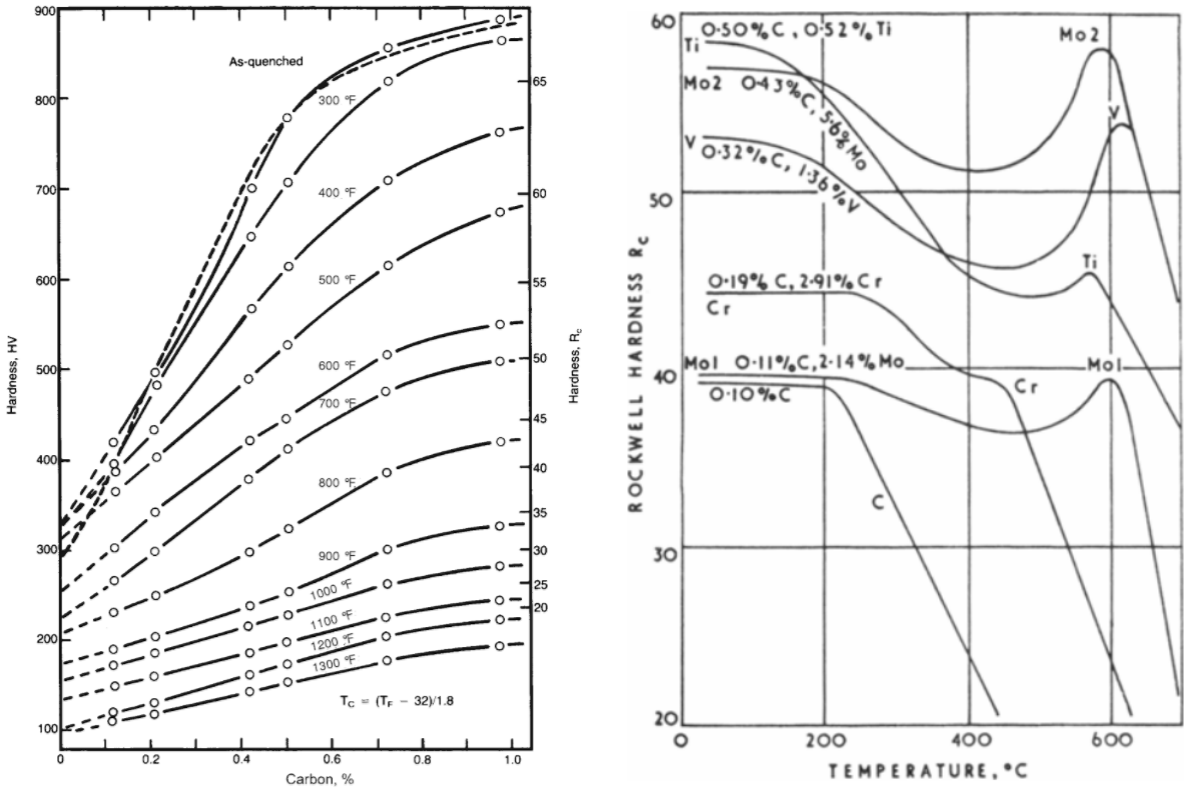


(A) (B)

FIG. 2.2 – Hardness as a function of tempering temperature and (A) carbon content [12] (B) alloying content [14], in different Fe-C alloys.

## 2.2 Types of precipitates in steels

Many different precipitates can be found in microalloyed and heat treated steels. The main types encountered in microalloyed steels are complex carbonitridres (Nb,Ti,V,Mo)(C,N). These precipitates have a NaCl face centered cubic (fcc) crystal structure (space group $Fm\bar{3}m$) and have a range of lattice parameters varying between 4.245 Å (pure TiN structure, large precipitates) and 4.469 Å (pure NbC structure, small precipitates) [15]. It was shown that small precipitates can nucleate at the interface of preexisting larger precipitates [16]. For example, large

($\simeq$ 1 µm) cubic TiN precipitates that form during casting can act as nucleation sites for smaller (Nb,Ti,Mo)(C,N) particles in microalloyed steels.

In high Mo-Cr heat treated steels the following precipitation sequence was determined. During the tempering step of Q&T, the first phase to form appears to be CrN, then (Cr,Mo)(N,C), followed by (Mo,Cr)(C,N), and eventually $Mo_2C$ [17]. Complex $(Fe_xCr_y)C_n$ carbides were also detected in high Cr (2.25 wt%) heat-treated steels [18]. Those precipitates were examined using carbon replicas and transmission electron microscopy (TEM). A complex $Mo_xCr_yC$ structure is also physically possible [19]. Concerning $Mo_2C$ particles, they have a hexagonal crystal structure (space group P63/mmc). Table 2.1 presents the different lattice parameters of the main precipitate types.

TABLE 2.1 – Lattice parameters of the main precipitate types.

| Phase | a or (a,b,c) in Å | Space group | Reference |
|---|---|---|---|
| TiN | 4.245 | $Fm\bar{3}m$ | [15] |
| TiC | 4.327 | $Fm\bar{3}m$ | [15] |
| NbN | 4.395 | $Fm\bar{3}m$ | [15] |
| NbC | 4.469 | $Fm\bar{3}m$ | [15] |
| VN | 4.139 | $Fm\bar{3}m$ | [15] |
| VC | 4.182 | $Fm\bar{3}m$ | [15] |
| MoN | 4.215 | $Fm\bar{3}m$ | [20] |
| MoC | 4.27 | $Fm\bar{3}m$ | [21] |
| $Mo_2C$ | (3.019,3.019,4.746) | P63/mmc | [19] |

All the aforementioned precipitates have very different solubility products (Figure 2.3) in austenite and ferrite and do not precipitate at the same stage of TMCP or Q&T. Because of its low solubity in austenite, TiN forms during casting and is not dissolved during TMCP [22]. NbC, TiC and VC have the highest solubility in ferrite. Therefore, they form during the latest stages of TMCP (laminar cooling and coiling) when temperatures are below 800°C [1].

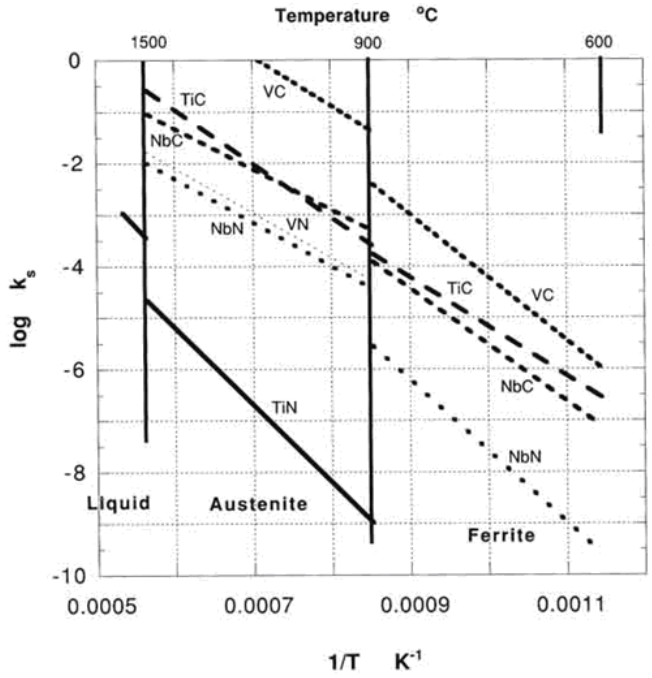


FIG. 2.3 – Comparison of the solubility products $K_S$ for different carbides and nitrides in austenite and ferrite [1].

Molybdenum carbides have higher solubility products in austenite and ferrite (Figure 2.4) than other microalloy carbides such as NbC or VC as shown in [23]. Due to this high solubility, Mo carbides form during Q&T at low temperature, i.e., below 700°C.

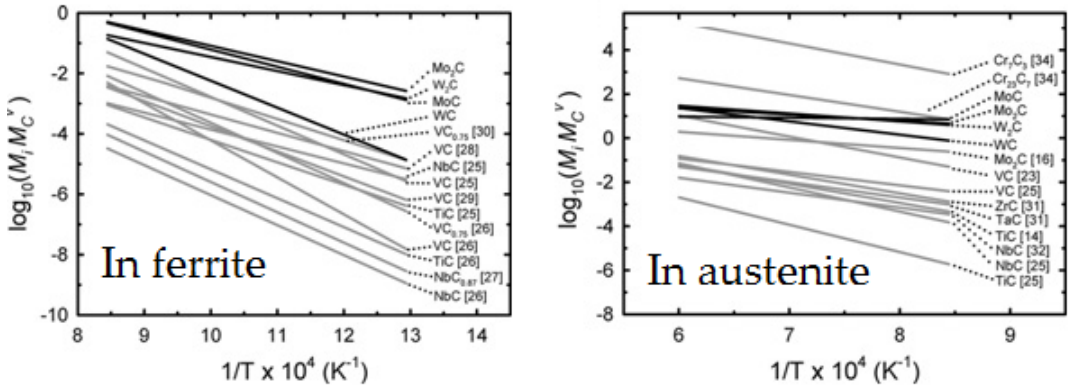


FIG. 2.4 – Comparison of the solubility products $K_S$ for different carbides in austenite and ferrite [23].

The precipitates have different shapes (e.g., cubic for TiN and spherical for NbC), compositions and sizes. Nevertheless, they have one thing in common, that makes their characterizations difficult, which is a very low volume fraction (as low as 0.1%).

## 2.3 Strengthening mechanisms

Different strengthening mechanisms take place in microalloyed and heat treated steels including grain size refinement strengthening (the finer the grain size, the larger the amount of grain boundaries that impedes dislocation motion), solid solution strengthening, precipitation strengthening ($\sigma_{ppt}$) and other mechanisms (dislocation strengthening, texture strengthening). Lu has summarized and described these mechanisms in [2]. Because the present work deals with precipitation, the focus will be on $\sigma_{ppt}$, precipitation strengthening, defined by Equation 4.15 [1].

$$\sigma_{ppt}(\text{MPa}) = \left(\frac{10.8 \cdot f_v^{\frac{1}{2}}}{X}\right) \ln\left(\frac{X}{6.125 \cdot 10^{-4}}\right) \tag{2.1}$$

where $\sigma_{ppt}$ is the precipitation strengthening in MPa, $f_v$ the volume fraction of precipitates and X the mean diameter of precipitates in µm. Precipitation strengthening is a major contributor to the overall strength in a steel (up to 25%). Two mechanisms are involved and are linked to the interaction between precipitates and dislocations. First of all, dislocation motion is slowed down by the precipitates and dislocations can shear the precipitates. A second interaction appears when the precipitates are too hard to be cut and is referred as Orowan looping. More information can be found in [24]. Dislocations are not likely able to shear very hard particles. In this case, Orowan looping becomes the primary strengthening mechanism. Equation 2.1 accounts for Orowan looping. The precipitate characteristics $f_v$ and X have to be quantified to determine the effect of the precipitation on steel strength [25]. Each type of precipitates has a particular composition, volume fraction and size.

## 2.4 Precipitate characterization

Many different techniques are used to characterize precipitates in steels. Some techniques are localized such as scanning or transmission electron microscopy (SEM, TEM). Some others allow for the analysis of a statistical amount of particles such as QXRD.

### 2.4.1 Scanning and transmission electron microscopy (SEM and TEM)

A method to look at precipitates is by SEM. Both size and composition of precipitates can be measured using SEM analysis and energy-dispersive X-ray spectroscopy (EDX) analysis. However it is very difficult to observe nanosized precipitates except using carbon replicas. It is then possible to observe nanoscale particles [26]. It allows an estimatation of size distribution and mean composition but the number of analyzed particles is low. Using TEM with a carbon replica or thin film technique allows for the observation of very small precipitates and can provide good information regarding the composition and even the crystal structure of the particles. However, the number of precipitates that can be analyzed is very low and not statistically relevant of the whole sample [2].

### 2.4.2 Atom probe tomography

Atom probe tomography (APT) is also an alternative, which combines a field ion microscope and a mass spectrometer. It is a destructive technique where sample ions are removed from the sample surface. The microscope allows for the detection of single ions. Each ion has a unique position on the detector. Computer methods are utilized to rebuild a 3D view of the sample based on the position of each ion. It was reported [27, 28] that it is possible to characterize nanoscale precipitates through APT. However, this technique is localized and it is difficult to analyze enough material to make sure the results are representative of the whole sample. Nevertheless this technique is quite accurate.

### 2.4.3 Small angle neutron scattering

Small angle neutron scattering (SANS) is one of the few techniques that can analyze a large piece of material and characterize the size distribution and volume fraction of nanoprecipitates present in the sample [29, 30, 31]. The size range of conventional SANS is approximately 2 to 100 nm. Because of the large penetration depth of neutrons, a large volume of material can be analyzed. The only drawback is that it is not possible to determine either the chemical composition or the relative abundance of each type of precipitates. Another technique that would allow complete and statistical characterization is therefore needed.

### 2.4.4 Matrix dissolution

The matrix dissolution method allows for the separation of the precipitates and the steel matrix. The steel matrix is dissolved and the precipitates, which are stable in the solution used for the dissolution, can be collected. A large piece of steel allows for the collection of a large amount of precipitates. It was shown by Lu [2] that matrix dissolution techniques in combination with SEM, TEM and QXRD are the best way to analyze with great accuracy a large amount of precipitates. The two main types of dissolution are chemical dissolution and electrolytic dissolution. A summary and description of these techniques are presented in [2].

Electrolytic dissolution has the advantage of selectivity [32]. The use of a particular electrolyte at precise conditions (current/voltage) allows selection of specific precipitates. However, this kind of dissolution is time consuming and is not ideal for generating quick results.

The second type of dissolution is chemical dissolution. Once again different solutions are available. Halogen-based ($Br_2$ or $I_2$ in methanol or ethanol) are the most common solutions to dissolve steels. It is possible to collect precipitates such as $Fe_3C$, MnS or $Cr_3C_2$ [33]. This type of dissolution is very slow though.

Acid solutions such as HCl, $HNO_3$, $H_2SO_4$ allow selection of the type of collected precipitates while being time efficient. The best solution is a mixture of water and 6N HCl [34], for many reasons; the high solubity of $FeCl_2$ (product of the dissolution) in water, all Nb and Ti

carbonitrides are collected and dissolution is time-efficient [35]. Mo carbides [36] and Cr carbides [37] are stable and insoluble in HCl. However, acidic solutions do not allow for collection of unstable phases such as $Fe_3C$ or MnS. One inconvenience is that this dissolution method is often associated with the formation of an amorphous $SiO_2$ phase.

Dissolution using a mixture of 6N HCl and water [34] was chosen for this work and will be further detailed in Chapter 3. Once the precipitates are collected, the main analysis is quantitative x-ray diffraction (QXRD) analysis by doing a Rietveld refinement.

### 2.4.5 X-ray diffraction – Rietveld refinement (QXRD)

XRD analysis is a semi-quantitative analysis. The Rietveld method [38, 39] is a least-square fitting approach that calculates a theoretical XRD pattern (many phases at the same time) in order to match that experimental diffraction pattern. Many different parameters are used to calculate the theoretical pattern including the lattice parameters, the atomic compositions, the crystallite sizes (apparent domain sizes $L_{vol}$ in nm), the lattice strains, the relative scale and the relative abundance.

$L_{vol}$ is linked to the mean radius ($\bar{R}$ in nm) of the precipitate distribution (standard deviation $\sigma$) by Equation 2.2 [40].

$$L_{vol} = \frac{3\bar{R}(1+c)^3}{2} \qquad \text{with} \quad c = \frac{\sigma^2}{\bar{R}^2} \tag{2.2}$$

where $c = 0$ for a monodisperse spherical distribution, and $c = 0.2$ for a typical lognormal distribution [41]. This technique has been successfully applied to Grade 100 steel precipitates extracted by matrix dissolution [42].

## 2.5 NbC precipitation modeling

A lot of work has already been done on precipitation modeling and behavior in austenite. It is quite difficult to model the precipitation of NbC in ferrite since the thermodynamic data are

still uncertain. All the current models only take into account isothermal transformations. Mathematical simulations (based on classical nucleation theory) can be used to model precipitation kinetics of NbC in ferrite.

### 2.5.1 Thermodynamic data available

Gendt presents [43] a review of all the thermodynamic data available for the $\alpha$-Fe-Nb-C system, i.e., solubility products, diffusion coefficients for Nb and C in $\alpha$-Fe and activation energies for Nb and C in $\alpha$-Fe. Table 2.2 summarizes the thermodynamic data that Gendt selected to model the isothermal precipitation of NbC in ferrite. These thermodynamic data will be used for the modeling of NbC precipitation during laminar cooling in Chapter 4.

TABLE 2.2 – Thermodynamic data for NbC in ferrite [43].

| Parameter | Symbol | Value |
|---|---|---|
| Diffusion pre-factors (in ferrite) | $D^0_{Nb}$ ($m^2.s^{-1}$) | $5 \cdot 10^{-3}$ |
| | $D^0_C$ ($m^2.s^{-1}$) | $2 \cdot 10^{-6}$ |
| Activation energies (in ferrite) | $Q_{Nb}$ ($kJ.mol^{-1}$) | 251.4 |
| | $Q_C$ ($kJ.mol^{-1}$) | 84.6 |
| Interface energy of NbC in ferrite | $\gamma$ ($J.m^{-2}$) | 0.73 |
| Dislocation density | $\rho$ ($m.m^{-3}$) | $2 \cdot 10^{14}$ |
| Solubility product $K_S$, $\ln(K_S) = B - \frac{A}{T}$ | A (K) | 14560 |
| | B | -7.33 |

### 2.5.2 Different approaches

Three precipitation models based on classical nucleation theory (CNT) are reviewed [44]; the mean radius approach, the Euler-like multi-class approach and the Lagrange-like multi-class approach. In these models, only homogeneous precipitation is considered. The precipitation of particles at the interface of preexisting precipitates is not considered [16]. Other assumptions made in the model development include [43]:

1. Only stoichiometric compounds (e.g., NbC) are considered.
2. The precipitates are spherical.
3. Due to the low volume fraction, there is no interaction between the precipitates.
4. The interfacial energy is constant (no temperature dependency).
5. There is always a local equilibrium between the precipitates and the matrix (curvature effect or Gibbs-Thomson effect).
6. Carbon only is at the thermodynamic equilibrium. This is due to the high diffusivity of C in $\alpha$-Fe, and low diffusivity of Nb in $\alpha$-Fe.

This 'mean radius approach' is the simplest one where only the mean radius and the number density are predicted but not the particle size distribution. Precipitation occurs in $\alpha$-Fe. Perrard applied this model to the NbC precipitation on dislocations in ferrite [31].

The Euler-like multi-class approach is inspired by the KW nucleation model (Kampmann and Wagner [45]). In this approach "the particle size distribution is discretized in several size classes and its time evolution is calculated evaluating the fluxes between neighboring classes". Precipitation occurs in $\alpha$-Fe.

The 'Lagrange-like multi-class approach' or 'Multipreci' algorithm is based on the work by Maugis [46] and is close to what Fujita and Bhadeshia did [47]. In this approach "the particle size distribution (PSD) is again discretized in several size classes, whose radius time evolutions are calculated". Precipitation occurs in $\alpha$-Fe. This approach was chosen for the present work, mainly because the PSD is tracked during the simulation, and is detailed in Chapter 4.

### 2.5.3 Validation of the methods

In order to validate the different methods, some techniques that were previously presented are used. For example, Perrard [31] did SANS and TEM analysis on laboratory high-Nb (0.079 wt%) and low-Nb (0.04 wt%) steels to validate their precipitation kinetics model. They conducted different heat treatments (different time and temperature conditions) on these non commercial steels. Other studies used electrolytical dissolution to collect and analyze the precipitates

and compared the results to their model results [44]. Figure 2.5 presents the SANS and simulation results of Perrard. Good agreement between the experimental and the model results is observed.

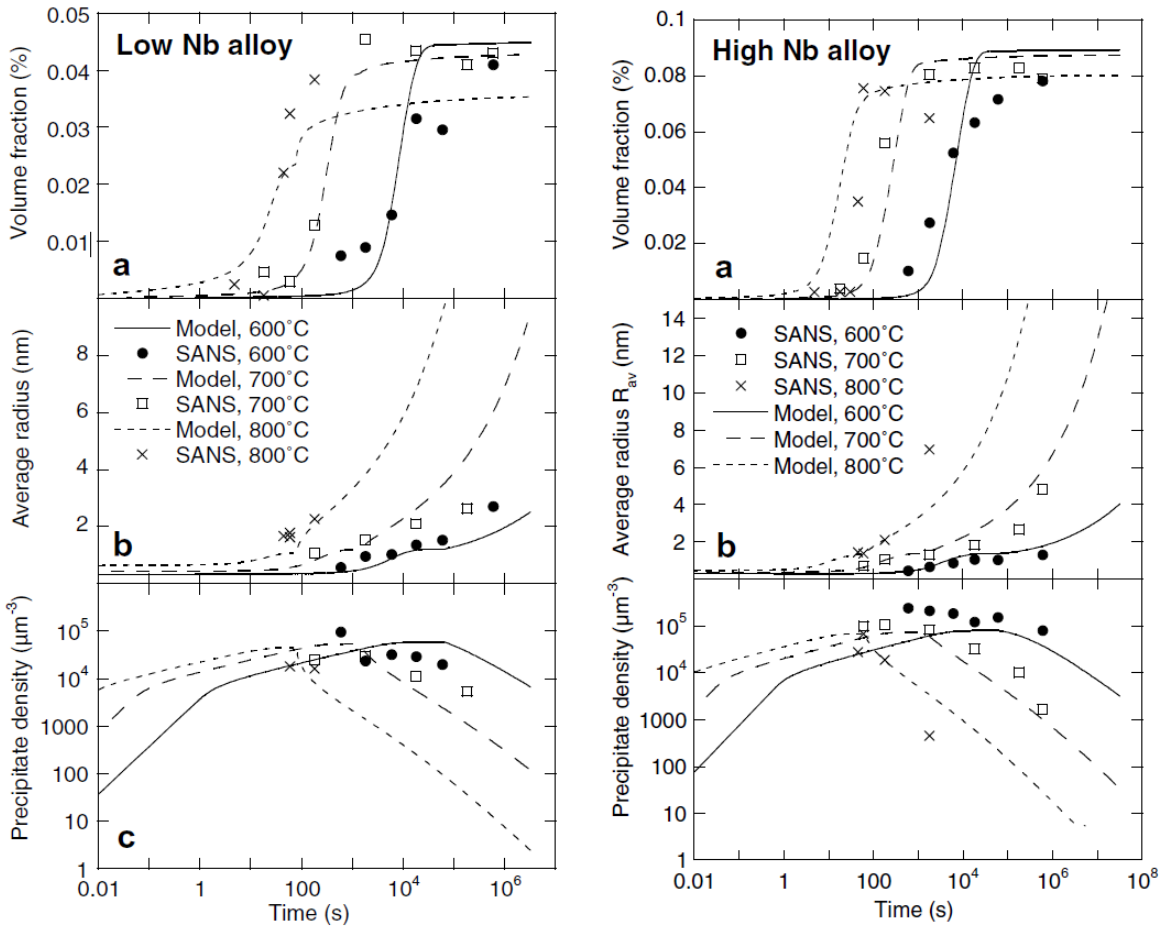


FIG. 2.5 – SANS results and NbC precipitation model results for low-Nb and high-Nb laboratory steels [31].

## 2.6 Summary

To sum up, matrix dissolution is the best experimental method to collect a large amount of precipitates. QXRD allows for the analysis of this large number of precipitates and for the determination of size distributions, compositions and relative abundance of each type of precipitates. Conventional microscopy techniques such as SEM or TEM allow for the analysis of a very small

amount of particles in comparison. Regarding precipitation modeling, different approaches exist to simulate NbC precipitation in ferrite. Both experimental and computational results can help answer the main questions previously stated in Chapter 1:

1. What is the effect of the thickness of a steel on precipitation for TMCP X70 steels?
2. What is the effect of Mo and Cr content on precipitation in Q&T steels?
3. How can nanoscale precipitation be predicted during the laminar cooling stage of TMCP?

# Chapter 3

# Experimental procedures

The purpose of this chapter is to describe the experimental procedures used. First, the different steels analyzed will be described. Then the experimental methods used will be presented such as electron back-scattered diffraction (EBSD) or scanning electron microscopy (SEM), followed by a description of the dissolution procedures. This chapter will finally present the different techniques (ICP, SEM-EDX and QXRD) used to characterize the precipitates collected during dissolution.

## 3.1 Steels analyzed

In total five steels were analyzed: two X70 steels, two L80 steels and a T95 steel which is similar to the L80 steels but with a higher Cr content. The steel compositions are shown in Table 3.1.

TABLE 3.1 – Steel compositions (wt%)

| Steel - Thickness | C | N | Nb | Mo | Ti | Cr | V |
|---|---|---|---|---|---|---|---|
| X70 – 11mm | 0.052 | 0.007 | 0.09 | 0.13 | 0.016 | 0.23 | 0.003 |
| TWX70 – 17 mm | 0.043 | 0.009 | 0.067 | 0.19 | 0.016 | 0.09 | 0.003 |
| L80 - 10 mm | 0.254 | 0.008 | 0 | 0.02 | 0.030 | 0.14 | 0.003 |
| ML80 - 8 mm | 0.252 | 0.003 | 0.001 | 0.49 | 0.001 | 0.22 | 0.001 |
| T95 - 11 mm | 0.27 | 0.007 | 0.001 | 0.19 | 0.041 | 0.90 | 0.006 |

The X70 and TWX70 (for thick wall X70) steels have very similar compositions and processing conditions (similar finish rolling temperature, around 790°C, and cooling rate, around 15°C/s). The main difference is the thickness of the gauge. The conventional X70 has a thickness of 11 mm, while the new product is 17 mm thick. More information on TWX70 can be found in [48].

The other steels (L80, ML80 and T95) are all heat treated steels (quenched and tempered steels) and have a similar microstructure (tempered martensite), allthough different quench-and-temper (Q&T) conditions. L80 pipes are heated to 900°C (austenization), then quenched and tempered at 680°C for 2 hour and finally air cooled. ML80 is tempered at 690°C for three hours and air cooled. T95 is tempered at a lower temperature during a shorter time. Their thicknesses are similar (Table. 3.1). The main differences are their chemistries: L80 is a low-Mo, medium-Cr and high-Ti steel, ML80 is a low-Ti, medium-Cr and high-Mo steel, and T95 is a medium-Mo, high-Cr and high-Ti steel.

Tensile tests were carried at the EVRAZ NA Research and Development Center based in Regina, SK. A Instron tensile test unit was used to measure the yield strength (YS), the ultimate tensile strength (UTS) and the percent of elongation (%El). Table 3.2 gives mechanical properties measured for each of the five steels analyzed.

TABLE 3.2 – Mechanical properties of the steels studied

| Steel - Thickness | YS (MPa) | UTS (MPa) | %El |
|---|---|---|---|
| X70 – 11mm | 524.0 | 651.6 | 37 |
| TWX70 – 17 mm | 554.3 | 679.1 | 38 |
| L80 - 10 mm | 594.3 | 692.2 | 30 |
| ML80 - 8 mm | 592.8 | 675.1 | 32 |
| T95 - 11 mm | 714.9 | 811.5 | 28 |

## 3.2 Microstructure analysis

All the steels were mounted, polished, etched and then analyzed using optical microscopy (OM) and SEM-EBSD in order to determine their microstructures (e.g., phases and grain sizes).

For each steel, a portion parallel to the centerline was cut and mounted into an epoxy resin. Three different thicknesses were cut, one from the surface just below the coating, one from the centerline and the last one at quarter thickness. Each sample was then ground successively with 240, 320, 600 and 800 grit SiC paper. After grinding, the sample was polished using 9 µm, 3 µm and 1 µm diamond suspensions, and finally polished with a 0.05 µm colloidal silica suspension. After cleaning with distilled water and ethanol, in an ultrasonic bath, the sample was etched. A 2% Nital solution (mixture of ethanol and 2% nitric acid) was used for 10-12 s to reveal the microstructure.

OM allows for observation of the sample at low magnification only. Therefore it was difficult to accurately measure the grain size or to be certain of the microstructure. Regarding precipitates, only large ones such as TiN-rich precipitates were visible using OM.

Scanning electron microscopy (SEM) was then used for its high resolution power. It is much easier to characterize the microstructure and the grain size. A Zeiss Sigma field-emission SEM (FE-SEM) operated at 10 kV was used to analyzed the etched samples. A secondary electron (SE) detector was used to obtain good surface resolution. An Zeiss Sigma FE-SEM operated at 20 kV coupled with an EBSD system was used to examine the grain orientation and the grain size more precisely. A mean linear intercept method (m.l.i.) was used to estimate the grain size. Due to the highly deformed microstructure, it was difficult to use the standard ASTM method to measure the grain size [49], which is why the m.l.i. method was used.

## 3.3 Chemical dissolution

As presented in Chapter 2, the best way to characterize the precipitates is to collect them by dissolving the matrix. After assessing dissolution techniques listed in the Literature Review,

HCl chemical dissolution was chosen based on its time efficiency and selectivity.

### 3.3.1 Experimental set-up

The experimental set-up (Figure 3.1) developed by Lu [2] consists of a classical reflux system. A small piece (or several pieces for a large dissolution set-up) was cut and polished to remove any trace of coating or oxidation and then weighed.

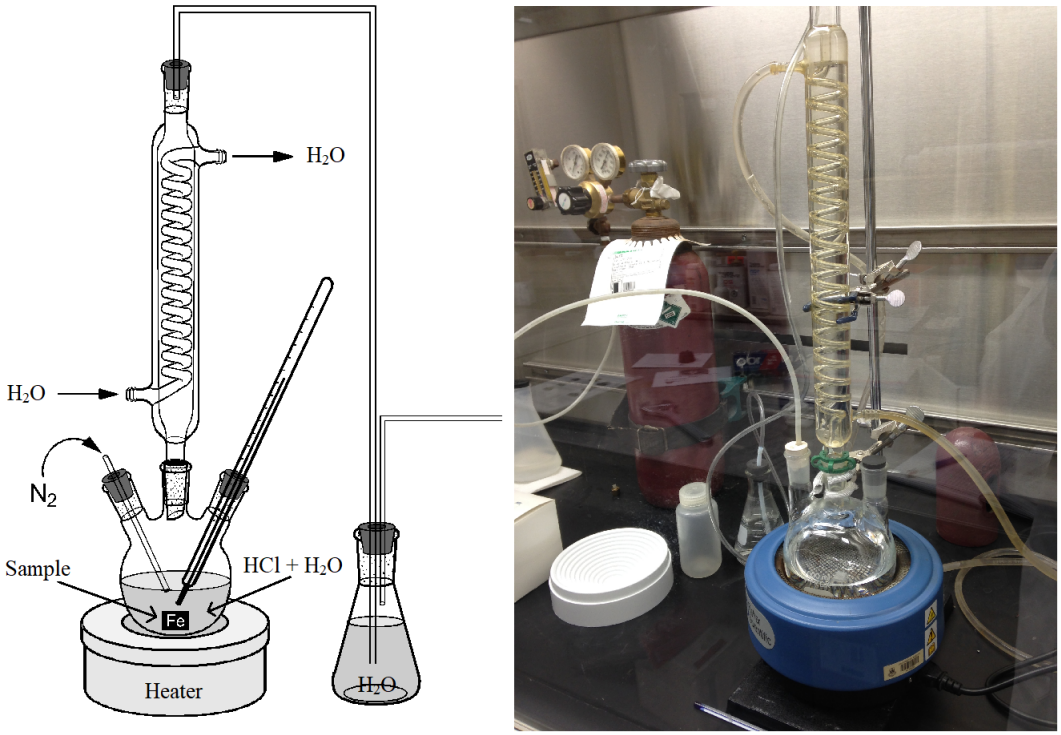


FIG. 3.1 – Experimental set-up (schematic and photograph).

In a three-neck flask (the reactor) a mixture of 6N HCl, distilled water and the steel sample to be dissolved were combined, according to ASTM standard E194-90 (200 mL of 6N HCl in 300 mL of distilled water per 10g of steel). The temperature of the reactor was maintained at 65-70°C in order to activate the reaction (hence the use of a heater). However, increasing the temperature to 90°C can accelerate the reaction significantly.

A condenser was mounted on the flask (middle neck), to avoid losing any part of the solution and to maintain a constant volume in the reactor. The first neck was used to connect the

reactor to a $N_2$ source, in order to provide a non-oxidizing atmosphere. The last neck was used to connect a thermometer to measure the temperature inside the reactor.

### 3.3.2 Modification of Lu's set-up

Lu observed the presence of amorphous $SiO_2$ in the collected residues [2]. This amorphous phase was an issue in further analysis. The presence of an amorphous phase makes SEM/TEM and XRD analysis more difficult as discussed in Chapter 2. It also makes the quantitative XRD analysis less accurate.

To remove the dissolved $O_2$ from the system, $N_2$ was directly injected into the solution before starting and during the dissolution process. Figure 3.2 shows the XRD results for two different dissolutions. The dissolution T95-2 was carried out with bubbling $N_2$, whereas the T95-3 was not. The difference is clear. T95-2 shows no amorphous 'bump' around $2\theta = 25°$ and the peak intensities are higher, making characterization easier.

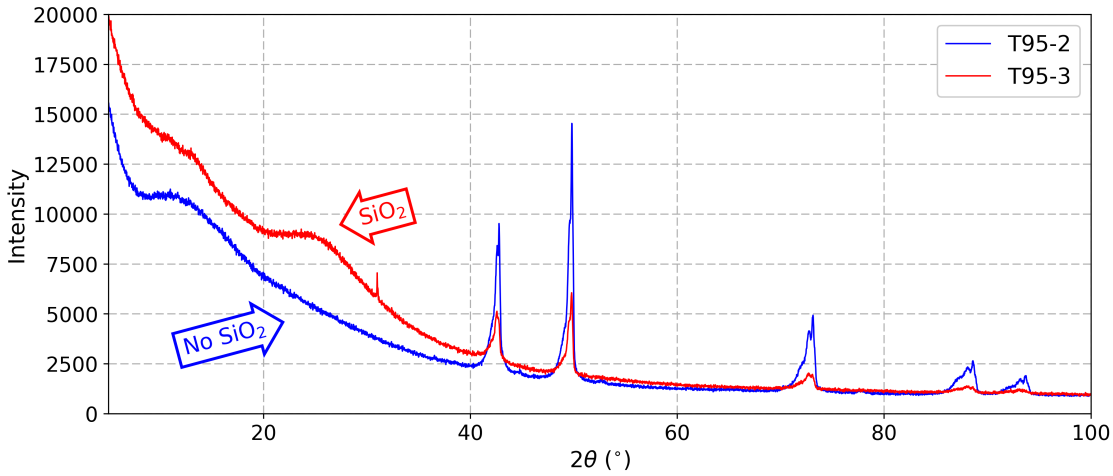


FIG. 3.2 – XRD pattern of residues form T95-2 (bubbling $N_2$ ) and T95-3 ($N_2$ atmosphere)

### 3.3.3 Centrifuge process

Following complete dissolution (around a week for a 10g sample), the precipitates were separated from the acid solution containing iron chloride $FeCl_2$. The process was lengthy and as

much $FeCl_2$ as possible had to be removed to obtain a clean powder.

To collect the precipitates, the solution containing the residues and the iron chlorides was transferred into centrifuge tubes. For this work, PPCO (polypropylene co-polymer) tubes were used as they do not react with the acid solution. A Sorvall RC-6 centrifuge (Mandel) was used to separate the residues and the supernatant solution, at a speed of 18300 RPM (maximum speed allowed for PPCO tubes) and at 4°C 0.5 h.

After a first centrifuge cycle, the supernatant solution was carefully removed and stored for further analysis and distilled water was added into the tube in order to clean the residues. The tubes were then put back in the centrifuge for a second cycle. At least two cycles were necessary to obtain a clean suspension. After the last cycle, the water was carefully removed and ethanol was added. The tubes were then put in an ultrasonic bath for 20 minutes in order to detach all precipitates from the tube inner walls.

A collection beaker was weighed with an accuracy of 0.1 g and the ethanol suspension containing the precipitates was poured into that beaker. After a few hours when all the ethanol had evaporated, the beaker was weighed again to measure the mass of the collected residue. This left a clean powder containing all the collected precipitates and a supernatant solution free of solid particles. Both samples were ready for analysis. Table 3.3 shows the different dissolution parameters used for each steels and their dissolution results. For each steel (except for L80 steel), two dissolutions were done (e.g., X70 and X70-2 for X70 steel).

## 3.4 ICP analysis of supernatant solution

Inductively coupled plasma mass spectroscopy (ICP-MS or ICP) is a spectroscopy technique that allows measurement of the concentration of elements dissolved in liquid solutions. A Perkin Elmer Elan 6000 ICP-MS was used to measure the amount of the main alloying elements (Ti, Nb, Mo, Cr, etc.) present in the supernatant solutions (collected after the first centrifuge cycle). Each result was the average of three measurements. Calibration was done using a four point calibration method. Bi, Sc and In were used as internal standards.

TABLE 3.3 – Dissolution parameters and results for X70, TWX70, L80, ML80 and T95 steels.

| Steel | $m_{steel}$ (g) | $V_{solution}$ (mL) | T (°C) | Duration | $m_{residues}$ (mg) |
|---|---|---|---|---|---|
| X70 | 48.1474 | 2500 | 90 | 3 weeks | 67.1 |
| X70-2 | 9.9800 | 500 | 90 | 1 weeks | 11.9 |
| TWX70 | 10.1308 | 500 | 90 | 1 week | 12.2 |
| TWX70-2 | 10.2214 | 500 | 90 | 1 week | 10.6 |
| L80 | 40.0128 | 2330 | 90 | 3 weeks | 4.6 |
| ML80 | 9.7644 | 500 | 90 | 1 week | 11.1 |
| ML80-2 | 9.7548 | 500 | 90 | 1 week | 9.5 |
| T95 | 10.1818 | 500 | 90 | 1 week | 9.7 |
| T95-2 | 10.4851 | 500 | 90 | 1 week | 10.3 |

If the mass of the dissolved steel sample and the volume of the initial solution are known, the mass fraction of each element that remains in solution can be calculated. This information was used to complete the mass balance for the quantitative XRD analysis of the collected precipitates.

## 3.5 XRD analysis of the precipitates

XRD analysis was undertaken for each steel and QXRD was applied to determine the precipitate characteristics such as particle size distribution, compositions and relative abundance.

### 3.5.1 XRD Measurements

As can be seen in Table 3.3, the amount of collected powders is quite low (around 5-10 mg per 10 g of steel); therefore only a small amount of powder was available for XRD analysis. Nevertheless it was still possible to collect a good diffraction pattern using a quartz sample holder (to avoid issues due to the thickness of the sample).

A Rigaku Ultima IV unit was used to collect the XRD patterns. Table 3.4 provides relevant diffraction data. The software Jade (version 9) was used to analyze XRD patterns using the International center for diffraction data (ICDD) database. This analysis is referred as Jade analysis in Chapters 5 and 6.

TABLE 3.4 – X-ray diffraction data

| Diffractometer | Rigaku Ultima IV |
|---|---|
| Radiation | Co - $\lambda$ = 0.1790260 nm |
| Detector | D/Tex with Fe filter |
| 2$\theta$ range | 5° - 100° |
| Scan | 0.02°/step |
| Scan speed | 2°/min |
| Sample holder | Quartz |

Before running a sample, a standardisation of the XRD has to be done using a $LaB_6$ standard. This standardisation allows for the calibration of the XRD and is necessary to determine the instrument broadening. Ideally a standardisation should be done before every run. However, if many samples are run during the same day or week it is sufficient to run a $LaB_6$ standard once before and once after (at the end to check the calibration).

### 3.5.2 Rietveld refinement and QXRD analysis

A simple analysis can be done on the raw XRD pattern based on the peak positions; however, only a rough estimation of the amount of phases is possible. A more complex analysis can also be done using the Rietveld method [38, 39] (QXRD).

The software Topas (Academic version) was used to refine the phase structures and calculate the relative abundance of each phase. The software uses a linear least squares method to refine the background (due to the sample holder), lattice parameters, occupancy of each atom, scale factor (to refine the relative intensity of each phase), size effect and strain effect.

The space group and the atomic positions need to be provided (the Crystallographic Information File or CIF file can be found easily through the Crystallographic Open Database [1]). The refinement procedure itself is particular and has to be thoroughly followed in order to obtain a good fit and consistency between samples. The procedure is outlined bellow.

1. A RAW file was read. An XRD data file with the background already removed is a source of error.
2. Instrument parameters (type of tube, wavelength, etc.) were added.
3. Cagliotti parameters (experimental parameters) which define the instrument broadening are obtained from a $LaB_6$ standard.
4. The background was fit with a 6th, 7th or 8th order Chebyshev polynomial function.
5. A single phase (e.g., TiN or NbC, based on prior knowledge of the steel) was added to the analysis. Its space group, lattice parameters, atomic positions and occupancies were added.
6. The lattice parameter of this first phase was refined first to fit the peak positions.
7. This was followed by the addition of size and strain effects. These parameters refine the shape of the peak.
8. The atomic composition was refined to fit the peak intensities.
9. Steps 6 to 8 were repeated in order to improve the fit.
10. Steps 5 to 9 were repeated for other phases to be included.

When a fit is visually good (a lower weighted profile R-factor $R_{wp}$ denotes a better fit [50]), the parameters need to be checked for physical consistency. To do so, the lattice parameters and the composition of each phase were correlated to ensure that no aberrations were encountered. ICP results were used to ensure mass balance (discussed later). The relative abundance of each

[1] `http://www.crystallography.net/cod/search.html`

phase was calculated. Topas uses Equation 3.1 [51] to calculate $w_\phi$, which is the relative weight fraction of a given phase $\varphi$.

$$w_\varphi = \frac{s_\varphi M_\varphi Z_\varphi V_\varphi}{\sum_{\varphi_i} s_{\varphi_i} M_{\varphi_i} Z_{\varphi_i} V_{\varphi_i}} \tag{3.1}$$

where s is the scale factor calculated by TOPAS, M is the mass of the unit cell, Z is the number of atoms in the unit cell and V is the volume of the unit cell.

When the relative weight fraction of each phase is known, it is possible to calculate the fraction of each element in the precipitate phase; this was compared to the fraction calculated from ICP measurements. The veracity of the Topas refinement was determined by checking the mass balance between the ICP and QXRD results. Once the mass balance was determined to be valid and all the parameters were consistent, the refinement was done and provided a good estimation of the lattice parameters (a), mean composition, crystallite size ($L_{vol}$) , mean strain and relative abundance for each phase $w_\varphi$. The mean radius $\bar{R}$ of the precipitate was calculated with Equation 3.2.

$$\bar{R} = \frac{2 \cdot L_{vol}}{3 \cdot (1 + c)^3} \tag{3.2}$$

where c = 0.2 for a typical lognormal distribution [41].

## 3.6 SEM-EDX analysis of collected precipitates

A Zeiss FE-SEM was used to image the collected precipitates, using an in-lens SE detector, combined with a Bruker energy dispersive X-ray (EDX) system to analyze the composition of the precipitates. A small amount of collected powder was deposited on a piece of carbon tape, attached to an SEM Al pin holder. In order to obtain a good image of the precipitates, the FE-SEM was operated at a low accelerating voltage (between 5 and 10 kV). Samples were coated with a thin layer of evaporated coating to minimize charging. However, for composition analysis using the EDX system, a higher accelerating voltage was used (20 kV). In these cases the carbon

coating was unnecessary and could be an issue.

Important microstructural information was obtained from SEM-EDX analysis, i.e., the shape of the precipitates, size and size distribution and semi-quantitative compositions. A major issue with SEM analysis is that the precipitates tend to agglomerate while drying. One way to examine the nano-precipitates was to form a suspension with ethanol followed by deposition of a drop or two of the suspension onto a piece of carbon tape. The preparation of the suspension was not trivial since the proper amount of agglomerates had to be added to the ethanol to form the suspension. An ultrasonic bath was used for particle separation. If the amount of agglomerates was too high, they were not broken up in the ultrasonic bath. If the amount was too low, the deposited particles were too sparse. A visual inspection of the suspension was often sufficient to determine if the deposition would succeed.

## 3.7 Error analysis

Many errors could be encountered in the quantitative analysis. The most important errors (due to propagation) arise from the volume and weight measurements of the liquids and solids during matrix dissolution. For instance, the volume of the acid solution introduced into the flask was measured with an error of 1 mL. The mass of each sample (steel or powder) had a precision of 0.1 mg. In addition, during each step of the dissolution process the amount of collected precipitates decreased. Some precipitates were lost while transferring the solution from the flask to the centrifuge tube. Some more were lost during the cleaning process. Finally, other precipitates were left in the tubes during transfer into the collection beaker. Therefore, the error associated with the final weight of precipitates was higher than 0.1 mg. This could have an impact during the mass balance calculation.

The EDX measurements cannot be considered as quantitative but only qualitative or semi-quantitative at best. As such, only approximate composition were determined. Nevertheless, EDX was a good way to estimate the range of compositions for the precipitates.

The QXRD analysis provided another source of error. It was shown in [52] that a relative

weight fraction (of a particular phase) below 5% was reliable. This was also taken into account for the mass balance calculations.

# Chapter 4

# Modeling of NbC precipitation kinetics during laminar cooling

It is clear that the nanoprecipitation of NbC in microalloyed steels noticeably affects precipitation strengthening [1, 25]. Smaller precipitates and larger volume fractions result in better precipitation strengthening. During casting only coarse precipitates form. These precipitates are mainly TiN-rich precipitates because of their low solubility in austenite. Carbides such as niobium carbides form in later stages of TMCP due to their solubility in austenite and ferrite. The laminar cooling stage allows nanoscale precipitates to form and the ability to predict this precipitation process is a way to predict and improve precipitation strengthening. This chapter will present modeling work for niobium carbide (NbC) precipitation kinetics during laminar cooling (last step of TMCP).

## 4.1 Lagrange "Multipreci" approach

Different approaches to model precipitation are presented in Chapter 2, Section 2.5 [44] and include the mean radius approach, the Euler approach and the Lagrange approach (inspired by the Multipreci approach [46]). The Lagrange-like multi-class approach was chosen for this work for two reasons. The system is discretized into classes (in sizes) of precipitates and the key predicted variable is the mean radius of each class.

The inputs to the model are the processing conditions (such as different temperatures) and the steel specifications. The model predicts the mean radius, size distribution and volume fraction of the precipitates.

Many simulations treat nucleation, growth and coalescence independently and sequentially. In this approach, the three steps are not separated and are considered at the same time. Doing a criterion governing transition between stages is avoided. Herein, the Gibbs-Thomson effect will determine the distinction between growth and dissolution and, therefore, coarsening. If dissolution occurs, the solid solution concentration will increase and the remaining precipitates will be able to grow. Finally, in order to account for laminar cooling the temperature will change over the course of the simulation.

## 4.2 Assumptions

Several assumptions were made in order to model the precipitation kinetics of NbC [43].

1. Only stoichiometric NbC particles are considered.
2. The precipitates are spherical.
3. Due to their low volume fraction, there is no interaction between the precipitates.
4. The interfacial energy is constant (no temperature dependency).
5. There is always a local equilibrium between the precipitates and the matrix (curvature effect or Gibbs-Thomson effect).
6. Carbon only is at thermodynamic equilibrium. This is due to the high diffusivity of C in $\alpha$-Fe and the low diffusivity of Nb in $\alpha$-Fe.
7. To simplify the model, dislocations are assumed to have no effect on nucleation. Only homogeneous nucleation is considered.
8. After finish rolling, ferrite is considered to be the only matrix phase present.

All these assumptions will be discussed in Chapter 7.

## 4.3 Classical nucleation theory

### 4.3.1 Nucleation

The Gibbs free energy of formation of NbC (spherical with radius R) is given by Equation 4.1 [44].

$$\Delta G(R) = \frac{4}{3}\pi R^3 \Delta g + 4\pi R^2 \gamma \tag{4.1}$$

where $\Delta g$ is the free energy per unit volume and $\gamma$ the interfacial energy between NbC and $\alpha$-Fe. Using a regular solution approximation [43], $\Delta g$ is defined by Equation 4.2.

$$\Delta g = \frac{-kT}{v_{NbC}} \ln\left(\frac{X_C \cdot X_{Nb}}{K_S(T)}\right) \tag{4.2}$$

where $v_{NbC} = \frac{a_{NbC}^3}{4}$ is the atomic volume of NbC (lattice parameter $a_{NbC}$ = 4.47 Å, 4 NbC per lattice), $v_{NbC} = 2.2 \cdot 10^{-29}$ $m^3$. $K_S(T)$ is the solubility product of NbC at a temperature T defined by $K_S = X_{Nb}^{eq} X_C^{eq}$. $X_C$ and $X_{Nb}$ are the atomic concentrations of C and Nb in the matrix.

Equation 4.1 allows a maximum for a critical radius $R^\star$ ($\Delta G(R^\star)$ is a maximum). Precipitates with a radius smaller than $R^\star$ will tend to dissolve, while those larger than $R^\star$ will coarsen. $R^\star$ is defined by Equation 4.3.

$$R^\star = \frac{-2\gamma}{\Delta g} = \frac{R_0}{\ln\left(\frac{X_C \cdot X_{Nb}}{K_S}\right)} \tag{4.3}$$

where $R_0 = \frac{2\gamma v_{NbC}}{kT}$ is the capillary radius, i.e., a characteristic length scale depending on surface tension between the particle and the matrix. The nucleation barrier is then defined by the value

of $\Delta G$ at $R^\star$ (Equation 4.4).

$$\Delta G^\star = \frac{16}{3}\pi\frac{\gamma^3}{\Delta g^2} = \frac{\Delta G_0}{\left(\ln\left(\frac{X_C \cdot X_{Nb}}{K_S}\right)\right)^2} \tag{4.4}$$

where $\Delta G_0 = \frac{4}{3}\pi R_0^2\gamma$. Finally classical nucleation theory gives the nucleation rate defined by Equation 4.5 [53].

$$\left.\frac{dN}{dt}\right|_{nucl} = N_0 Z\beta^\star e^{\frac{-\Delta G^\star}{kT}}\left(1 - e^{\frac{-t}{\tau}}\right) \tag{4.5}$$

where:

- $N_0$ is the number of nucleation sites per volume unit : $N_0 = \frac{1}{v_{Fe}} = \frac{2}{a_{Fe}^3}$ [54]
- Z is the Zeldovich factor : $Z = \frac{v_{NbC}}{2\pi R^{\star 2}}\sqrt{\frac{\gamma}{kT}}$ [55]
- $\beta^\star$ is the condensation rate : $\beta^\star = \frac{4\pi R^{\star 2} D_{Nb} X_{Nb}}{a_{Fe}^4}$ [56]
- $\tau$ is the incubation time for nucleation : $\tau = \frac{4}{2\pi\beta^\star Z^2}$ [53]

### 4.3.2 Growth

Precipitate growth is assumed to be governed by the diffusion of atoms in the matrix. The precipitates "see" an infinite matrix where the solute concentration is constant. Under the assumption that the precipitate concentration (in terms of Nb and C) is higher than the matrix concentration and there is local equilibrium at the precipitate/matrix interface, the variation of the radius over time is given by Equation 4.6 [57].

$$\frac{dR}{dt} = \frac{D_C}{R}\frac{X_C - X_C^i}{X_p\frac{v_{Fe}}{v_{NbC}} - X_C^i} = \frac{D_{Nb}}{R}\frac{X_{Nb} - X_{Nb}^i}{X_p\frac{v_{Fe}}{v_{NbC}} - X_{Nb}^i} \quad \text{with} \quad D_x = D_x^0 \cdot e^{\frac{-Q_x}{k_B T}} \tag{4.6}$$

where $D_x$ is the diffusion coefficient of the solute ($D_{Nb}$ for Nb and $D_C$ for C), $X_x$ (x = Nb or C) is the atomic concentration of the solute in the matrix, $X_x^i$ is the concentration of the solute at

the interface, $X_p$ is the concentration in the precipitates ($X_p^{Nb} = X_p^C = 0.5$), $Q_x$ is the activation energy for the solute in ferrite and T is the temperature. A quasi-stationary profile is assumed for the concentration at the interface, i.e., $X(r) = X - \frac{R}{r}(X - X^i)$ [43].

The Gibbs-Thomson effect or curvature effect also affects the apparent solubility product at the interface $K_S^i(R)$ defined by Equation 4.7.

$$K_S^i(R) = K_S \, e^{\frac{R_0}{R}} \tag{4.7}$$

where $K_S^i(R) = X_{Nb}^i \cdot X_C^i$. Therefore the System 4.8 has to be solved in order to determine $X_{Nb}^i$ and $X_C^i$.

$$\begin{cases} \dfrac{D_{Nb}}{R} \dfrac{X_{Nb} - X_{Nb}^i}{X_p \frac{v_{Fe}}{v_{NbC}} - X_{Nb}^i} = \dfrac{dR}{dt} = \dfrac{D_C}{R} \dfrac{X_C - X_C^i}{X_p \frac{v_{Fe}}{v_{NbC}} - X_C^i} \\ X_{Nb}^i \cdot X_C^i = K_S \, e^{\frac{R_0}{R}} \end{cases} \tag{4.8}$$

Because $X_p^C >> X_C^i$ and $X_p^{Nb} >> X_{Nb}^i$, Equation 4.9 is obtained.

$$(X_{Nb}^i)^2 + X_{Nb}^i \left( \frac{D_C}{D_{Nb}} X_C - X_{Nb} \right) - \frac{D_C}{D_{Nb}} K_S \, e^{\frac{R_0}{R}} = 0 \tag{4.9}$$

with the solution defined by Equation 4.10.

$$X_{Nb}^i(T) = \frac{1}{2} \left[ X_{Nb} - \frac{D_C}{D_{Nb}} X_C + \sqrt{\left( \frac{D_C}{D_{Nb}} X_C - X_{Nb} \right)^2 + 4 \frac{D_C}{D_{Nb}} K_S \, e^{\frac{R_0}{R}}} \right] \tag{4.10}$$

The growth rate equation is therefore defined by Equation 4.11 using Equation 4.6 and Equation 4.10.

$$\left. \frac{dR}{dt} \right|_{growth} = \frac{D_{Nb}(T)}{R} \frac{X_{Nb} - X_{Nb}^i(T)}{X_p \frac{v_{Fe}}{v_{NbC}} - X_{Nb}^i(T)} \tag{4.11}$$

### 4.3.3 Coarsening

As mentioned previously, the coarsening stage is entirely included in the growth stage, due to the Gibbs-Thomson effect that governs the transition between coarsening and dissolution of a precipitate.

At the beginning of precipitation, all the precipitates will be larger than the critical radius (because of an elevated concentration in Nb and C in the matrix). Due to growth of the precipitates, the concentration in the matrix will decrease. The change in concentration will affect the value of the critical radius, i.e., a decrease in concentration will increase the critical radius. At some point, the change in critical radius will not be balanced by the growth of the smallest precipitates, so no more nucleation will occur. The smallest precipitates will dissolve while the larger ones will grow. This is the beginning of the coarsening stage. In the end, when all the atoms of the limiting reactant are consumed, coarsening stops. This is the end of precipitation.

## 4.4 Input parameters

Many parameters are needed in order to implement the 'Multipreci' model. However, the key parameters, $K_S$ and $D_{Nb}$, are not well known. Many different studies have provided very different values. In [43] the author implemented the 'Multipreci' model for isothermal NbC precipitation and utilized the parameters presented in Table 4.1. Therefore, since the same phenomenon is simulated in the present work, the same parameters are utilized. Other parameters have to be taken into account, such as the initial composition of the steel (Nb and C) and the laminar cooling parameters.

## 4.5 Laminar cooling parameters

During the last stage of TMCP, the steel plate is cooled from the finish rolling temperature (FRT) to the coiling temperature (CT). The cooling is continuous; a succession of water banks allows control of the cooling rate (CR). The temperature profiles at the surface and at the centerline

TABLE 4.1 – Input parameters [43].

| Parameter | Symbol | Value |
|---|---|---|
| Lattice parameters | $a_{Fe}$ (Å) | 2.866 |
| | $a_{NbC}$ (Å) | 4.47 |
| Diffusion pre-factors (in ferrite) | $D^0_{Nb}$ ($m^2.s^{-1}$) | $5 \cdot 10^{-3}$ |
| | $D^0_C$ ($m^2.s^{-1}$) | $2 \cdot 10^{-6}$ |
| Activation energies (in ferrite) | $Q_{Nb}$ ($kJ.mol^{-1}$) | 251.4 |
| | $Q_C$ ($kJ.mol^{-1}$) | 84.6 |
| Interface energy of NbC in ferrite | $\gamma$ ($J.m^{-2}$) | 0.73 |
| $\ln(K_S) = B - \frac{A}{T}$ | A (K) | 14560 |
| | B | -7.33 |

will obviously be different. However, it is possible to consider the cooling rate as constant for most of the steel. Figure 4.1 shows a simulation of the temperature profile at the centerline of a TWX70 steel plate [48] and the approximation of a constant cooling rate for the modeling of NbC precipitation.

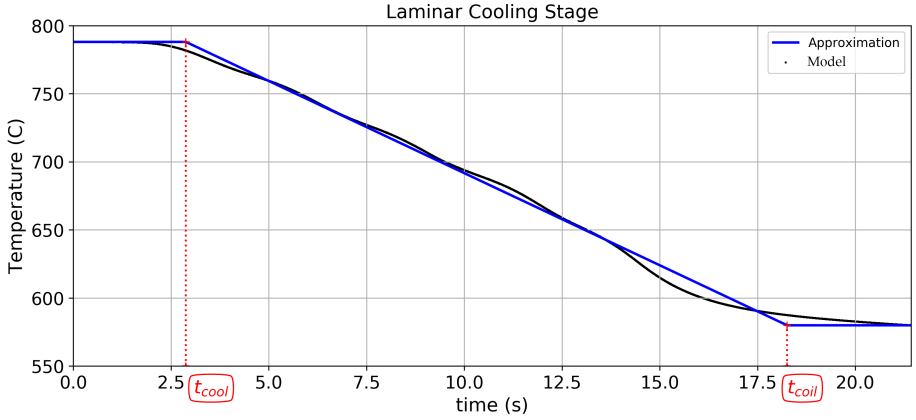


FIG. 4.1 – Laminar cooling temperature profile (centerline of TWX70 steel).

The last input parameters that are needed for the simulation of the NbC precipitation kinetic are the laminar cooling parameters :

- FRT : the finish rolling temperature (in °C);

- $t_{cool}$ : time at which laminar cooling begins (in s);
- CT : the coiling temperature (in °C);
- $t_{coil}$ : time at which laminar cooling stops (in s) and coiling starts.

Then the constant cooling rate is defined by Equation 4.12.

$$CR = \frac{FRT - CT}{t_{cool} - t_{coil}} \tag{4.12}$$

## 4.6 Numerical resolution

The Lagrange 'Multipreci' approach discretizes the particle size distribution into size classes of precipitates. The system is not described by a single value (e.g., mean radius); all precipitates are tracked. Precipitates of the same size are grouped into one unique class. Therefore, during the simulation, the evolution of each size class is determined. At each time step the concentration of solutes (Nb and C) in solid solution, the number of different classes and the radius and number of precipitates of each class are updated. The five variables are the key information for any further calculation such as the volume fraction, size distribution, concentration profile, etc. In order to implement Equations 4.5 and 4.11, they must be discretized.

### 4.6.1 Nucleation

At the beginning of each time step, a new class is created and the number of precipitates is given by Equation 4.13.

$$\Delta N = \left.\frac{dN}{dt}\right|_{nucl} \Delta t \qquad \text{where} \quad \left.\frac{dN}{dt}\right|_{nucl} = N_0 Z \beta^\star e^{\frac{-\Delta G^\star}{kT}} \left(1 - e^{\frac{-t}{\tau}}\right) \tag{4.13}$$

The radius of this class of precipitates is defined by $R' = R^\star + \frac{1}{2}\sqrt{\frac{kT}{\pi\gamma}}$ [43].

### 4.6.2 Growth and dissolution

After the nucleation stage, all the pre-existing precipitates undergo the growth (or dissolution) stage. At each time step, the new radius for each class of precipitates is given by Equation 4.14.

$$R(t + \Delta t) = R(t) + \left.\frac{dR}{dt}\right|_{growth} \Delta t \qquad \text{where} \qquad \left.\frac{dR}{dt}\right|_{growth} = \frac{D_{Nb}}{R} \frac{X_{Nb} - X^{i}_{Nb}}{X_p \frac{v_{Fe}}{v_{NbC}} - X^{i}_{Nb}} \tag{4.14}$$

If $X_{Nb} - X^{i}_{Nb} > 0$, the radius of the precipitates increases, i.e., it undergoes the growth stage. If $X_{Nb} - X^{i}_{Nb} < 0$, the precipitates are not stable (due to the Gibbs-Thomson effect). Therefore they are dissolved and the atoms within the particles go back into solid solution.

Figure 4.2 shows a scheme that details the nucleation and growth sequence that happens at each time step, for all classes. At each time step, a new class is created and all pre-existing classes grow (in the case where $X_{Nb} - X^{i}_{Nb} > 0$). At the end of the calculation, the mean radius of the final distribution, the volume fraction and, consequently, the precipitation strengthening [1] are calculated using Equation 4.15.

$$\sigma_{ppt}(MPa) = \left(\frac{10.8 f_v^{\frac{1}{2}}}{2R_{mean}}\right) \ln\left(\frac{2R_{mean}}{6.125 \cdot 10^{-4}}\right) \tag{4.15}$$

where $\sigma_{ppt}$ is the precipitation strengthening contribution in MPa, $f_v$ is the volume fraction of precipitates and $R_{mean}$ is the mean radius in µm.

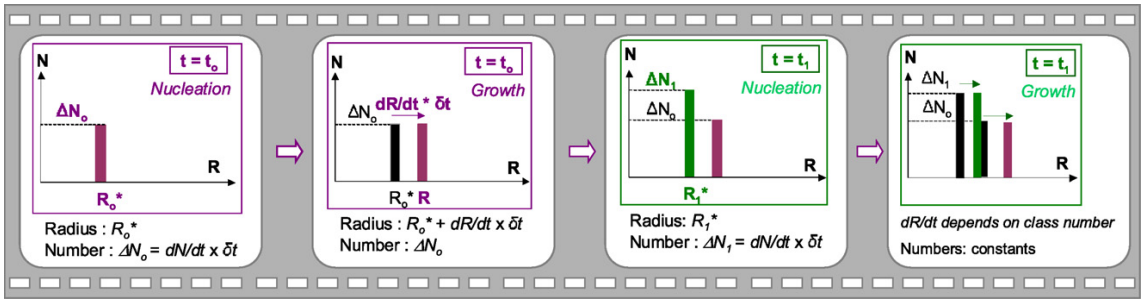


FIG. 4.2 – Nucleation and growth sequence [44].

### 4.6.3 Timestep

For this work, $t_{end}$ does not exceed $10^2$ s. Thus a constant time step that provides stability and accuracy while remaining time efficient was implemented. Figure 4.3 shows calculations for the mean precipitate radius, for an X70 steel at five different time steps, i.e., $\Delta t$ = 50, 25, 10, 5 and 1 ms. The difference is less than 0.05 nm between $\Delta t$ = 50 ms and $\Delta t$ = 1 ms. The latter is obviously a bit more precise, but time consuming. A timestep of 25 ms was chosen for the subsequent simulations. Each simulation takes less than a minute to run.

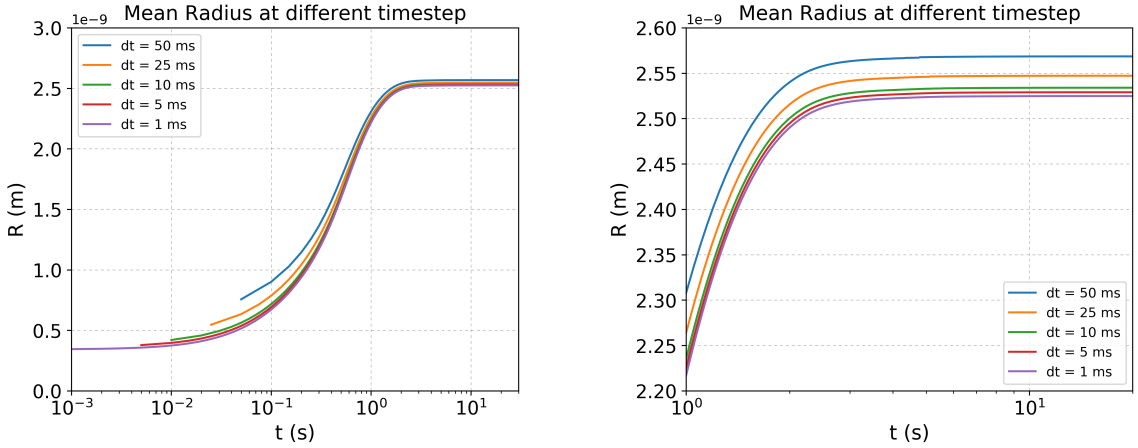


(A) (B)

FIG. 4.3 – Simulation of the mean radius over time for X70 steel, for different $\Delta t$ values: (A) Overall results and (B) zoom.

## 4.7 Results

The chosen language for implementation is Python (the entire code is found in Appendix A). Two sets of calculations were done in order to test the NbC precipitation simulations. The first one is composed of the five X70/X80 steels analyzed in [2], while the second one is of the two X70 steels analyzed in the present work, i.e., a conventional X70 steel and a thick wall X70 (TWX70).

The difficult part was to assess the time schedule, i.e., where to start and stop cooling. Even if there is an approximation from the temperature profile simulation, the real experimental conditions are far more difficult to know. Assuming that the distance between finish rolling and the runout table is approximatively 7 m (23 ft), and the speed of the skelp is about 3.12 m/s, the time spent by the skelp between finish rolling and the start of the runout table is 2.25 s.

### 4.7.1 Lu's steels [2]

Table 4.2 presents the simulation results for Lu's steels (X70/X80), i.e., the predicted mean radii and volume fractions. The results will be discussed and compared with the experimental results in Chapter 7.

TABLE 4.2 – Results for Lu's steels [2].

| Sample | wt% C | wt% Nb | FRT (°C) | CT (°C) | CR (°C/s) | $t_{cool}$ (s) | $t_{coil}$ (s) | $R_{mean}^{model}$ (nm) | $f_v^{model}$ (%) | $\sigma_{ppt}^{model}$ (MPa) |
|---|---|---|---|---|---|---|---|---|---|---|
| X70-564 | 0.0398 | 0.069 | 744 | 588 | 15 | 2.25 | 12.65 | 2.04 | 0.019 | 87.7 |
| X80-462 | 0.03 | 0.091 | 744 | 588 | 15 | 2.25 | 12.65 | 2.48 | 0.032 | 109.2 |
| X80-A4B | 0.035 | 0.094 | 829 | 527 | 15 | 2.25 | 22.38 | 4.53 | 0.107 | 156.1 |
| X80-B4F | 0.052 | 0.077 | 788 | 566 | 15 | 2.25 | 17.05 | 2.88 | 0.087 | 171.5 |
| X80-A4F | 0.052 | 0.044 | 788 | 510 | 15 | 2.25 | 20.78 | 3.16 | 0.017 | 73.6 |

### 4.7.2 Conventional and thick wall X70 steels

Table 4.3 presents the simulation results for the X70 steels. Figures 4.4 and 4.5 present the detailed results for X70 and TWX70 steels.

TABLE 4.3 – Simulation results for the X70 and TWX70 steels.

| Sample | wt% C | wt% Nb | FRT (°C) | CT (°C) | CR (°C/s) | $t_{cool}$ (s) | $t_{coil}$ (s) | $R_{mean}^{model}$ (nm) | $f_v^{model}$ (%) | $\sigma_{ppt}^{model}$ (MPa) |
|---|---|---|---|---|---|---|---|---|---|---|
| X70 | 0.052 | 0.09 | 790 | 575 | 15 | 2.25 | 16.58 | 2.55 | 0.10 | 143.9 |
| TWX70 | 0.043 | 0.067 | 790 | 575 | 15 | 2.25 | 16.58 | 3.87 | 0.06 | 89.6 |

The first graph shows the evolution over time for the mean radius and the critical radius ($R^*$, Equation 4.3). The final mean radius for TWX70 steel (3.87 nm) is larger than that for X70 steel (2.54 nm). For both steels, the critical radius has a particular profile over time, where a maximum is reached at t = 6 s (T = 734°C). The critical radius is a function of T and composition

as defined by Equation 4.3. Both the composition and the temperature decrease during laminar cooling. At one point equilibrium between temperature and composition is reached. This is why a maximum for the critical radius is observed. The next graph shows the evolution over time of the solid solution concentrations in ferrite (in terms of at% Nb an at% C). For both steels, concentrations decrease because of precipitation. The main difference is that a significant part of Nb (0.011 wt%) remains in solid solution for TWX70 steel. Only 0.00008 wt% Nb remains in solid solution for X70 steel. The third graph displays the evolution over time of the volume fraction (in %) of precipitates. The final volume fraction of precipitates for X70 steel (0.10 %) is larger than that for TWX70 steel (0.06 %). The next graph shows the evolution over time of the number of precipitates per $\mu m^3$ in ferrite. The final number of precipitates for X70 steel ($1.4 \cdot 10^{22}$ $m^{-3}$) is also larger than that for TWX70 steel ($2.5 \cdot 10^{21}$ $m^{-3}$). The fifth graph displays the evolution over time of the nucleation rate (in $\mu m^{-3} s^{-1}$). When the nucleation rate becomes equal to zero, i.e., at t = 0.8 s for X70 steel and at t = 2 s for TWX70 steel, no more nucleation occurs and only precipitation coarsening is ongoing. Finally, the last graph shows the temperature profile during laminar cooling used for the simulations (same as Figure 4.1). In this model the skelp thickness was not an input parameter. The differences that are observed between the two simulations are only due to the difference in chemistry.

## 4.8 Summary

Precipitation of NbC in different steels was simulated using the 'Multipreci' algorithm coupled with laminar cooling conditions. The results allowed for prediction of the contribution of precipitation to the global strength of the steel. All assumptions used in the model are discussed in Chapter 7. The results are also discussed and compared with experimental measurements obtained from the matrix dissolution technique.

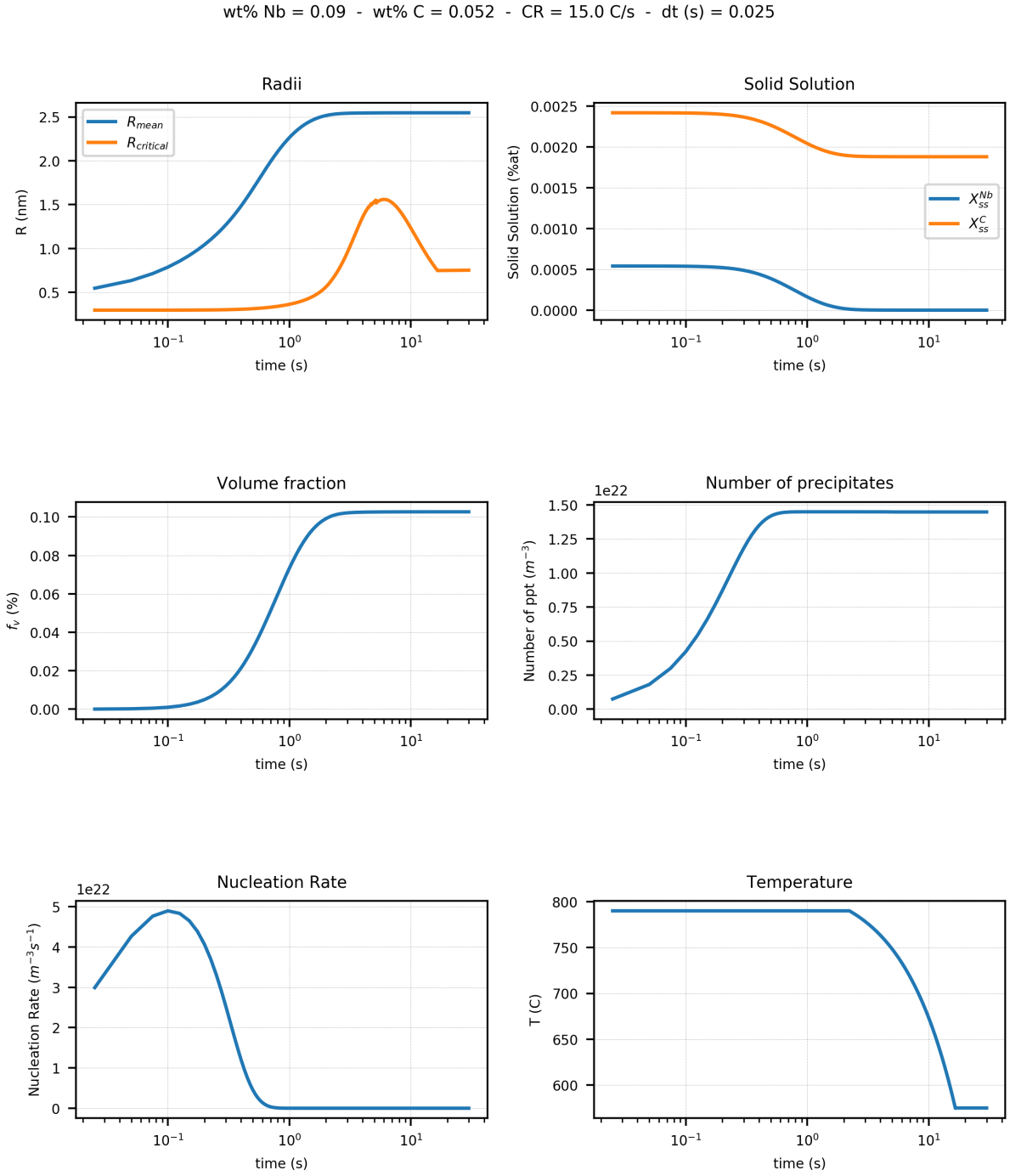


FIG. 4.4 – Modeling of NbC precipitation during laminar cooling for X70 steel.

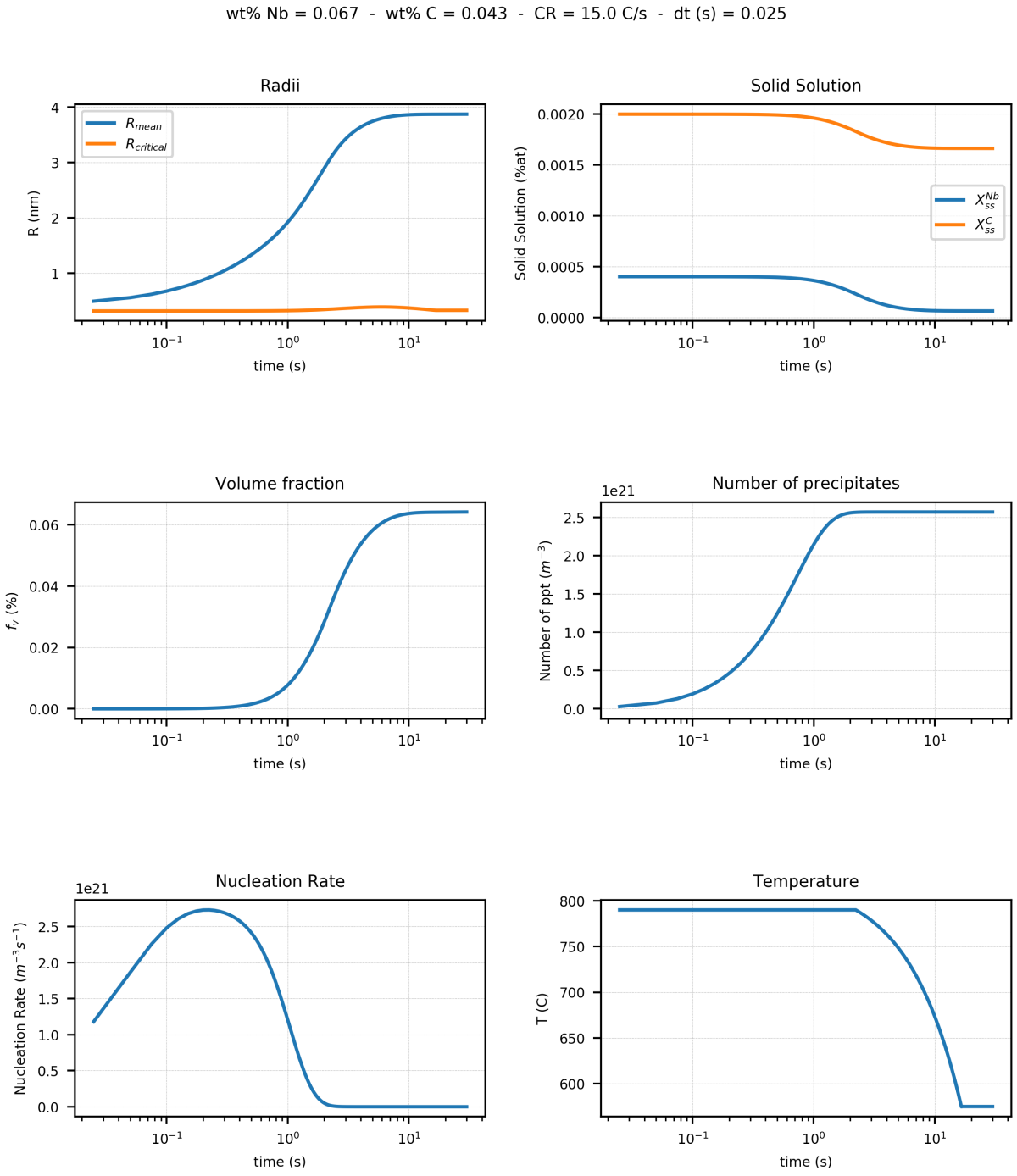


FIG. 4.5 – Modeling of NbC precipitation during laminar cooling for TWX70 steel.

# Chapter 5

# X70 and TWX70 steels

Chapter 3 presented all the experimental procedures that were used to characterize and quantify both the steels and the precipitates collected from the matrix dissolution technique. This chapter presents the characterization results for the X70 and TWX70 steels.

The steel samples were first characterized by SEM to determine their microstructure and their grain sizes (more specifically their mean linear intercepts, which is an approximation of the grain size). ICP analysis was conducted on the supernatant solution to measure the amount of each alloying element in solution. QXRD analysis was carried out on the collected precipitates in order to quantify the relative abundance of each type of precipitate, their mean size and strain and their composition. Finally, SEM-EDX analysis was performed on extracted powders to determine the shape, composition and size distribution of the different precipitates. The QXRD and ICP results were compared in order to close the mass balance and to give some confidence about the analysis.

The main difference between the X70 and TWX70 steels is their thickness. The steel compositions are similar, although the Nb/C ratio is 1.73 for the X70 and 1.56 for the TWX70, as are the processing conditions. Therefore, the main objective was to determine any effect of skelp thickness on precipitation. The second objective was to determine the effect of the precipitation on steel properties (microstructure and mechanical properties).

## 5.1 Microstructural analysis - grain size measurement

Quarter thickness samples for both X70 and TWX70 steels were analyzed to determine their microstructures and their grain sizes (through a mean linear intercept method).

### 5.1.1 SEM secondary electron (SE) imaging analysis

Figure 5.1 shows inverted SEM SE images of a polished and etched X70 sample taken at low and high magnifications. The microstruture is mainly polygonal ferrite. Some very large TiN-rich precipitates were also observed (images are displayed in Appendix C).

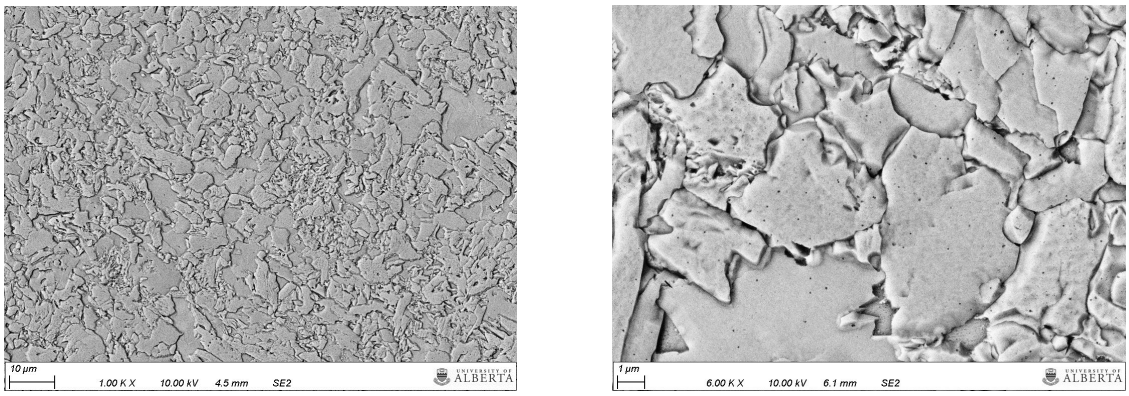


(A) (B)

FIG. 5.1 – SEM SE images of X70 steel: (A) Lower magnification and (B) higher magnification.

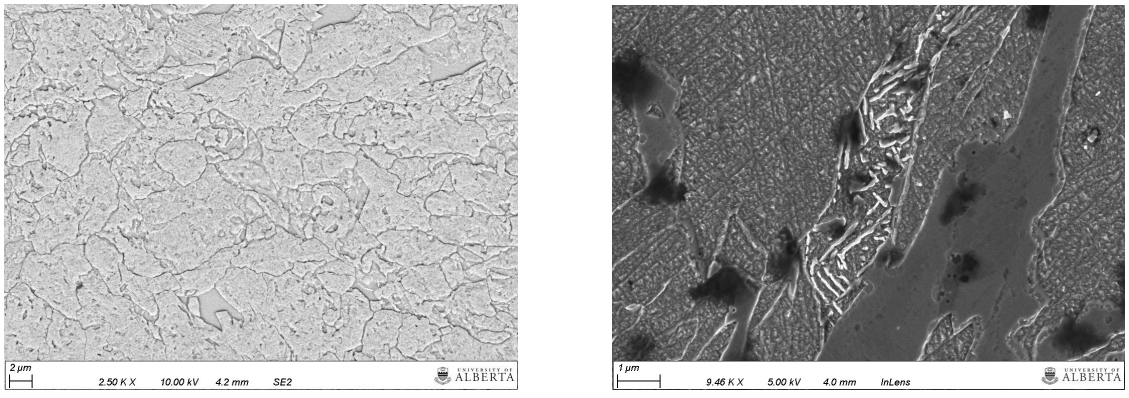


(A) (B)

FIG. 5.2 – SEM SE images of TWX70 steel: (A) SE image and (B) in-lens SE image.

The same type of microstructure was observed for TWX70 steel. It is mainly polygonal ferrite with some pearlite structure. Figure 5.2 shows an inverted SEM SE image of a TWX70 steel and an in-lens SE image of the same steel taken at higher magnification showing a pearlitic region. An in-lens detector is used to obtain high-contrast images.

### 5.1.2 EBSD analysis

Figure 5.3 shows EBSD images of X70 (A) and TWX70 (B) steels. A step size of 100 nm per pixel was used. A polygonal ferrite structure is observed for both steels. Grain boundaries are defined as having a misorientation greater than 15 degrees.

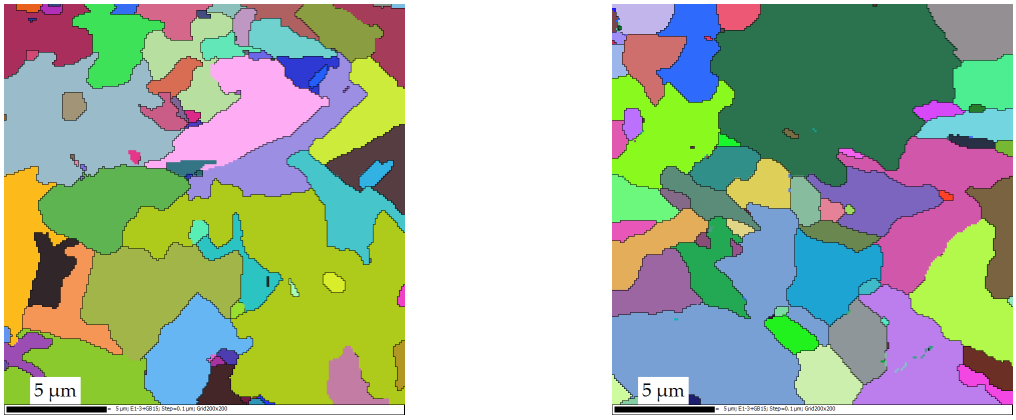


(A) (B)

FIG. 5.3 – EBSD images: (A) X70 steel and (B) TWX70 steel.

SEM SE and EBSD analysis provides some qualitative information about the structure and the size of the grains. However, in order to provide quantitative data regarding the grain size a mean linear intercept method (m.l.i.) was utilized.

### 5.1.3 Mean linear intercept measurements

Table 5.1 and Figure 5.4 present m.l.i. measurements for both steels, using SEM and EBSD images. SEM and EBSD measurements are consistent for the X70 steel and give an m.l.i. of about 2.6 µm. For the TWX70 steel, the results are different for the two methods but lie within

the standard deviation range. TWX70 has a higher m.l.i. value with a larger standard deviation ($\sigma$).

TABLE 5.1 – Mean linear intercept (m.l.i.) measurements for X70 and TWX70 steels

| m.l.i. SEM-SE | X70 | TWX70 |
|---|---|---|
| Mean (µm) | 2.61 | 4.87 |
| Median (µm) | 2.15 | 3.96 |
| $\sigma$ (µm) | 1.76 | 3.44 |

| m.l.i. EBSD | X70 | TWX70 |
|---|---|---|
| Mean (µm) | 2.57 | 2.98 |
| Median (µm) | 2.10 | 2.19 |
| $\sigma$ (µm) | 1.60 | 2.57 |

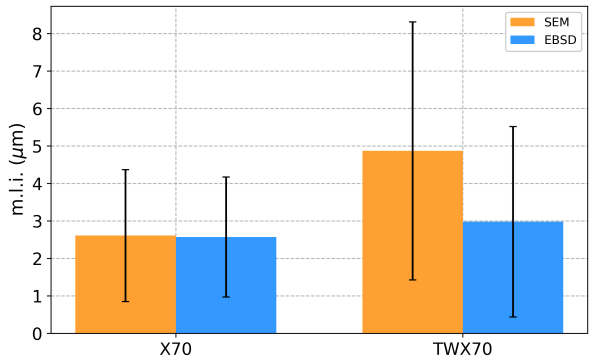


FIG. 5.4 – Mean linear intercept for X70 and TWX70 steels.

## 5.2 Chemical dissolution of the steel matrix

Table 3.3 (in Chapter 3) displays the dissolution results. The two X70 steels have similar yields (ratio between the mass of collected powders and the mass of the dissolved piece of steel), with 0.14% for the X70 steel and 0.12% for the TWX70 steel.

## 5.3 ICP measurements

Dissolution provides two samples for analysis, i.e., the extracted precipitates and the supernatant solution. ICP analysis was done on the latter in order to estimate the amount of each alloying element that remained in solution. Based on the amount of each element in the steel

and the measured amount of each element in solution, simple subtraction yields the element amount that is present in precipitate form.

### 5.3.1 X70 steel

Table 5.2 and Figure 5.5(A) show the ICP measurements and the calculated amount in precipitate form for X70 dissolution. The amounts of Nb and Ti that remain in solution are quite low compared with their nominal compositions in the steel. Figure 5.5(B) shows that most of the Nb (94%) and Ti (74%) appear to be in precipitate form. A significant amount of Mo (13%) is present in precipitate form. Most of the Mo is, therefore, in solution after dissolution. Cr appears to be all in solution after dissolution. The measured amount of Cr is even higher than the steel composition. This could be due to the precision of the measurement or to an actual higher concentration in the dissolved piece. No Cr is then present in the collected precipitates. A low amount of V (0.003 wt%) is present in the steel composition and only 13% appears in precipitate form (0.0004 wt%).

The calculated phase diagrams (with ThermoCalc 2017a, TCFE6 Steels/Fe-alloys database) give solubilities at room temperature in ferrite of 19.23 wt% for V, 0.025 wt% for Cr, $2.4 \cdot 10^{-4}$ wt% for Ti, $1 \cdot 10^{-4}$ wt% for Nb and $4 \cdot 10^{-6}$ wt% for Mo. It is difficult to provide interpretations to these results. Assuming the solutes are in equilibrium, this would indicate that most of solutes that remain in acidic solution after dissolution were not in solid solution in ferrite. However, the solutes in solid solution are not in equilibrium.

TABLE 5.2 – ICP measurements and calculated amount in precipitate form for X70 steel.

| Analyte | Steel (wt%) | Solution (wt%, measured) | Equilibirum (wt%) | In precipitate (wt%, calculated) |
|---|---|---|---|---|
| Ti | 0.016 | 0.0042 | $2.4 \cdot 10^{-4}$ | 0.0118 |
| Nb | 0.090 | 0.005 | $1 \cdot 10^{-4}$ | 0.085 |
| Mo | 0.137 | 0.119 | $4 \cdot 10^{-6}$ | 0.018 |
| V | 0.003 | 0.0026 | 19.23 | 0.0004 |
| Cr | 0.23 | 0.235 | 0.025 | -0.005 |

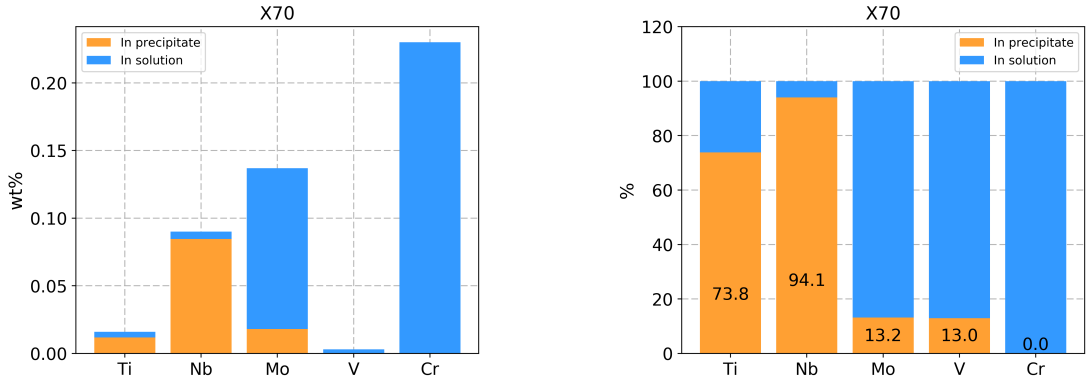


(A) (B)

FIG. 5.5 – ICP results for X70 steel: (A) wt% and (B) relative amounts.

### 5.3.2 TWX70 steel

Table 5.3 and Figure 5.6(A) show the ICP measurements and the calculated amounts in precipitate form for TWX70 dissolution. The amounts of Nb and Ti that remain in solution are also quite low compared with their nominal compositions in the steel. Figure 5.6(B) shows that most of the Nb (96%) and Ti (98%) are in precipitate form. A small amount of Mo (8%) is present in precipitate form, with most being in solution after dissolution. Cr is mostly in solution (6% in precipitate form). As with the X70 steel, a low amount of V (0.003 wt%) is present in the steel composition and only 13% appears in precipitate form (0.0004 wt%).

TABLE 5.3 – ICP measurements and calculated amount in precipitate form for TWX70 steel.

| Analyte | Steel (wt%) | Solution (wt%, measured) | Equilibirum (wt%) | In precipitate (wt%, calculated) |
|---|---|---|---|---|
| Ti | 0.016 | 0.0003 | $2.4 \cdot 10^{-4}$ | 0.0157 |
| Nb | 0.067 | 0.003 | $1 \cdot 10^{-4}$ | 0.064 |
| Mo | 0.192 | 0.177 | $4 \cdot 10^{-6}$ | 0.015 |
| V | 0.003 | 0.0023 | 19.23 | 0.0007 |
| Cr | 0.09 | 0.085 | 0.025 | 0.005 |

### 5.3.3 ICP summary

The ICP analysis showed that Cr, Mo and V remain mostly in solution. Conversely, the Nb and Ti levels in solution were very low for both steels. However, the measured amounts remaining

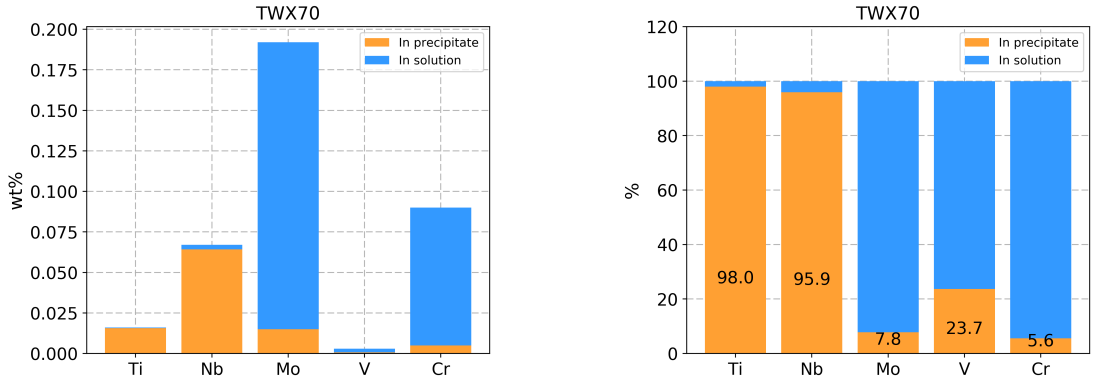


(A) (B)

FIG. 5.6 – ICP results for TWX70 steel: (A) wt% and (B) relative amounts.

in solution after dissolution are above the equilibrium amounts for both steels. Nevertheless, the solutes cannot be considered to be in equilibrium in the steel because of the processing conditions. In additions, the equilibrium calculations were done for simple binary systems such as Fe-Nb or Fe-Ti and not complex system such as Fe-Nb-Ti-Cr-Mo. The precipitates are mainly (Nb,Ti,Mo,V)-rich precipitates. It is reasonable to assume that the precipitates are complex carbonitrides, i.e., (Nb,Ti,Mo,V)(C,N) as expected. One way to determine amounts of precipitate types is through quantitative XRD analysis (QXRD).

## 5.4 SEM-EDX analysis of the collected precipitates

SEM imaging combined with EDX analysis provides both quantitative and qualitative information regarding the precipitates. Two kinds of samples were prepared:

1. Powders deposited on carbon tape on an Al stub, with a carbon coating (preparation #1).
2. A suspension with the particles deposited on carbon tape on an Al stub, with a carbon coating (preparation #2).

The first kind of sample allows for the examination of the global atomic composition (using EDX analysis) and the sizes and shapes of the precipitates. The second method provides a way to

look at the size distribution of the small precipitates. More information regarding preparation is given in Chapter 3, Section 3.6, page 27.

In addition, C and N compositions of the precipitates were not analyzed. It was difficult to measure the precipitate carbon content because of the presence of the carbon coating and carbon tape. Nitrogen content was also difficult to assess through EDX analysis because of the low relative intensity of the N peak in the EDX spectra. It was also difficult to measure the vanadium content because Ti and V peaks in the EDX spectrum were very close. Therefore, the deconvolution of the peaks resulted in measuring no V in precipitate form.

### 5.4.1 X70 steel

Figure 5.7 shows an SEM secondary electron (SE) image of the residue from an X70 steel (preparation #1). Two types of precipitates can be seen. The TiN-rich precipitates (cubic, colored in blue to help with identification) vary in size from $\simeq 1$ to $\simeq 4$ µm. Agglomerates of smaller precipitates surround the TiN-rich particles.

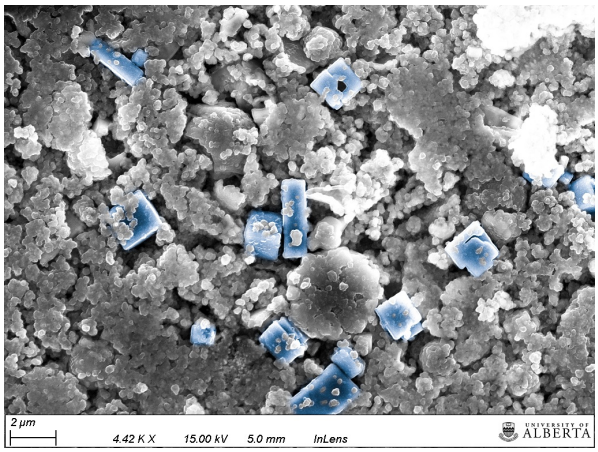


FIG. 5.7 – SEM SE image of precipitates collected from an X70 steel (TiN in blue, false color).

Figure 5.8(A) shows a higher magnification SEM image of a cubic TiN-rich precipitate surrounded by agglomerates of small precipitates. Figure 5.8(B) shows an SEM image of particles from preparation #2, where two sets of small precipitates (circled in red and green in Figure 5.8(B)) are highlighted. The particles appear spherical. The resolution of the SEM does not

allow for differentiation of the small agglomerates into single particles. It is possible that the red-circled precipitates are an agglomeration of smaller precipitates. A total of ten images was used to quantitatively analyze the size distribution. More images can be found in Appendix C.

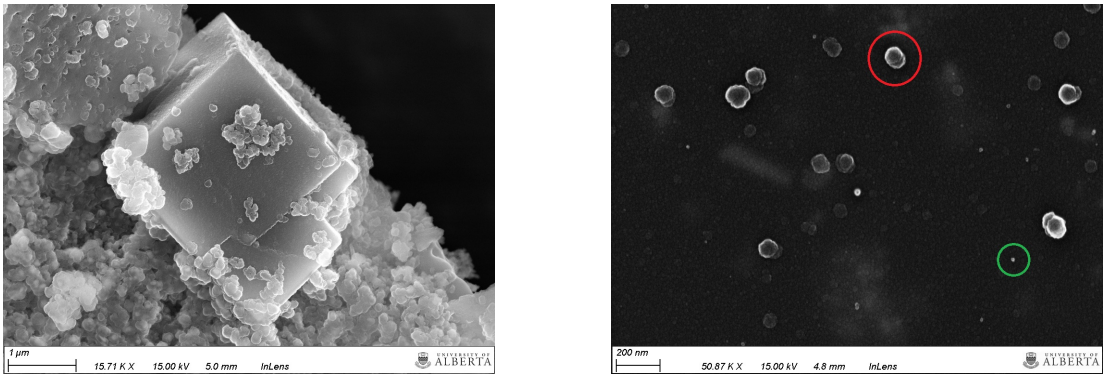


(A) (B)

FIG. 5.8 – SEM SE images of precipitates collected from an X70 steel: (A) TiN and (B) suspension (preparation #2).

Figure 5.9 presents the size distribution of the particles analyzed from preparation #2. The first set of particles shows an average size of 7.95 nm with a standard deviation of 2.19 nm. The second set of sizes varies from 40 to 70 nm (most likely agglomerates of smaller particles).

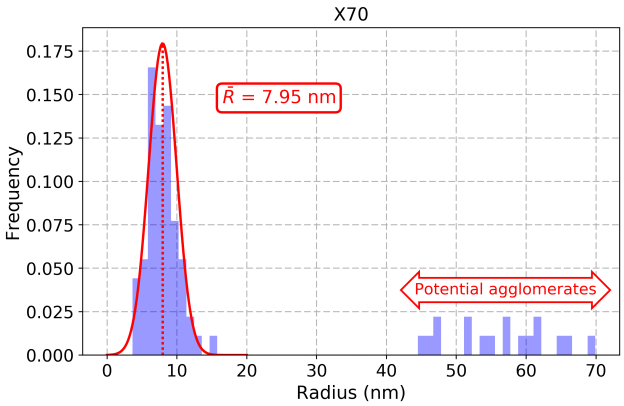


FIG. 5.9 – X70 steel precipitate size distribution from a total of 82 particles.

Figure 5.10 and Table 5.4 present the results of EDX analysis of the extracted precipitates. A total of 42 agglomerates of small precipitates and 30 large precipitates were analyzed. More EDX results can be found in the Appendix C. No V was seen by EDX analysis. The composition of the precipitates was assumed to be $(Ti_xNb_yMo_{1-x-y})(C,N)$ (with x + y + z = 1). A range of

compositions is found for the large precipitates, i.e., the Ti (x) content varies from 0.75 to 0.93 with an average of 0.87. A range of compositions occurs for the nano-precipitates as well with an average y value of 0.79 for Nb, an average x value of 0.16 for Ti and an average (1-x-y) value of 0.05 for Mo. Cr was not observed during EDX analysis.

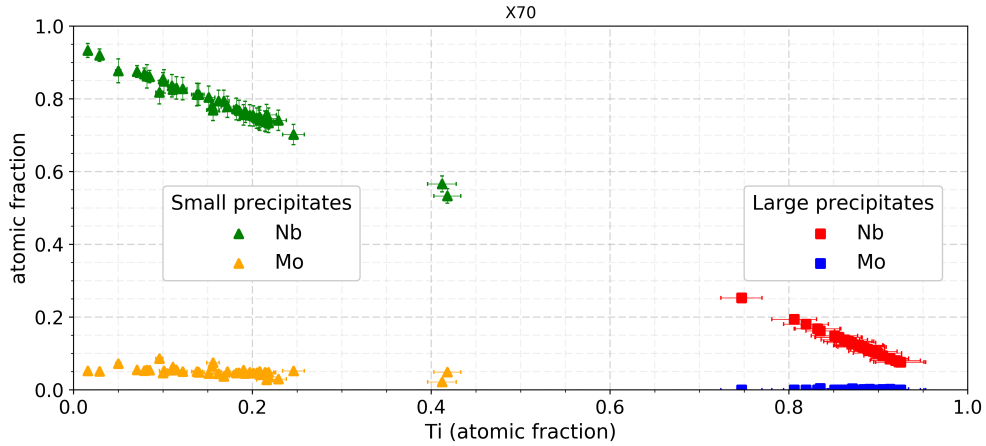


FIG. 5.10 – EDX analysis for precipitates extracted from X70 steel. The Nb content of the large precipitates is shown in red and the Mo content is shown in blue. The Nb content of the small precipitates is shown in green and the Mo content is shown in yellow.

TABLE 5.4 – EDX analysis for large (total of 30 particles) and small (total of 42 agglomerates) precipitates ($Ti_xNb_yMo_{1-x-y}$)(C,N) extracted from X70 steel (values in atomic fraction).

| Small | Ti | Mo | Nb |
|---|---|---|---|
| Average | 0.164 | 0.050 | 0.786 |
| StDev | 0.081 | 0.011 | 0.076 |

| Large | Ti | Mo | Nb |
|---|---|---|---|
| Average | 0.870 | 0.000 | 0.129 |
| StDev | 0.038 | 0.001 | 0.038 |

### 5.4.2 TWX70 steel

The same analysis was done for the extracted precipitates from TWX70 steel. Figure 5.11(A) shows an agglomerate of nanosized precipitates that has trapped a few large TiN-rich precipitates (colored in blue). Figure 5.11(B) shows an inverted SEM SE image of precipitates from preparation #2. Small particles are observed and appear spherical.

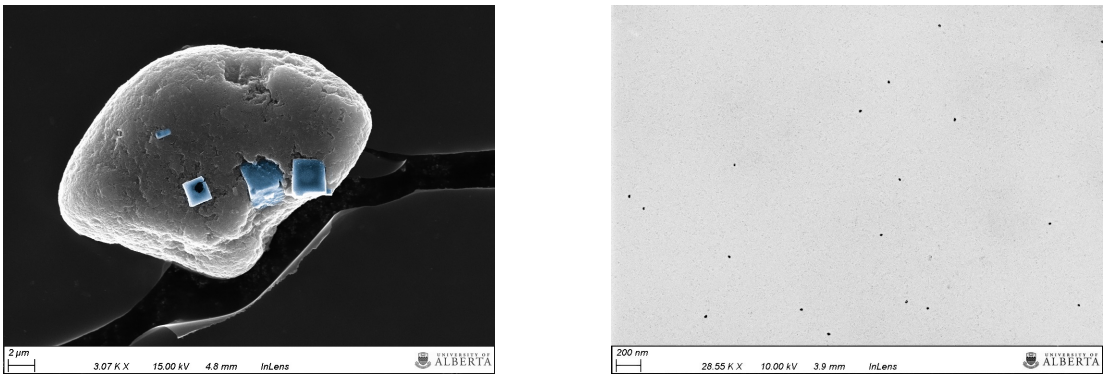


(A) (B)

FIG. 5.11 – SEM SE images of precipitates collected from TWX70 steel: (A) TiN (in blue, false color) and (B) suspension (preparation #2).

Figure 5.12 presents the size distribution of the small precipitates. The average precipitate size is 9.15 nm (radius) with a standard deviation of 2.19 nm, with a first peak at around 4.4 nm and a second peak at around 10 nm.

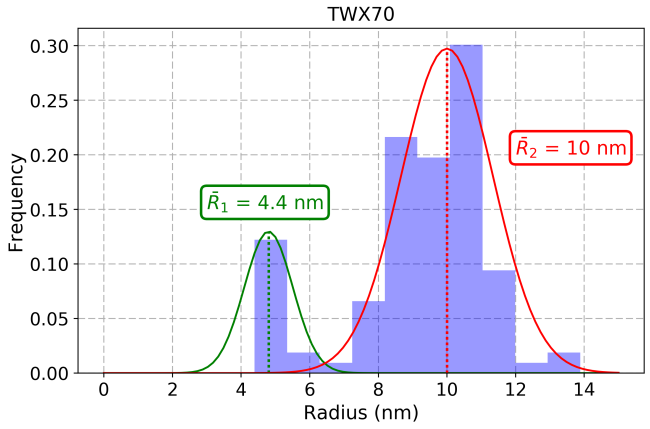


FIG. 5.12 – TWX70 steel precipitate size (particle radii) distribution from a total of 112 particles from preparation #2.

Figure 5.13, Table 5.5 and Table 5.6 present the EDX results obtained for the precipitates extracted from the TWX70 steel. A total of 37 agglomerates of small precipitates and 29 large precipitates were analyzed. No V was seen by EDX analysis. Three sets of precipitates were observed. The first set (labeled as large precipitates in red/blue in Figure 5.13) shows a range of Ti composition (x) from 0.73 to 0.95 with an average value of 0.87 and a standard deviation of 0.06. The second set (labeled as small precipitates, in yellow/green in Figure 5.13) shows a

range of Ti composition (x) with an average value of 0.16, as well as an average Nb compositon (y) of 0.74 and an average Mo composition (1-x-y) of 0.10. The third set (circled, also labeled as small precipitates, in yellow/green in Figure 5.13) shows a range of Ti composition (x) with an average value of 0.22, as well as an average Nb compositon (y) of 0.54 and an average Mo composition (1-x-y) of 0.24. Cr was not observed during EDX analysis.

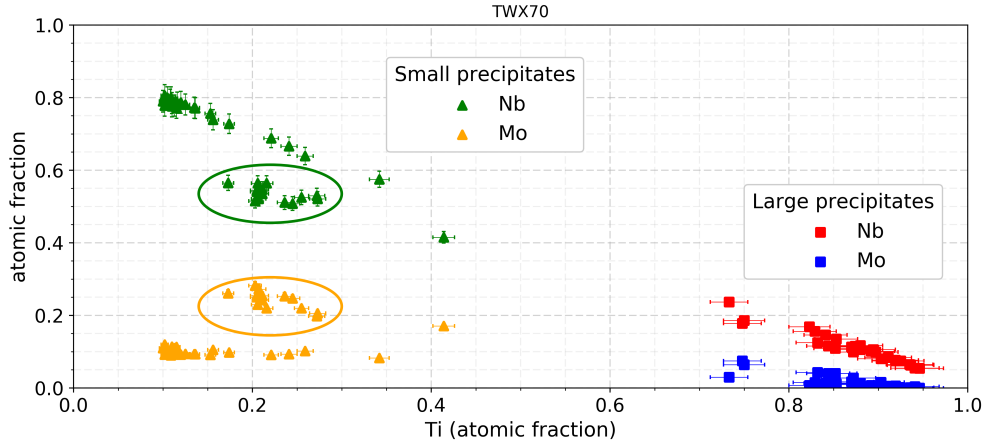


FIG. 5.13 – EDX analysis for precipitates extracted from TWX70 steel. The Nb content of the large precipitates is shown in red and the Mo content is shown in blue. The Nb content of the small precipitates is shown in green and the Mo content is shown in yellow.

TABLE 5.5 – EDX analysis for large precipitates $(Ti_xNb_yMo_{1-x-y})(C,N)$ from TWX70 steel (total of 29 particles). Values in atomic fraction.

| Large | Ti | Mo | Nb |
|---|---|---|---|
| Average | 0.873 | 0.016 | 0.111 |
| StDev | 0.057 | 0.019 | 0.043 |

TABLE 5.6 – EDX analysis for small precipitates $(Ti_xNb_yMo_{1-x-y})(C,N)$ from TWX70 steel (total of 37 agglomerates, values in atomic fraction).

| Small | Ti | Mo | Nb |
|---|---|---|---|
| Average | 0.159 | 0.102 | 0.738 |
| StDev | 0.083 | 0.018 | 0.091 |

| Circled | Ti | Mo | Nb |
|---|---|---|---|
| Average | 0.223 | 0.242 | 0.535 |
| StDev | 0.029 | 0.025 | 0.020 |

## 5.5 X-ray diffraction of the extracted precipitates

The collected powders are assumed to be composed of complex (Nb,Ti,Mo,V)(C,N) precipitates. Based on the EDX analysis, the extracted powders are composed of large TiNb-rich precipitates and small NbMoTi-rich precipitates. XRD can provide information about the lattice parameters (which depend on the diffraction angle and, thus, the peak positions), atomic composition (through the peak intensities) and the size and strain of the crystallites (through the shape of the peaks).

### 5.5.1 X70

Figure 5.14 presents XRD patterns obtained for the extracted powder from the X70 steel (first dissolution). X70 steel was the first sample to be dissolved and analyzed, which is why a small peak between $2\theta = 20^\circ$ and $2\theta = 30^\circ$ is observed. This broad peak is characteristic of amorphous $SiO_2$. This is the only case where the $SiO_2$ peak is present.

Two other sets of peaks are observed. Both are characteristic of a NaCl-type structure ($Fm\bar{3}m$ space group). XRD analysis was done using the XRD Jade software. The first set of peaks belongs to an NbC-rich structure, whereas the second set belongs to TiN-rich precipitates. No Mo or Cr carbides are seen by XRD analysis.

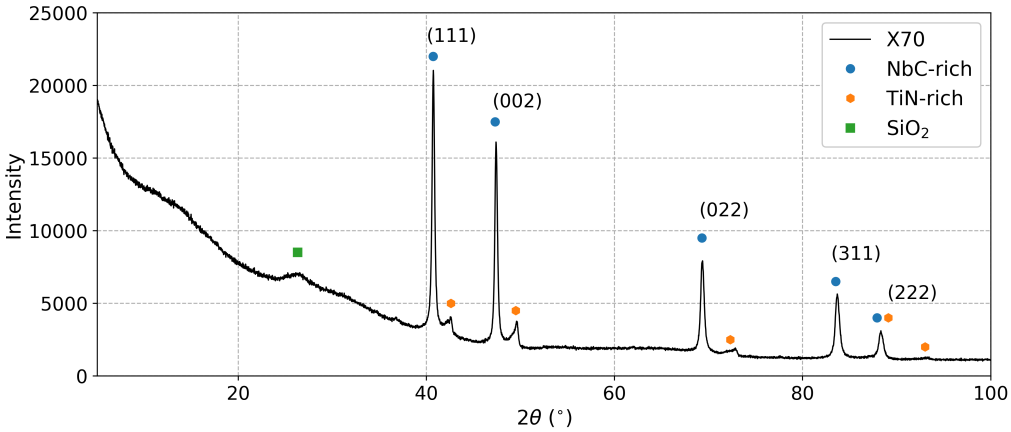


FIG. 5.14 – XRD pattern for collected precipitates from X70 steel.

### 5.5.2 TWX70

Figure 5.15 presents the XRD pattern obtained for the extracted powder from the TWX70 steel. Because of the set-up improvement (detailed in Chapter 3), the amorphous silica peak is not present in this pattern. Two sets of diffraction peaks are observed. Like the X70 extracted precipitates, both sets are consistent with a cubic structure ($Fm\bar{3}m$ space group), i.e., NbC-rich and TiN-rich precipitates. No Mo or Cr are seen by XRD analysis.

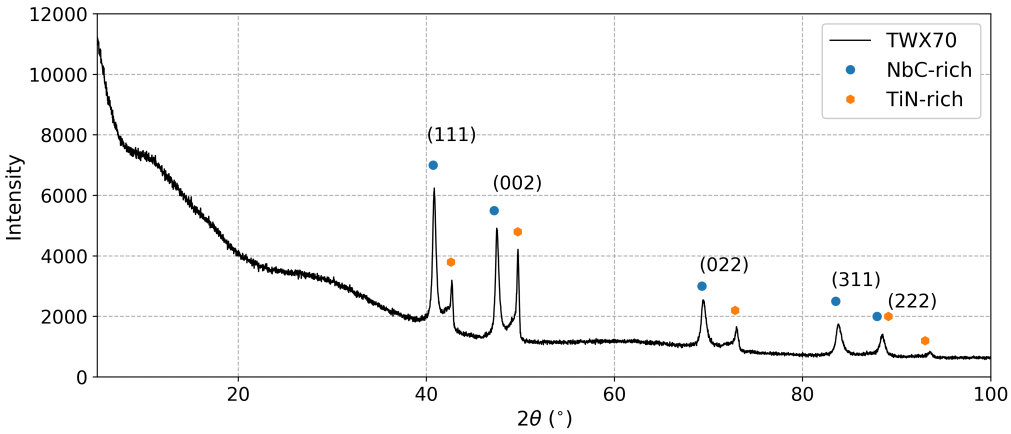


FIG. 5.15 – XRD pattern for collected precipitates from TWX70 steel.

### 5.5.3 XRD analysis summary

The initial analysis of XRD patterns provided information regarding the crystallographic structure of the precipitates. There appeared to be two similar cubic structures (NaCl-type) consistent with NbC-rich and TiN-rich type precipitates. Both steels exhibited the same types of precipitates. However, the intensities of the peaks showed that the relative amounts of TiN-rich and NbC-rich precipitates are different for the two steels. This is consistent with the ICP results, where it was found that the calculated amount of Ti in precipitate form is higher for the TWX70 steel. ICP analysis showed that the collected precipitates were (Nb,Ti,Mo,V)(C,N). Combination of XRD and ICP analyses shows that the extracted precipitates are Nb(Mo,Ti,V)C-rich and Ti(Mo,Nb,V)N-rich particles. Quantitative XRD analysis provides much more information regarding the compositions, sizes and amounts of each type of precipitates.

## 5.6 Rietveld refinement and QXRD analysis

The Rietveld refinement method is a crucial (and difficult) part of the precipitate analysis. The procedure is described in Chapter 3.

### 5.6.1 Adaptation of the refinement procedure

As presented in Chapter 3 section 3.3.3 two dissolutions were done for each steel. Figure 5.14 presented the XRD pattern from the first dissolution of X70 steel, which is representative of the two dissolution results. For this section, the XRD pattern of the second X70 steel dissolution (referred as X70-2 in this section) is taken as an example. The following development is only an explanation on how the refinement process was done. The actual QXRD analysis is detailed in the next section.

On closer examination of the different peaks in the XRD pattern, it was postulated that the TiN-rich set of peaks was not just one set (Figure 5.16), but a combination of many superimposed peaks. As such, there is not a unique composition of TiN-rich precipitates. This logic is also valid for the NbC-rich diffraction peaks, but less obvious at first.

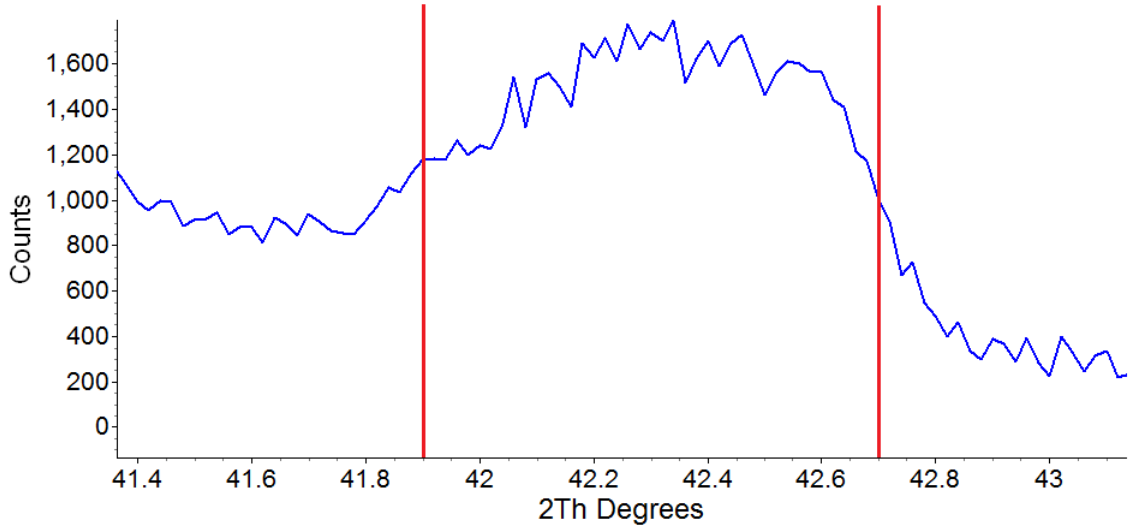


FIG. 5.16 – Part of the XRD pattern for sample X70-2 showing the first set of TiN-rich (111) peaks between $2\theta = 41.9°$ and $2\theta = 42.7°$.

In order to account for the multiple peaks, the procedure was adapted. Figure 5.17 presents the first step of that adapted procedure. Here, the set of TiN-rich (111) peaks spread out from $2\theta$ = 41.9° to $2\theta$ = 42.7°. In this example, the peak was deconvoluted into 9 different TiN-rich phases (referred as TiN 1, TiN 2, etc), in order to have one phase every 0.1°. These 9 phases have therefore 9 different lattice parameters that produce diffraction peaks evenly spread out from $2\theta$ = 41.9° to $2\theta$ = 42.7°. The phases are assumed to be pure nitrides to begin with. In Topas, the phases were initially added as $Ti_xNb_{1-x}N$ phases and initial parameters are presented in Table 5.7. TiN PDF file [58] gives a diffraction angle of $2\theta$ = 42.8° for the (111) plane. TiN lattice parameter is $a_{TiN}$ = 4.245 Å. A Co radiation is used for XRD analysis ($\lambda_{Co}$ = 1.78919 Å). The lattice parameters of the TiN-rich phases are calculated using Bragg's law and linear interpolation (using $\lambda_{Co}$, $a_{TiN}$ and $2\theta_{TiN}^{(111)}$). Ti contents are calculated using linear interpolation, i.e., x = 1 for $a_{TiN}$ = 4.245 Å and x = 0 for $a_{NbN}$ = 4.395 Å.

TABLE 5.7 – Initial parameters for Rietveld refinement for TiN-rich precipitates from X70-2 sample (values of Ti and Nb contents in atomic fraction).

| Phase | $2\theta$ (°) | a (Å) | Ti (x) | Nb (1-x) |
|---|---|---|---|---|
| TiN 1 | 42.7 | 4.258 | 0.91 | 0.09 |
| TiN 2 | 42.6 | 4.267 | 0.85 | 0.15 |
| TiN 3 | 42.5 | 4.277 | 0.78 | 0.22 |
| TiN 4 | 42.4 | 4.286 | 0.73 | 0.27 |
| TiN 5 | 42.3 | 4.296 | 0.66 | 0.34 |
| TiN 6 | 42.2 | 4.306 | 0.60 | 0.40 |
| TiN 7 | 42.1 | 4.316 | 0.53 | 0.47 |
| TiN 8 | 42 | 4.325 | 0.46 | 0.54 |
| TiN 9 | 41.9 | 4.335 | 0.40 | 0.60 |

The refined compositions of the phases are not detailed in this section. The purpose is to provide information on how the refinement was done. During the first step Topas only refines the scale factor of each individual phase. During the second step (Figure 5.18), Topas refines the lattice parameters and the scale factors, in order to optimize the peak positions.

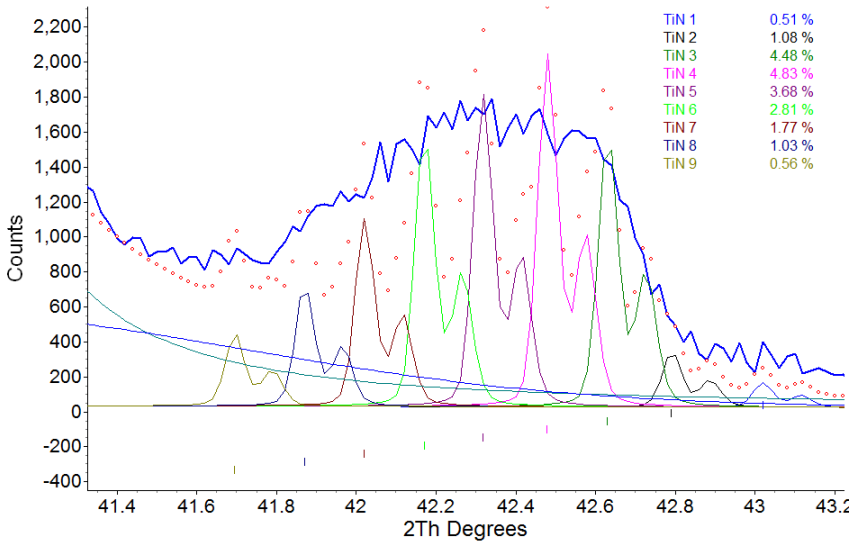


FIG. 5.17 – Step 1 of Rietveld refinement process showing addition of 9 TiN-rich phases evenly spread out between $2\theta = 41.9°$ and $2\theta = 42.7°$. The blue line represents the experimental XRD pattern. The red dots represent the calculated XRD pattern. The ticks below the curves represent the position of each diffraction peak.

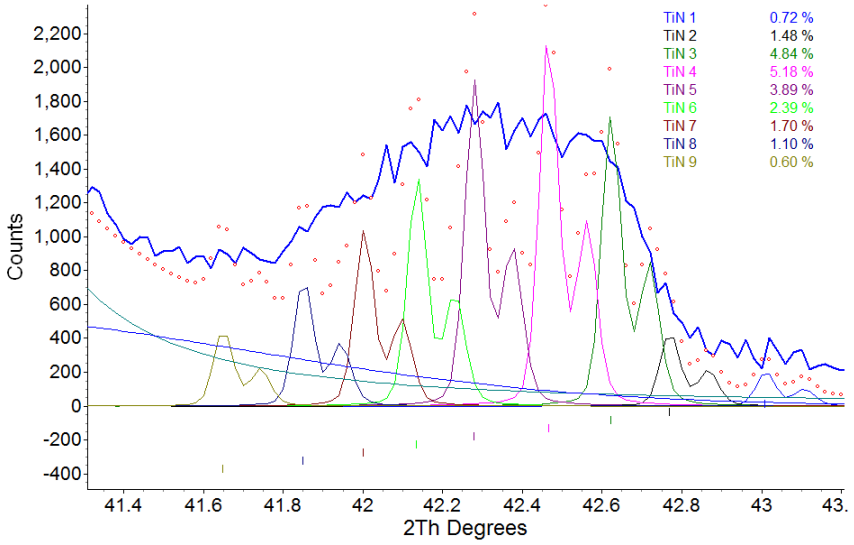


FIG. 5.18 – Step 2 of Rietveld refinement process showing refinement of the lattice parameters and scale factors for 9 phases.

The third step (Figure 5.19) is refinement of the size and strain parameters, so that the refinement of the shape of each peak improves the global fit. Finally, the composition of each phase

(Ti, Nb, C and N occupancies) are refined to fit the intensity of each peak (Figure 5.20).

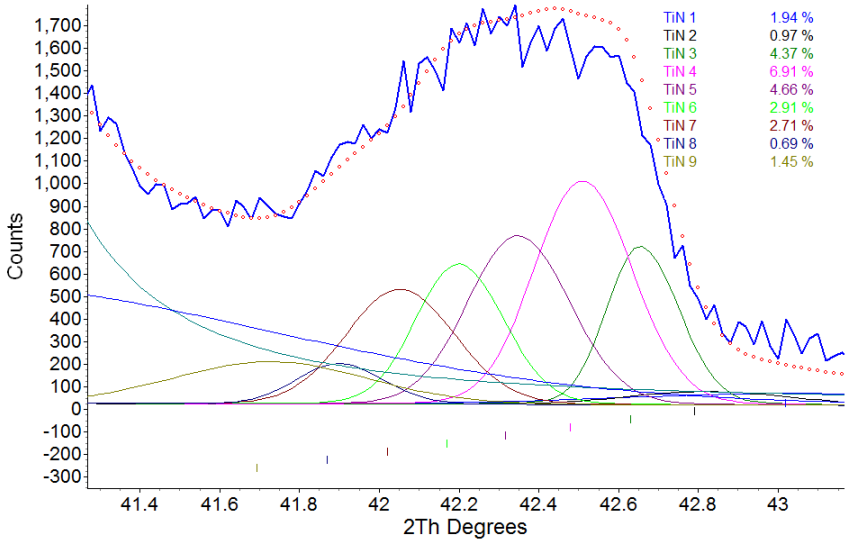


FIG. 5.19 – Step 3 of Rietveld refinement process showing refinement of the strain and size parameters for 9 phases.

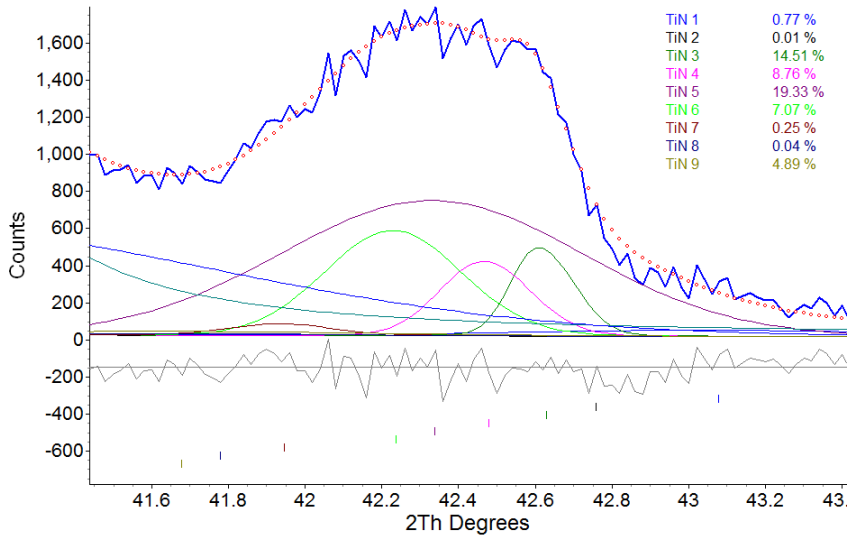


FIG. 5.20 – Step 4 of Rietveld refinement process showing refinement of the phase compositions for 9 phases.

Steps 2-4 have to be reiterated many times to improve the refinement. At the end of the refinement, when the fit is visually satisfying, the QXRD results are compared with the ICP

results to ensure the mass balance is closed. In this example, 4 out of the 9 phases that were initially introduced have a calculated wt% close to zero. This shows that the addition of 9 was too much. Only 5 TiN-rich phases would have been needed. Therefore only 5 phases are introduced for the subsequent analysis.

### 5.6.2 QXRD analysis for X70 steel

In this section, precipitates collected from the first X70 dissolution are analyzed. The sample is different from the one used in the previous section as an example for the adapted procedure. Figure 5.21 and Table 5.8 present refinement results for extracted precipitates from the X70 steel.

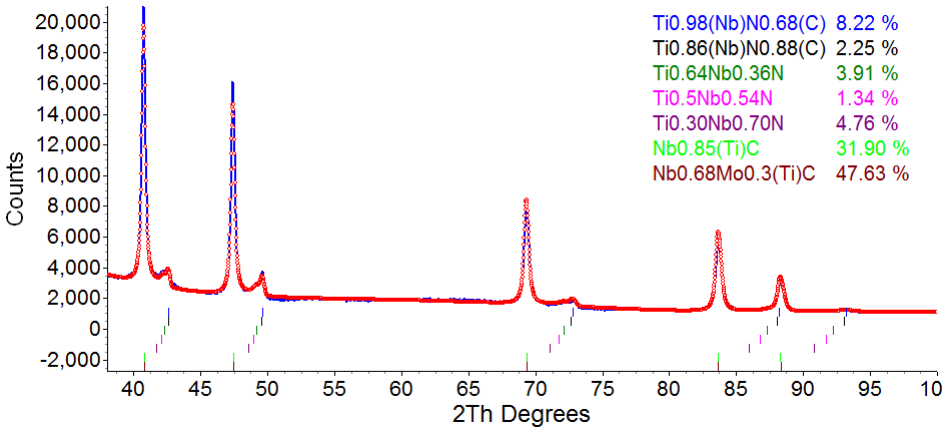


FIG. 5.21 – QXRD analysis for precipitates in X70 steel.

As detailed in Section 5.3, two types of precipitates are present, i.e., TiN-rich and NbC-rich. To fit the experimental pattern, 5 Ti(Nb,Mo,V)N(C) phases (as presented in the previous section) and 2 Nb(Ti,Mo,V)C(N) were needed. A single NbC-rich phase was not able to fit the experimental pattern. Therefore a second phase was added. V was added in the phases, however, no V was found in any phase during Topas refinement (occupancy refined to 0). Even if V was found in ICP (0.0004 wt%, 213 times lower than Nb), Topas refined the amount to 0. Mo was only found in the smallest precipitates. Table 5.8 shows 5 distinct compositions for the large precipitates. However, these have to be seen as average compositions. In reality, a range of compositions is observed (cf EDX analysis, Section 5.4.1).

TABLE 5.8 – QXRD results for precipitates in X70 steel.

| Precipitate | a (Å) | Strain (%) | $L_{vol}$ (nm) | $\bar{R}$ | wt% |
|---|---|---|---|---|---|
| $Ti_{0.97}Nb_{0.03}N_{0.68}C_{0.32}$ | 4.26 | 0.14 | 4000 | 1.5 µm | 8.2 |
| $Ti_{0.86}Nb_{0.14}N_{0.88}C_{0.12}$ | 4.27 | 0.19 | 4000 | 1.5 µm | 2.3 |
| $Ti_{0.64}Nb_{0.36}N$ | 4.30 | 0.19 | 4000 | 1.5 µm | 3.9 |
| $Ti_{0.50}Nb_{0.50}N$ | 4.32 | 0.28 | 4000 | 1.5 µm | 1.3 |
| $Ti_{0.30}Nb_{0.70}N$ | 4.35 | 0.82 | 4000 | 1.5 µm | 4.8 |
| $Nb_{0.85}Ti_{0.15}C$ | 4.45 | 0 | 40.3 | 15.6 nm | 31.9 |
| $Nb_{0.68}Mo_{0.30}Ti_{0.02}C$ | 4.45 | 0 | 10.9 | 4.2 nm | 47.6 |

In order to remain consistent, the lattice parameters provided by the refinement have to be physically consistent. A good way to assess is to look at the Ti concentration of each phase as a function of its lattice parameters. Figure 5.22 presents the Ti concentration of each phase as a function of its lattice parameters.

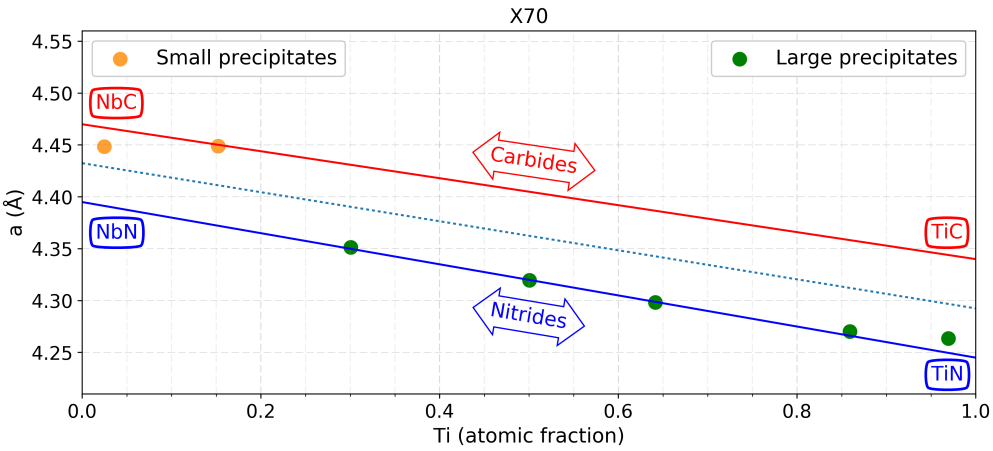


FIG. 5.22 – Lattice parameters for the precipitates as a function of Ti content for X70 steel.

The red line represents the 'carbides' line. On this line, precipitates should be pure carbides. The blue line represents the 'nitrides' line. On this line, precipitates should be pure nitrides. When the atomic fraction of Ti is close to 1, the red line represents for the TiC precipitates and the blue line for TiN precipitates. When the atomic fraction of Ti is close to 0, the red line

represents for the NbC precipitates and the blue line for NbN precipitates. It was noted that Topas refinement was not sensitive to C and N composition. The presented C and N contents allow for the best Rietveld refinement. A more precised analysis is required to validate these compositions. In order to remain physically acceptable, each phase (represented by a dot in Figure 5.22) has to be between or on the lines. The distance to the lines (if the marker is between the lines) represents the C/N content. Concerning the two first large precipitates, their representative dots are not on the 'nitrides' line, which is consistent with the fact that they are carbonitrides. The last three large precipitates are pure nitrides and their representative dots appear to be on the 'nitrides' line. The two small precipitates are pure carbides, but only the representative dot of the first one appears to be on the 'carbides' line. This may be due to the fact that Mo is accounted for as Nb for the second small precipitate. Nevertheless, the dot is closer to the 'carbides' line than to the 'nitrides' line.

The agreement between the composition and the lattice parameters is relatively good for the precipitates collected from X70 steel. The last thing to check is the mass balance, i.e., the comparison between the ICP results and the relative amount of each precipitate type calculated through Topas. Firstly, the molar mass of each phase is calculated from the calculated atomic compositions. Then the number of moles is deduced using the molar mass, the relative abundance of each phase and the mass of the collected residues. The total mass of each element (Ti, Nb, Mo, etc.) in precipitate form is calculated using the atomic mass of each element, the number of moles of each phase and the atomic composition of the phase. Finally the weight fraction (wt%) of each element in precipitate form is calculated using the mass of the steel sample and the amount of each element previously calculated. An example can be found in Appendix B.

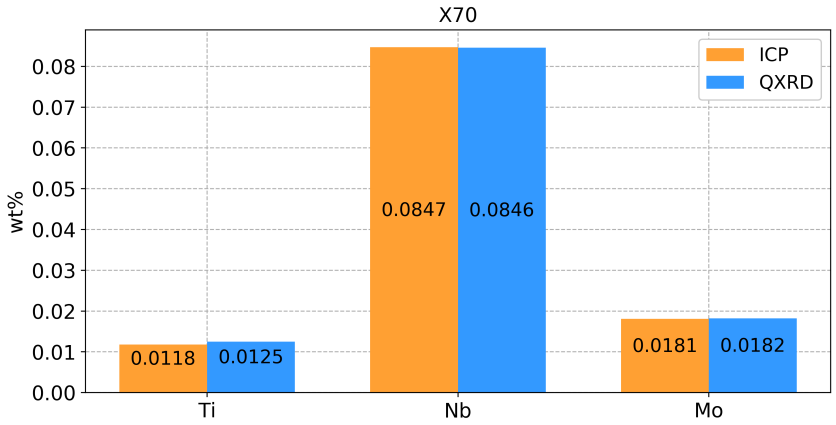


FIG. 5.23 – Comparison between ICP and QXRD results for precipitates in X70 steel.

From the error analysis introduced in Chapter 3, regarding the experimental procedures, it was shown that the relative weight fraction (of a particular phase) below 5% was not reliable. Figure 5.23 presents the comparison between the ICP and the QXRD results for Ti, Nb and Mo amount in precipitate form. A good agreement is found between the ICP and the QXRD results. The mass balance is closed for Ti, Nb and Mo.

The sizes of small precipitates calculated by Rietveld refinement (4.2 and 15.6 nm) are within the same order of magnitude as the one measured by SEM (7.95 nm). The number of analyzed particles (during SEM analysis) may be too low for the size distribution to show two distinct peaks.

### 5.6.3 QXRD analysis for TWX70 steel

The refinement results obtained with Topas for the TWX70 precipitates are shown in Figure 5.24, following the same procedure as explained for the X70 steel. The second peak (002) for the TiN-rich precipitates (around $2\theta = 49°$) is not well fit. The explanation is not clear at this time. The measured intensity is too high compared with the PDF file (Powder Diffraction File) available in the literature [58]. This anomaly appears to be linked to a preferred orientation.

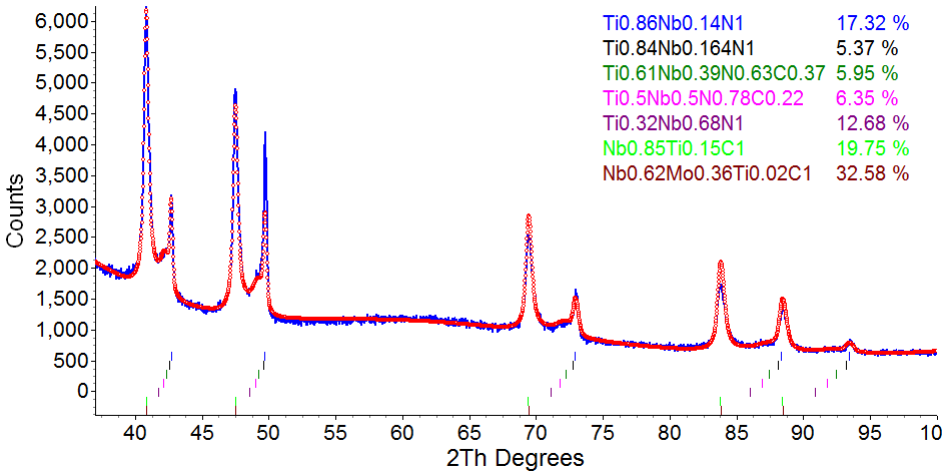


FIG. 5.24 – QXRD analysis for the precipitates in TWX70 steel.

However, there is no reason to expect a preferred orientation. One possible explanation is the way the sample was prepared for the XRD analysis. The powder was grind and deposited on the sample holder from an ethanol suspension. This preparation may likely have induced preferred orientation. No other explanation was found on why a preferred orientation would appear. This is a recurrent issue as shown in Chapter 6. The only way to account for this issue is to ignore these particular peaks during the refinement and not to try to fit the theoretical intensity to the experimental intensity. Ignoring this peak will not introduce error in the Rietveld refinement since the other peaks are refined. However, the refinement would provide less accurate results.

Table 5.9 presents the refinement results obtained with Topas. Both X70 and TWX70 are X70 steels with a similar composition. Therefore, as with the QXRD analysis for precipitates in X70, 5 Ti(Nb,Mo,V,Cr)N(C) phases (as presented in the Section 5.3) and 2 Nb(Ti,Mo,V,Cr)C(N) were needed. A single NbC-rich phase was not able to fit the experimental pattern. Therefore a second phase was added. No V or Cr were found in any phase during Topas refinement (occupancy refined to 0). Mo was only found in the smallest precipitates.

The comparison between the lattice parameters and the Ti composition is showed in Figure 5.25. Mo is accounted for as Nb for the purpose of the graph. The agreement is less good than

TABLE 5.9 – QXRD results for precipitates in TWX70 steel.

| Precipitate | a (Å) | Strain (%) | $L_{vol}$ (nm) | $\bar{R}$ | wt% |
|---|---|---|---|---|---|
| $Ti_{0.86}Nb_{0.14}N$ | 4.26 | 0.10 | 4000 | 1.5 µm | 17.3 |
| $Ti_{0.84}Nb_{0.16}N$ | 4.27 | 0.23 | 4000 | 1.5 µm | 5.4 |
| $Ti_{0.61}Nb_{0.39}N_{0.63}C_{0.37}$ | 4.29 | 0.25 | 4000 | 1.5 µm | 5.9 |
| $Ti_{0.50}Nb_{0.50}N_{0.78}C_{0.22}$ | 4.32 | 0.27 | 4000 | 1.5 µm | 6.4 |
| $Ti_{0.32}Nb_{0.68}N$ | 4.35 | 0.99 | 4000 | 1.5 µm | 12.7 |
| $Nb_{0.84}Ti_{0.16}C$ | 4.44 | 0 | 28.9 | 11.2 nm | 19.8 |
| $Nb_{0.62}Mo_{0.36}Ti_{0.02}C$ | 4.44 | 0 | 13.21 | 5.1 nm | 32.6 |

for the precipitates in X70 steel. Nevertheless, the large precipitates (nitrides and carbonitrides) have their representative dots close to the 'nitrides' line. The pure carbide small precipitates are also close to the 'carbides' line. The purpose of this figure is to check if the lattice parameters are within the range of compositions that are allowed based on linear interpolations. As mentionned previously for X70 steel in Section 5.6.2, it was noted that Topas refinement was not sensitive to C and N composition. The presented C and N contents allow for the best Rietveld refinement. A more precised analysis such as TEM-EDX analysis is required to validate these compositions. For precipitates extracted from TWX70 steel, the agreement is overall decent.

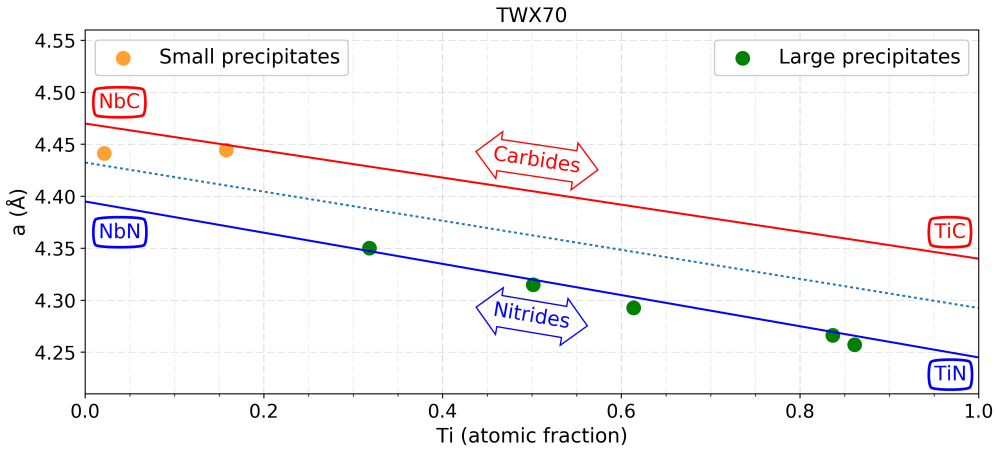


FIG. 5.25 – Lattice parameters for the precipitates as a function of Ti contents for TWX70 steel.

Figure 5.26 shows the comparison between the ICP results and the amount of Ti, Nb and Mo in the precipitates calculated through Topas. The agreement is less good than the one for X70 steel. Neverthess, the mass balance is closed for Ti, Nb and Mo. The same calculations as for precipitates in X70 steel were done.

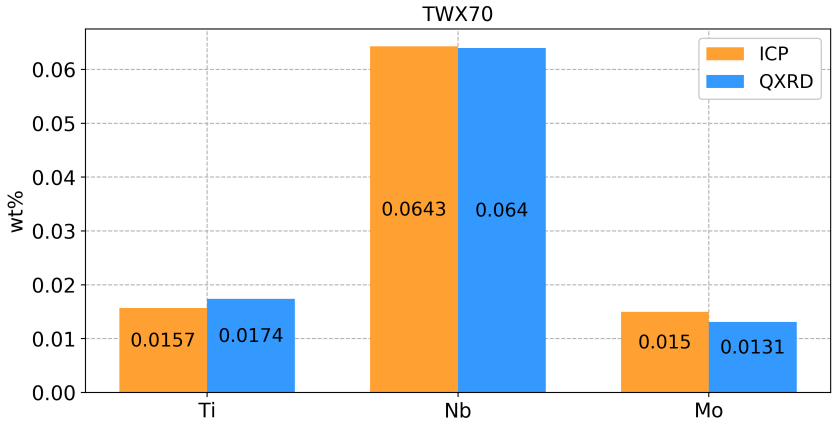


FIG. 5.26 – Comparison between ICP and QXRD results for precipitates in TWX70 steel.

The sizes of small precipitates calculated by Rietveld refinement (5.1 and 11.2 nm) are of the same order of magnitude as the one measured by SEM (4.4 and 10 nm). In this case, the particle size distribution displayed two peaks.

## 5.7 Summary

The QXRD results are consistent with the ICP analysis and the mass balance is closed for Ti, Nb and Mo for both steels. EDX analysis confirms that large precipitates have ranges of compositions. The agreement between the EDX and QXRD results is less good for the small precipitates. Nevertheless, the QXRD results are supported by the ICP analysis and the comparison between the lattice parameters against the Ti contents. SEM analysis confirms the order of magnitudes for the size distribution of the large and small precipitates for both steels. The results are discussed and compared with the numerical simulations in Chapter 7.

# Chapter 6

# L80, ML80 and T95 steels

Chapter 5 presented the precipitation analysis of two different X70 steels. This chapter provides the same kind of information regarding three different heat-treated steels: L80, ML80 and T95. As shown in Table 3.1 (Chapter 3), the main differences between those steels are their compositions. L80 steel is a standard Ti/B heat-treated product. ML80 is a Mo-rich L80, while T95 has a high Cr content and slightly different heat treatment conditions. The exact heat treatment conditions can be found in Chapter 3. The same experimental procedures used for the X70 steels were used to analyze the precipitates in the L80, ML80 and T95 steels including SEM-EBSD, SEM-EDX, ICP of the supernatant solution, XRD and QXRD of the extracted powders and SEM-EDX of the precipitates. The main objective is to determine the effect of the Mo and Cr content on precipitation.

## 6.1 Microstructural analysis and grain size measurements

Quarter thickness samples for the three steels were analyzed to determine their microstructures and their grain sizes (through a mean linear intercept method).

### 6.1.1 SEM analysis

Figure 6.1 presents inverted SEM SE images of a L80 sample taken at (A) low and (B) high magnification. In both images, the microstructures appear to be tempered martensite and bainite

given the thermal history of the steel (austenized at 900°C and then quenched and tempered at 680°C for 3 h). The same type of microstructure is observed for the ML80 steel (Figure 6.2 (A) and (B)) and the T95 steel (Figure 6.3 (A) and (B)) samples.

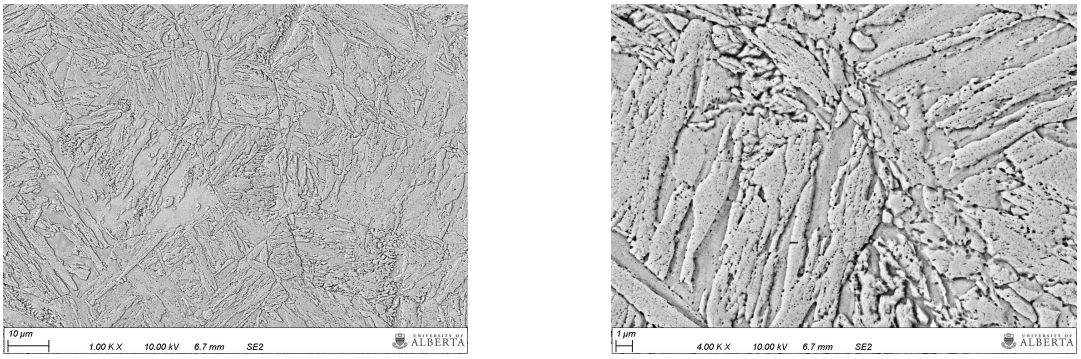


(A) (B)

FIG. 6.1 – SEM SE images of L80 steel: (A) lower and (B) higher magnification.

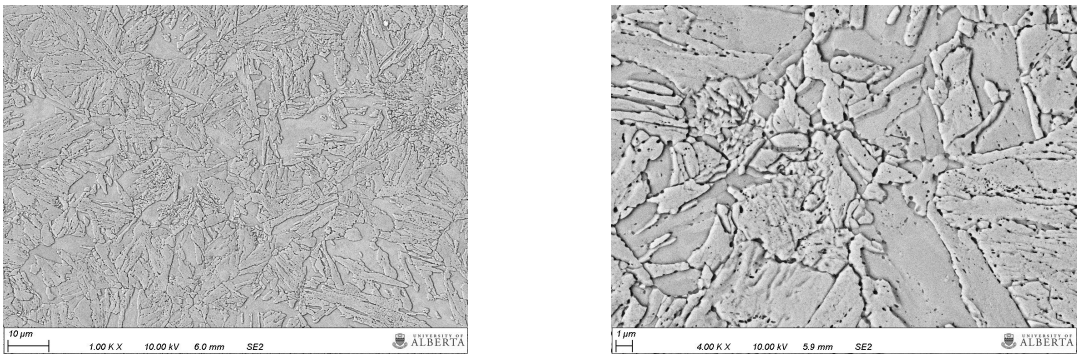


(A) (B)

FIG. 6.2 – SEM SE images of ML80 steel: (A) lower and (B) higher magnification.

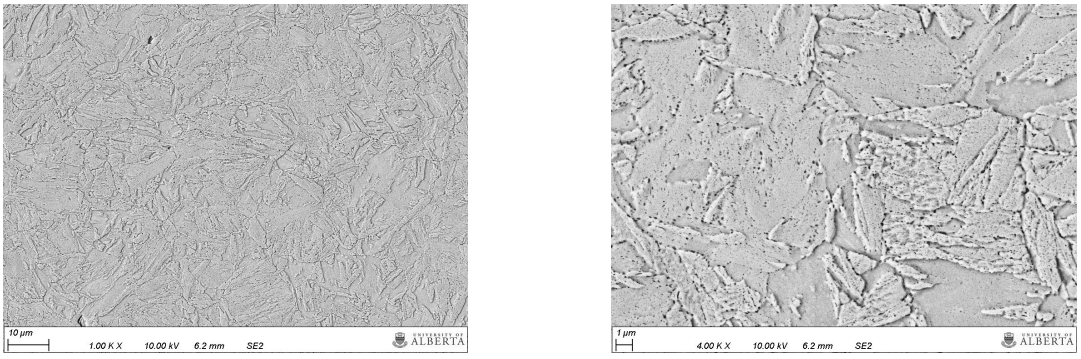


(A) (B)

FIG. 6.3 – SEM SE images of T95 steel: (A) lower and (B) higher magnification.

Some precipitates are observed through SE SEM imaging. However, it was not possible to determine their composition by EDX analysis because of the ferritic matrix surrounding the particles. Only Fe was picked up during EDX analysis.

### 6.1.2 EBSD analysis

Figure 6.4 shows three EBSD images for (A) L80, (B) ML80 and (C) T95 steel. A stepsize of 200 nm was used for L80, 150 nm for T95 and 400 nm for ML80. The grain boundaries are set as having a misorientation greater than 15 degrees.

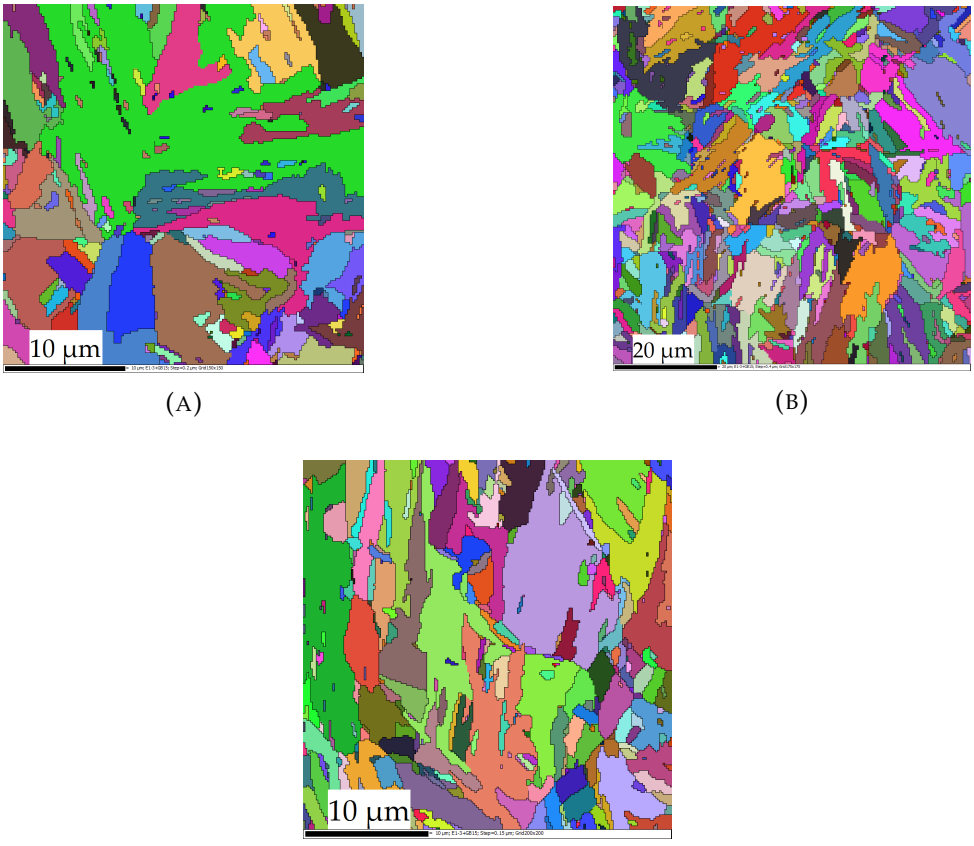


(A) (B)

(C)

FIG. 6.4 – EBSD images for (A) L80, (B) ML80 and (C) T95 steels.

SE SEM imaging and EBSD analysis provide qualitative information about the structure and the size of the grains. The mean linear intercept method was used to provide quantitative analysis.

### 6.1.3 Mean linear intercept (m.l.i.) measurements

The m.l.i. measurements (mean value, median and standard deviation $\sigma$) for the three steels, using SEM and EBSD images are presented in Table 6.1 and Figure 6.5. The SEM and EBSD measurements are consistent for all the steels. Both analyses show the steels have about the same mean linear intercept. The standard deviations $\sigma$ are large because of the large range of grain sizes (see Figure 6.3).

TABLE 6.1 – Mean linear intercept results for L80, ML80 and T95 steels.

| m.l.i. SEM-SE | L80 | ML80 | T95 |
|---|---|---|---|
| Mean (µm) | 2.8 | 2.6 | 2.5 |
| Median (µm) | 2.2 | 2.0 | 1.8 |
| $\sigma$ (µm) | 2.1 | 2.0 | 2.2 |

| m.l.i. EBSD | L80 | ML80 | T95 |
|---|---|---|---|
| Mean (µm) | 2.7 | 2.4 | 2.3 |
| Median (µm) | 2.0 | 1.6 | 1.8 |
| $\sigma$ (µm) | 2.1 | 1.9 | 1.9 |

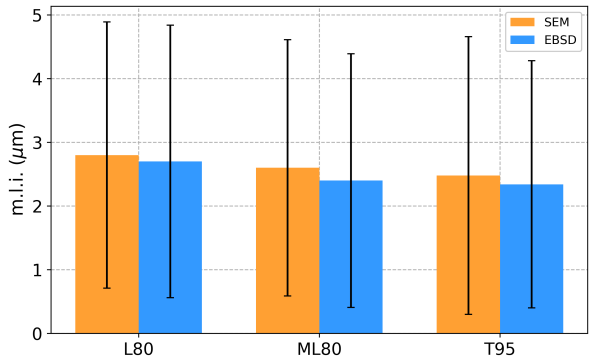


FIG. 6.5 – Mean linear intercept measurements for L80, ML80 and T95 steels.

## 6.2 Chemical dissolution of steel matrix

The same experimental procedure that was used for the X70 steels was followed, leading to no amorphous $SiO_2$ production. Table 3.3 (in Chapter 3) displays the dissolution results. The dissolution of the ML80 steel and T95 steel show a similar yield ($m_{residues}/m_{steel}$), i.e., 0.11% for the ML80 and 0.10% for the T95 steel. The dissolution of the L80 steel has a much lower yield (0.01%).

## 6.3 ICP measurements

Dissolution provided two samples to analyze: the extracted precipitates and the supernatant solution. ICP analysis was done on the latter in order to estimate the amount of the various alloying elements that remains in solution. Knowing the amount of each element in steel, and measuring the amount that remains in solution, a simple subtraction provides the amount that is present in precipitate form.

### 6.3.1 L80 steel

The ICP results for L80 dissolution are presented in Figure 6.6 and Table 6.2. Most of the Ti (78.8%) and Mo (89.9%) is present in solution after dissolution. All the V is also present in solution after dissolution. In addition, no Cr is present in precipitate form.

TABLE 6.2 – ICP measurements and calculated amounts in precipitate form for L80 steel.

| Analyte | Steel (wt%) | Solution (wt%, measured) | Equilibrium (wt%) | In precipitate (wt%, calculated) |
|---|---|---|---|---|
| Ti | 0.03 | 0.024 | $2.4 \cdot 10^{-4}$ | 0.006 |
| Cr | 0.14 | 0.147 | 0.025 | -0.007 |
| Mo | 0.019 | 0.017 | $4 \cdot 10^{-6}$ | 0.02 |
| V | 0.003 | 0.0031 | 19.23 | -0.0001 |

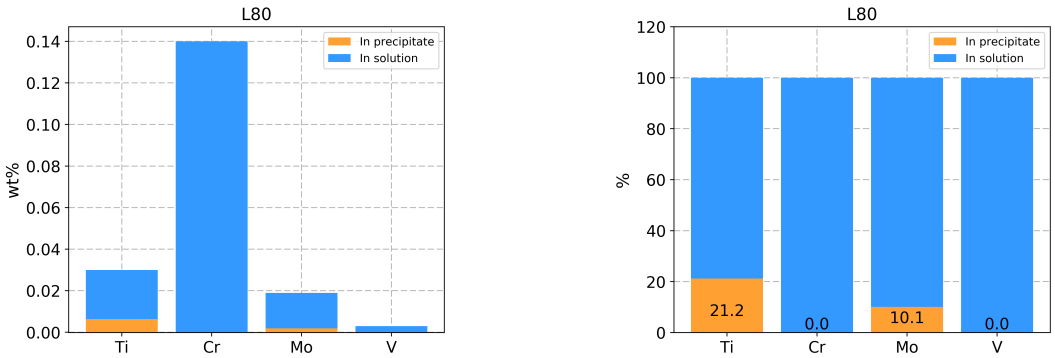


(A) (B)

FIG. 6.6 – ICP results for L80 steel: (A) composition in wt% and (B) relative amounts.

The measured amount of Cr (and V) is even higher than the steel composition. This could be due to the precision of the measurement or to an actual higher concentration in the dissolved piece. This is an important information for the subsequent QXRD analysis. It can be postulated that the precipitates will be mainly of the form (Ti,Mo)(C,N).

### 6.3.2 ML80 steel

ICP results for ML80 dissolution are presented in Figure 6.7 and Table 6.3. Most of the Cr (93.9%) and Mo (79.2%) are present in solution after dissolution. All the V is also present in solution after dissolution. Even though the amount of Ti is very low in the steel, most of it is present in precipitate form (85%). However, the amount of Ti in precipitates is much lower than the amount of Mo and Cr in precipitates. It can be postulated that the precipitates are mainly of the form (Mo,Cr)(C,N).

TABLE 6.3 – ICP measurements and calculated amounts in precipitate form for ML80 steel.

| Analyte | Steel (wt%) | Solution (wt%, measured) | Equilibrium (wt%) | In precipitate (wt%, calculated) |
|---|---|---|---|---|
| Ti | 0.001 | 0.0001 | $2.4 \cdot 10^{-4}$ | 0.0009 |
| Cr | 0.22 | 0.207 | 0.025 | 0.013 |
| Mo | 0.436 | 0.345 | $4 \cdot 10^{-6}$ | 0.091 |
| V | 0.001 | 0.002 | 19.23 | -0.001 |

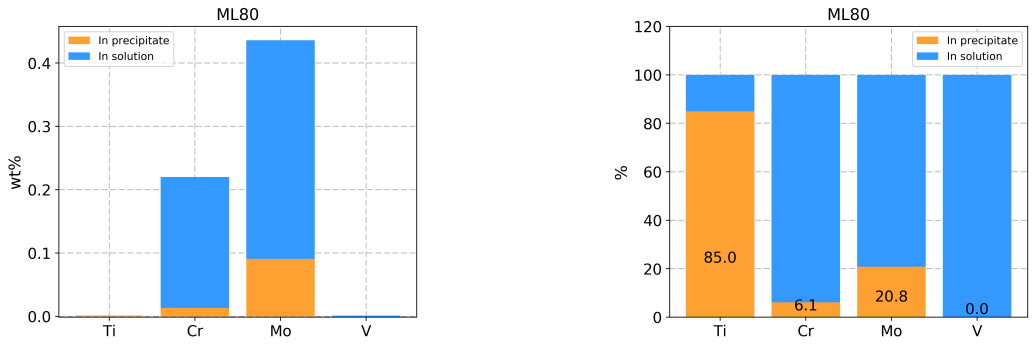


(A) (B)

FIG. 6.7 – ICP results for ML80 steel: (A) composition in wt% and (B) relative amounts.

### 6.3.3 T95 steel

ICP results for T95 dissolution are presented in Figure 6.8 and Table 6.4. Most of the Mo (87.4%) is present in solution after dissolution and all the Cr is present in solution after dissolution. All the V is also present in solution after dissolution. The measured amount of Cr (and V) is even higher than the steel composition. This could be due to the precision of the measurement or to an actual higher concentration in the dissolved piece. Almost all the Ti (98.1%) is present in precipitate form. It can be postulated that the precipitates will be of the form (Ti,Mo)(C,N).

TABLE 6.4 – ICP measurements and calculated amounts in precipitate form for T95 steel.

| Analyte | Steel (wt%) | Solution (wt%, measured) | Equilibrium (wt%) | Precipitate (wt%, calculated) |
|---|---|---|---|---|
| Ti | 0.041 | 0.001 | $2.4 \cdot 10^{-4}$ | 0.040 |
| Cr | 0.9 | 0.97 | 0.025 | -0.07 |
| Mo | 0.193 | 0.169 | $4 \cdot 10^{-6}$ | 0.024 |
| V | 0.006 | 0.0068 | 19.23 | -0.0008 |

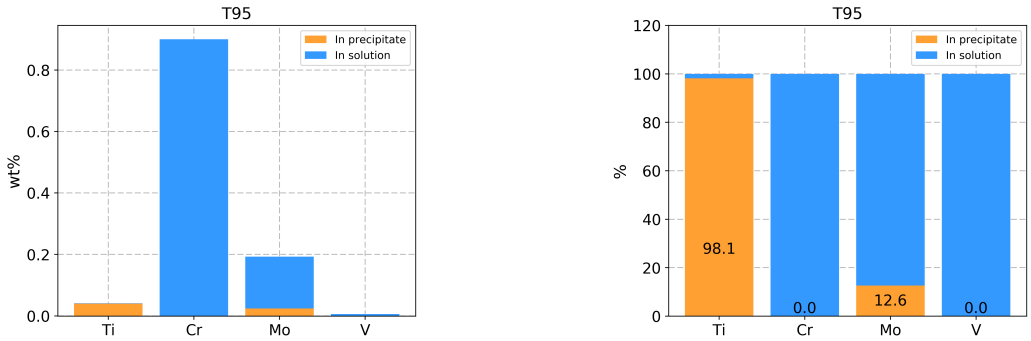


(A) (B)

FIG. 6.8 – ICP results for T95 steel: (A) composition in wt% and (B) relative amounts.

Even if C and Cr contents are higher in T95 steel, no Cr was found using ICP analysis. It is possible that other precipitates such as (Fe,Mo,Cr)C precipitates may have been present in the steel (particle observed by SEM, Figure 6.3) and have dissolved during matrix dissolution. This will be further developed in Chapter 7, Section 7.4.

### 6.3.4 Summary of ICP analysis

ICP analysis shows that the precipitates are mainly (Ti,Mo)(C,N) for the L80 and T95 steels and (Mo,Cr)(C,N) for the ML80 steel. Most of the Cr appears to remain in acidic solution after dissolution. The collected precipitates can be characterized more precisely through Quantitative XRD (QXRD) analysis and SEM-EDX analysis.

## 6.4 SEM-EDX analysis of the extracted precipitates

SEM-EDX analysis can provide both qualitative and quantitative information regarding the precipitates. Following the same procedure as for the X70 steels, two kinds of samples were prepared. The first type of sample (powder deposition) allows for determination of the atomic composition (using EDX analysis) and the sizes and shapes of the large precipitates. The second type of sample (suspension deposition) provides a way to examine the size distribution of the small precipitates.

### 6.4.1 L80 steel

Figure 6.9 shows two in-lens SEM SE images of (A) L80 powder and (B) L80 suspension samples. Figure 6.9(A) shows a TiN-rich precipitate surrounded by agglomerates of smaller precipitates. Some oxides (large spherical particles) can also be seen. Figure 6.9(B) shows nanoprecipitates.

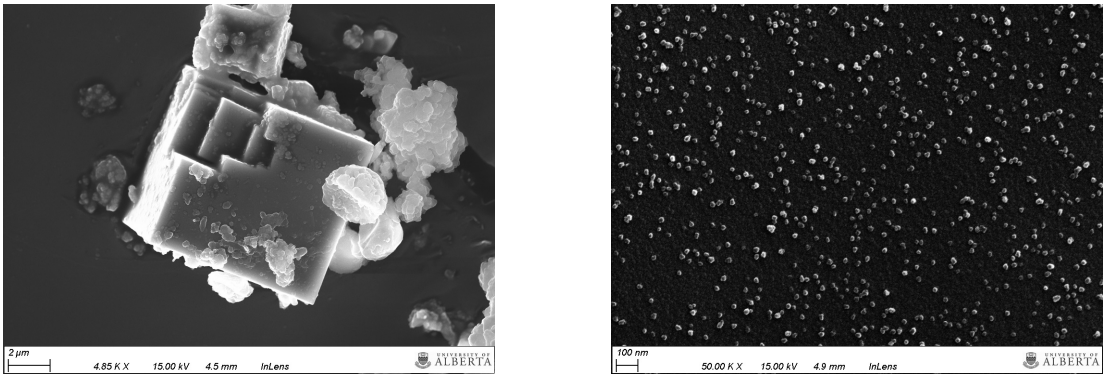


(A) (B)

FIG. 6.9 – SEM SE images of collected precipitates from L80 steel: (A) large TiN particle and (B) nanosize precipitates.

Ten images of the suspension deposition were analyzed. The particles appears to be spherical. The size distribution of the nano-precipitates (Figure 6.10) shows two peaks at 4.4 and 13.8 nm. It is possible that the second peak (13.8 nm) represents small agglomerates (2 or 3 individual precipitates). However, the resolution of the SEM does not allow for confirmation of that hypothesis.

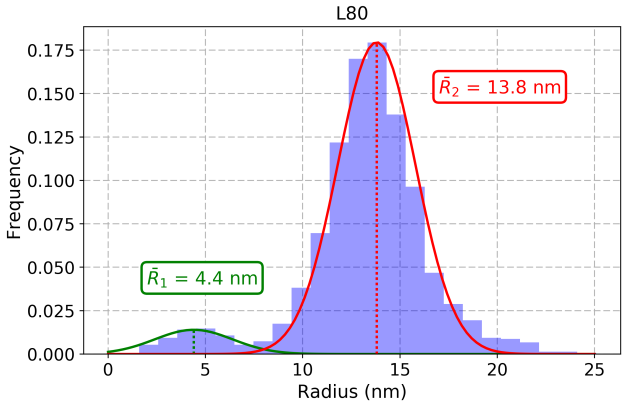


FIG. 6.10 – L80 steel precipitate size (particle radii) distribution from a total of 1526 particles.

Figure 6.11 and Table 6.5 present EDX results for collected precipitates from L80 steel. The large precipitates were characterized as almost pure Ti (0.997 in average) precipitates (25 precipitates analyzed). 18 agglomerates of nanoscale precipitates were analyzed and a range of Mo composition was observed with an average value of 0.1 Mo in the precipitates. Almost no Cr (0.004 in average) was observed by EDX analysis. This confirms the ICP analysis (Figure 6.6) where no Cr was calculated in precipitate form. The low amount measured by EDX analysis might be an artefact (noise background). The precipitates are mainly Ti/Mo-rich precipitates.

TABLE 6.5 – EDX analysis of large precipitates (total of 25 particles) and small precipitates (total of 18 agglomerates) for L80 steel (values in atomic fraction).

| Small | Ti | Mo | Cr |
|---|---|---|---|
| Average | 0.900 | 0.095 | 0.004 |
| StDev | 0.042 | 0.042 | 0.004 |

| Large | Ti | Mo | Cr |
|---|---|---|---|
| Average | 0.997 | 0.002 | 0.001 |
| StDev | 0.003 | 0.003 | 0.001 |

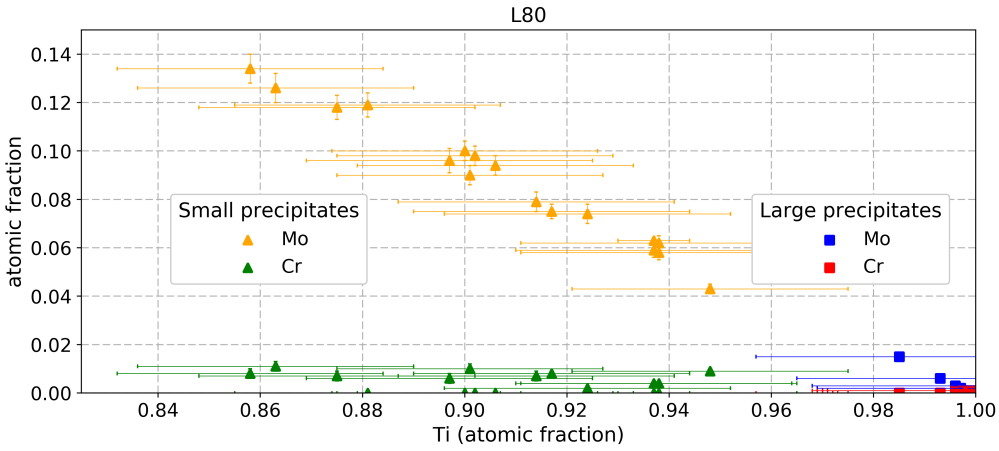


FIG. 6.11 – EDX analysis for precipitates extracted from L80 steel. The Cr content of the large precipitates is shown in red and the Mo content is shown in blue. The Cr content of the small precipitates is shown in green and the Mo content is shown in yellow.

### 6.4.2 ML80 steel

Figure 6.12 presents two in-lens SEM SE images for extracted precipitates from ML80 steel. Figure 6.12(A) shows an agglomerate of small precipitates. Figure 6.12(B) shows a suspension deposition where the particles appears to be spherical.

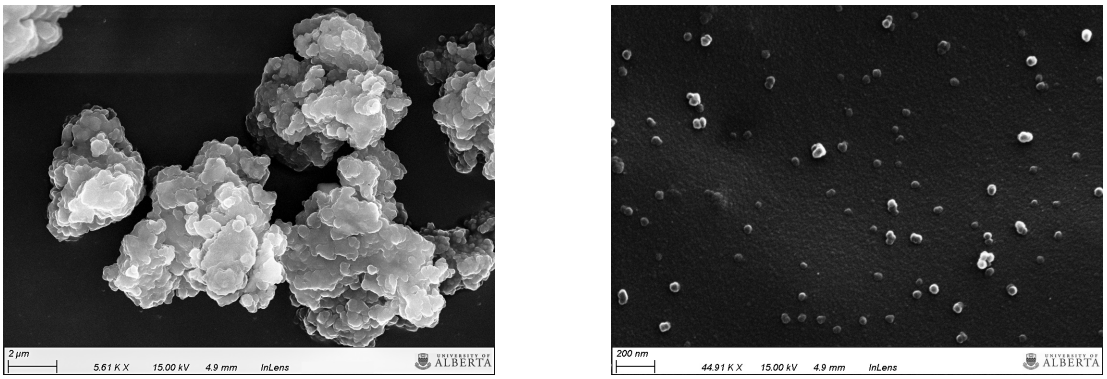


(A) (B)

FIG. 6.12 – SEM SE images for collected precipitates from ML80 steel: (A) Agglomerates and (B) suspension sample.

Fourteen images of the suspension deposition were analyzed and 1841 precipitates were measured. Two peaks are observed in the size distribution in Figure 6.13, a peak at around 8.6

nm and a second peak at around 31.4 nm. The second peak (31.4 nm) may represent particles that are small agglomerates (2 or 3 individual precipitates).

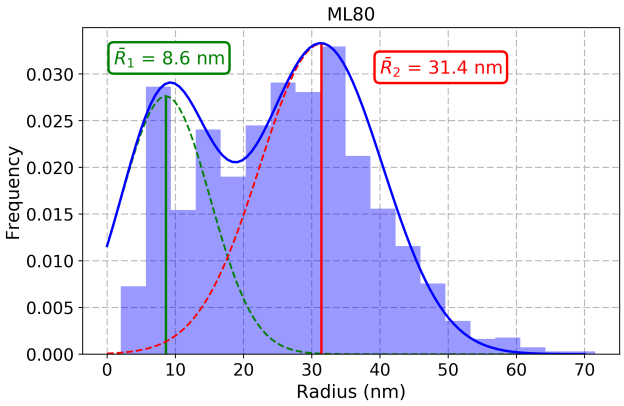


FIG. 6.13 – ML80 steel precipitate size (particle radii) distribution from a total of 1841 particles. The blue curve is the sum of the green and red distributions.

Eighteen agglomerates of nanoscale precipitates were studied by EDX analysis. Figure 6.14 and Table 6.6 present the EDX results. Only a small range of compositions was observed over the 18 measurements. The average Mo atom fraction is 0.96 while the average Cr atom fraction is 0.028. Precipitates are mainly Mo/Cr-rich precipitates. This confirms the ICP analysis (Figure 6.7). Some Al is also seen by EDX analysis. However, this could due to contamination from residues collection or sample preparation.

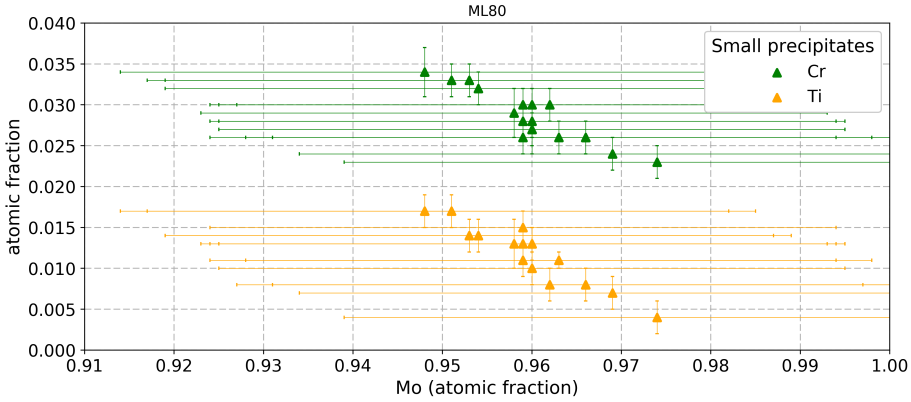


FIG. 6.14 – EDX analysis for precipitates extracted from ML80 steel. The Cr content of the small precipitates is shown in green and the Ti content is shown in yellow.

TABLE 6.6 – EDX analysis for small precipitates (total of 18 agglomerates) from ML80 steel (values in atomic fraction).

| Small | Ti | Mo | Cr |
|---|---|---|---|
| Average | 0.011 | 0.960 | 0.028 |
| StDev | 0.004 | 0.006 | 0.003 |

### 6.4.3 T95 steel

Figure 6.15 presents two in-lens SEM SE images of the collected precipitates from T95 steel. Figure 6.15(A) shows a TiN-rich precipitate with smaller precipitates on its surface. Figure 6.15(B) shows a suspension deposition sample.

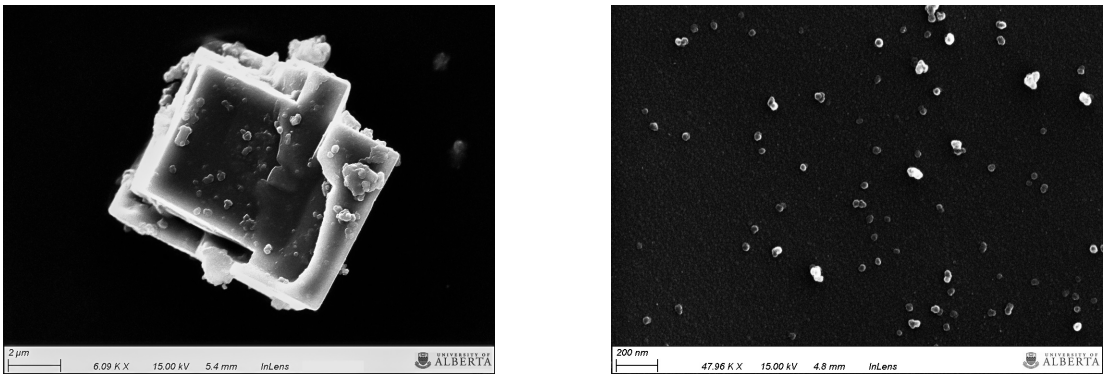


(A) (B)

FIG. 6.15 – SEM SE images of collected precipitates from T95 steel: (A) TiN and (B) suspension sample.

Nine images of the suspension deposition were analyzed. The particles appeared to be spherical. The size distribution in Figure 6.16 shows a first peak at around 5.2 nm and a second peak at around 34.8 nm. A total of 1414 precipitates were measured. It is still possible that the precipitates observed through SEM (5.2 and 34.8 nm) are small agglomerates of smaller particles.

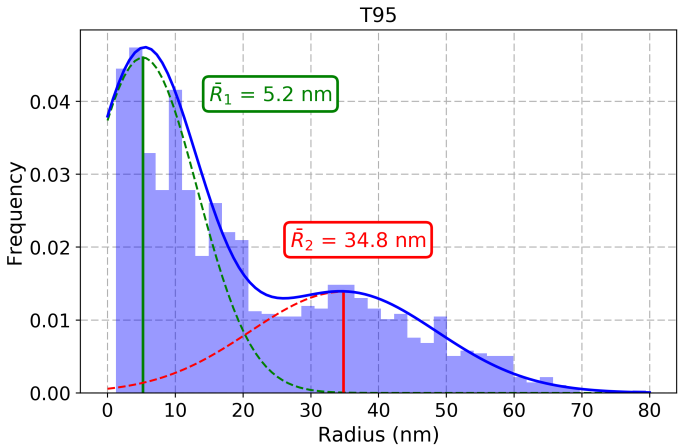


FIG. 6.16 – T95 steel precipitate size (particle radii) distribution from a total of 1414 particles. The blue curve is the sum of the green and red distributions.

Figure 6.17, Table 6.7 and Table 6.8 present the EDX results of the collected precipitates from T95 steel. The Mo content varies between 0.1 and 0.3 (atomic fraction), while the Cr content is constant below 0.03 (atomic fraction). Two ranges of large precipitates are present (Table 6.8). The first one represents almost pure Ti-rich precipitates. The Mo and Cr contents are below 0.01 (atomic fraction). The second type of large precipitates has an average Mo content of 0.04. These results confirm that almost no Cr (0.02) is present in precipitate form (Figure 6.8). Mo appears to be a major constituent of the nanoscale precipitates.

TABLE 6.7 – EDX analysis for the small precipitates (total of 40 agglomerates) from T95 steel (values in atomic fraction).

| Small | Ti | Mo | Cr |
|---|---|---|---|
| Average | 0.775 | 0.204 | 0.021 |
| StDev | 0.041 | 0.038 | 0.004 |

TABLE 6.8 – EDX analysis for T95 large precipitates (total of 34 particles). Values in atomic fraction.

| Large | Ti | Mo | Cr |
|---|---|---|---|
| Average | 0.986 | 0.009 | 0.005 |
| StDev | 0.007 | 0.005 | 0.004 |

| Large | Ti | Mo | Cr |
|---|---|---|---|
| Average | 0.947 | 0.041 | 0.011 |
| StDev | 0.019 | 0.020 | 0.007 |

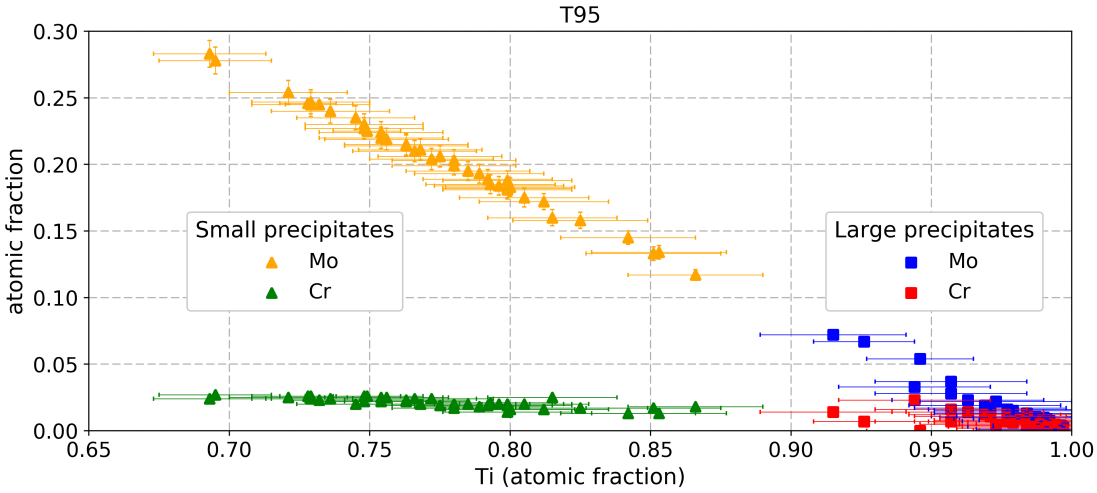


FIG. 6.17 – EDX analysis for precipitates extracted from T95 steel. The Cr content of the large precipitates is shown in red and the Mo content is shown in blue. The Cr content of the small precipitates is shown in green and the Mo content is shown in yellow.

## 6.5 X-ray diffraction of the extracted precipitates

Based on the ICP analysis, the collected powders are composed of complex (Ti,Mo,Cr)-rich precipitates. Based on EDX analysis, large precipitates are Ti-rich and Ti/Mo-rich precipitates for L80 and T95 steels. Small precipitates appears to be Mo-rich for ML80 steel and Ti/Mo-rich for L80 and T95 steels. XRD provides information regarding the lattice parameters (which depends on the peak positions), the atomic composition (through the peak intensities) and the size and strain of the crystallites (through the shape of the peaks).

### 6.5.1 L80 steel

Figure 6.18 shows the XRD pattern obtained for extracted precipitates from L80 steel. The XRD analysis was done using the XRD Jade software. The pattern shows four different phases. Two phases are consistent with a TiN-rich, based on the peak positions, cubic structure ($Fm\bar{3}m$ space group) and two others are consistent with an $Fd\bar{3}m$ structure. These latter two phases are believed to be oxides ($As_2O_3$ and $CuAl_2O_4$, according to Jade analysis) present in the steel or

formed during the dissolution (contamination). As, Cu and Al could be found in the steel composition in residual amounts according to EVRAZ (2200 ppm for Cu and 530 ppm for Al). As content is not provided by EVRAZ. Therefore the formation of such oxides is possible during the steel dissolution in HCl.

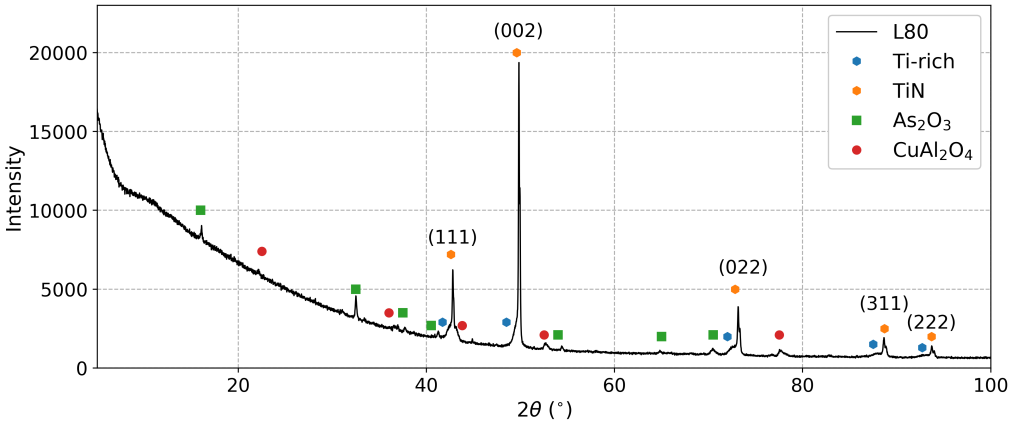


FIG. 6.18 – XRD pattern for collected precipitates from L80 steel.

EDX analysis shows the presence of As, Mg, Al and O (see Appendix C for EDX spectra). As and Mg peaks are very close in EDX spectra; therefore, it is difficult to deconvolute them. However, because the XRD pattern matches with As oxide and not Mg oxide, it is reasonable to assume As is present in the collected residues. In order to be certain, it would be of interest to do EDX analysis at higher energies (between 10 and 15 keV). The EDX analysis presented in this work did not allow for the analysis of energies higher than 10 keV because of the maximum accelerated voltage of 20 kV . No Cu was observed during EDX analysis though. It was difficult to analyze oxide particles because of their low amount.

### 6.5.2 ML80 steel

Figure 6.19 shows the XRD pattern obtained for extracted precipitates from ML80 steel. The pattern shows only one phase consistent with a hexagonal structure (P63/mmc space group) characteristic of a $Mo_2C$-rich phase according to Jade analysis.

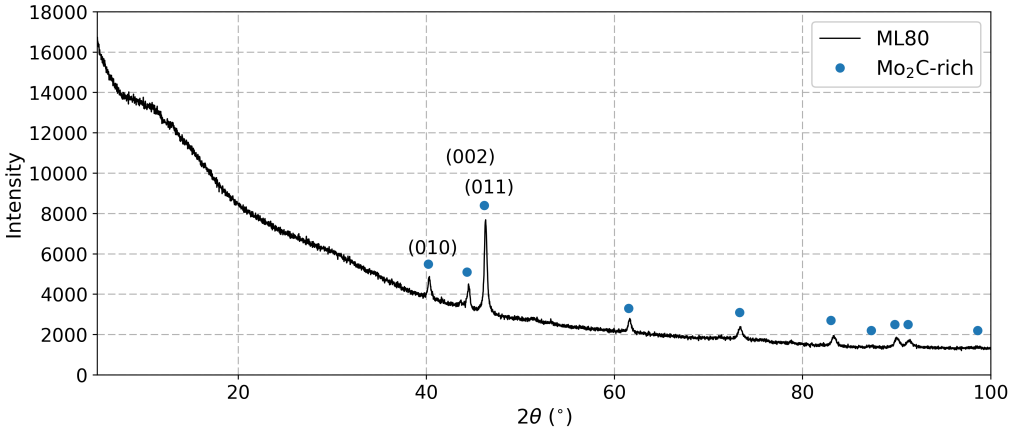


FIG. 6.19 – XRD pattern for collected precipitates from ML80 steel.

### 6.5.3 T95 steel

Figure 6.20 shows the XRD pattern obtained for extracted precipitates from T95 steel. The pattern shows three different phases, all consistent with a TiN-rich cubic structure ($Fm\bar{3}m$ space group) based on the peak positions and Jade analysis.

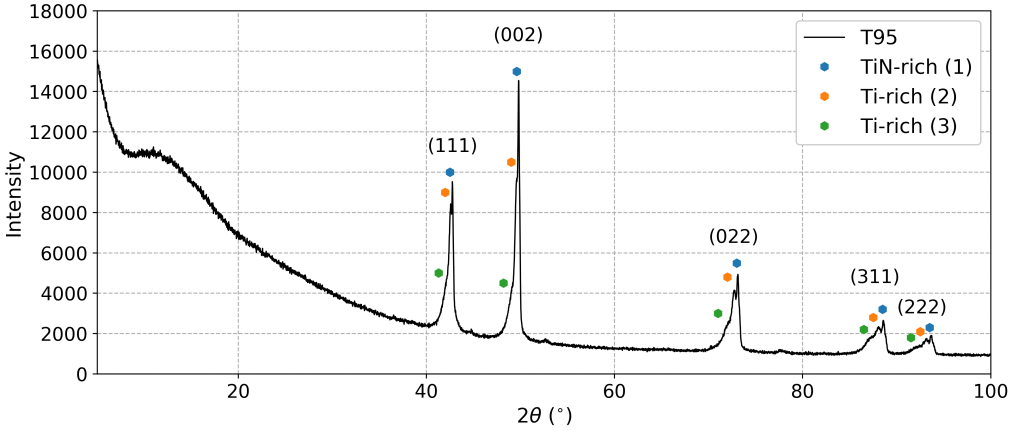


FIG. 6.20 – XRD pattern for collected precipitates from T95 steel.

### 6.5.4 Summary of XRD analysis

The three steels clearly have three different sets of precipitates. All the XRD analyses were done using the XRD software Jade. The L80 steel, which contains the lowest amount of precipitates, appears to contain some oxide phases as well. ML80 steel (Mo-loaded) seems to have only one type of precipitate, $Mo_2C$-rich. Finally the T95 sample, unlike the X70 steels (where a range of compositions was found), appears to contain three Ti-rich precipitates with different but precise compositions. Quantitative XRD analysis provides much more information regarding the compositions, sizes and amounts of each type of precipitates.

## 6.6 Rietveld refinement and quantitative XRD analysis

The Rietveld refinement method is the crucial (and difficult) part of precipitate analysis. The procedure is described in Chapter 3.

### 6.6.1 L80 steel

The L80 QXRD analysis was difficult because of the two oxide phases present in the collected powder. Simple XRD analysis (using Jade software) indicated that the two oxides are $As_2O_3$ and $CuAl_2O_4$. In order to provide quantitative analysis, it is necessary to include those phases in the refinement. Without addition of these phases, it is not possible to calculate the relative abundance of the precipitates in the collected residues.

The Topas final refinement of the L80 XRD pattern is presented in Figure 6.21 and Table 6.9. The amount of oxide phases is quite low; a simple calculation (using the mass of the collected residues and the weight fraction of the oxide phases calculated by Topas) gives a concentration of 0.4 ppm for Al (530 ppm in the steel) and 0.48 ppm for Cu (2200 ppm in the steel). It also gives a concentration of 0.9 ppm for As in precipitate form which appears to be within the range of the As steel composition according to EVRAZ. The actual As steel composition is not displayed in Table 3.1 as it is not provided by EVRAZ.

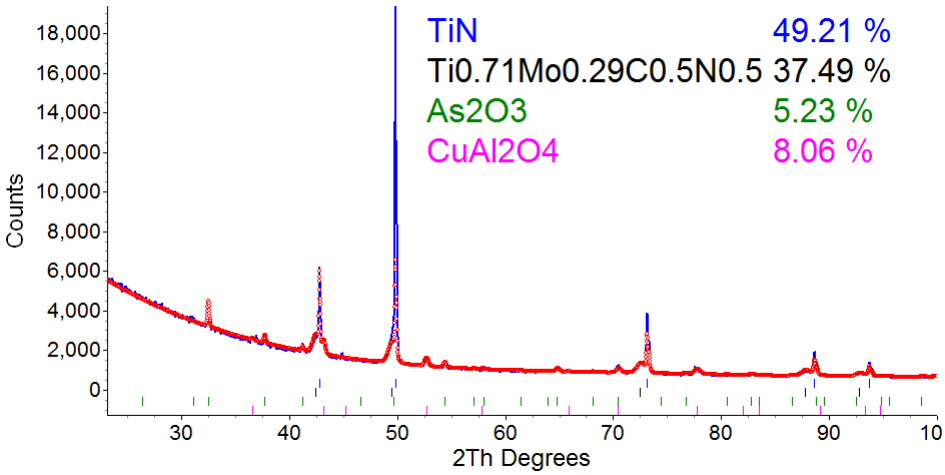


FIG. 6.21 – QXRD analysis for collected precipitates from L80 steel.

TABLE 6.9 – QXRD results for precipitates in L80 steel.

| Precipitate | a (Å) | Strain (%) | $L_{vol}$ (nm) | $\bar{R}$ (nm) | wt% |
|---|---|---|---|---|---|
| TiN | 4.25 | 0.04 | 4000 | - | 49.2 |
| $Ti_{0.71}Mo_{0.29}C_{0.5}N_{0.5}$ | 4.28 | 0 | 11.6 | 4.5 | 37.5 |
| $As_2O_3$ | 11.07 | 0.09 | 99.3 | - | 5.2 |
| $CuAl_2O_4$ | 8.06 | 0.16 | 151.5 | - | 8.1 |

The (111) peak of the TiN-rich phase is correctly refined, while the (002) is not. According to the literature [58], the expected relative intensity of the (111) peak compared to the (002) peak would be 72%. However, in the L80 XRD pattern the relative intensity is 27%. This anomaly appears to be linked to a preferred orientation. As detailed in Section 5.5.3 for precipitates extracted from TWX70 steel, this is likely due to the sample preparation before doing the XRD analysis. No other explanation other than the sample preparation was found. This (002) peak was not taken into account when fitting the diffraction pattern. This will not introduce errors in the Rietveld refinement because only one peak is left behind. The (111), (022), (311) and (222) peaks are sufficient to provide quantitative analysis. Their relative intensities are similar to the one given in the PDF file (ICDD database).

The precipitate sizes calculated by Rietveld refinement are in good agreement with the sizes

measured by SEM. QXRD analysis gives a mean size of 4.5 nm for the small precipitates. SEM analysis gave a size of 4.4 nm for the small precipitates.

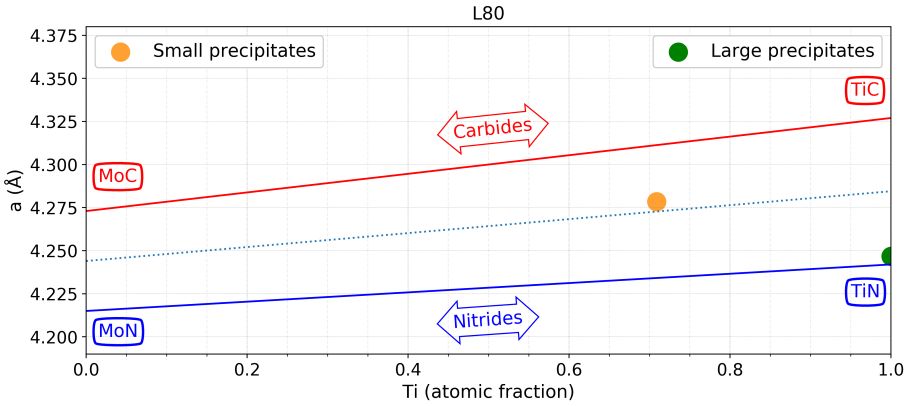


FIG. 6.22 – Lattice parameters for precipitates as a function of Ti contents for L80 steel.

Figure 6.22 shows the comparison between the lattice parameters of the different phases and their Ti atomic contents. As mentionned previously for X70 steel in Chapter 5, Section 5.6.2, it was noted that Topas refinement was not sensitive to C and N composition. A more precised analysis such as TEM-EDX analysis is required to validate these compositions. The QXRD results are within the range of allowed lattice parameters.

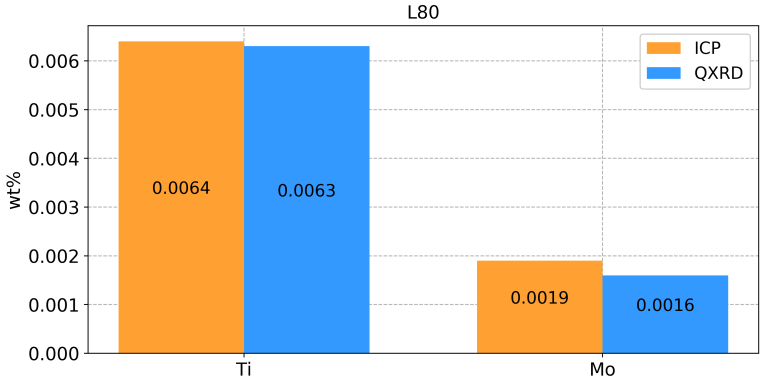


FIG. 6.23 – Comparison between ICP and QXRD results for collected precipitates from L80 steel.

Figure 6.23 shows that the amounts of Ti and Mo in precipitate form calculated through the QXRD analysis are consistent with the amounts calculated through the ICP analysis. The

calculated (by QXRD) amount of N in precipitate form is 0.0017 wt% (0.008 wt% in the steel composition). The calculated amount of C in precipitate form is 0.0003 wt% (0.254 wt% in the steel composition). Other carbides (such as $Fe_3C$) may have dissolved during matrix dissolution.

EDX analysis showed that the average Mo content was 0.1 for the small precipitates. QXRD analysis combined with ICP analysis shows that the average Mo content is 0.3 for the small precipitates. Therefore, there is a great difference between the two analyses. This could be due to the fact that EDX analysis is localized and the number of analyzed precipitates is low compared to QRXD analysis where the whole sample is accounted for. However, EDX analysis is a direct analysis and is therefore more reliable. Nevertheless, QXRD and ICP analyses are in good agreement and QXRD results are physically acceptable.

### 6.6.2 ML80 steel

XRD analysis of the ML80 sample showed only one type of precipitate ($Mo_2C$-rich). ICP analysis indicated that the two main elements present in precipitate form were Mo and Cr. Therefore it is fair to assume that the precipitates should be of the form (Mo,Cr)C.

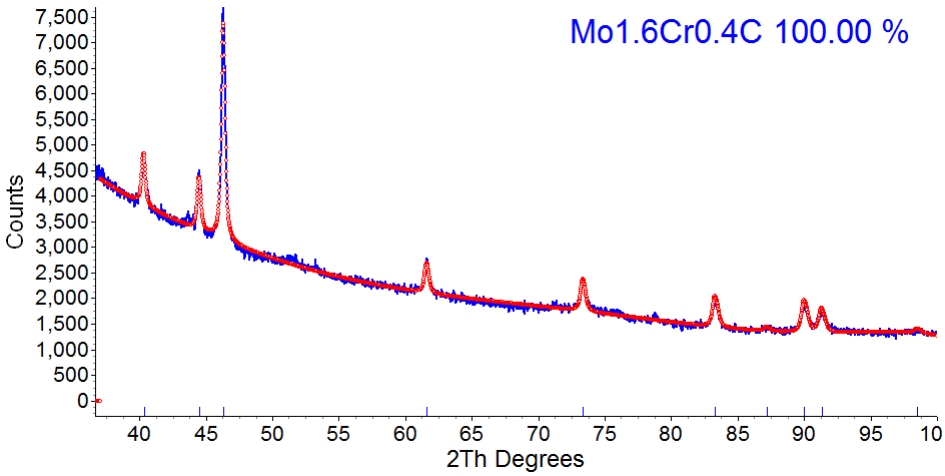


FIG. 6.24 – QXRD analysis for collected precipitates from ML80 steel.

Topas refinement results fro the ML80 sample are presented in Figure 6.24 and Table 6.10. In

order to fit the experimental XRD pattern only one phase was added. The precipitate sizes calculated by Rietveld refinement are in good agreement with the sizes measured by SEM. QXRD analysis gives a mean size of 10.4 nm for the small precipitates. SEM analysis gave a size of 8.6 nm for the small precipitates.

TABLE 6.10 – QXRD results for extracted precipitates in ML80 steel.

| Precipitate | (a, b, c) (Å) | $L_{vol}$ (nm) | $\bar{R}$ (nm) | wt% |
|---|---|---|---|---|
| $Mo_{1.57}Cr_{0.43}C$ | (2.99, 2.99, 4.72) | 26.8 | 10.4 | 100 |

The lattice parameters of hexagonal $Mo_2C$ are $a_{Mo_2C}$ = 3.0185 Å and $c_{Mo_2C}$ = 4.7456 Å. It was shown that Cr and C affect the structure of $(Mo_{1-x}Cr_x)_2C_y$ [19]. The lattice parameters of such a structure are calculated with Equations 6.1 and 6.2.

$$a(x, y) = 3.0185 - 0.1823x - 0.0017(1.00 - y) \tag{6.1}$$

$$c(x, y) = 4.7456 - 0.2861x - 0.1939(1.00 - y) \tag{6.2}$$

where x is the Cr composition and y is the carbon content. For x = 0.2 and y = 1 (calculated compositions with Topas), $a_{Mo_{1.6}Cr_{0.4}C}$ = 2.98 Å and $c_{Mo_{1.6}Cr_{0.4}C}$ = 4.69 Å. The value for a is in good agreement with the value calculated with Topas ($a_{topas}$ = 2.99 Å). The value for c is a bit different for the one calculated with Topas ($c_{topas}$ = 4.72 Å). A higher value of $c_{topas}$ suggests that the carbon content is higher than 1. For instance, if x = 0.2 and c = 4.72, Equation 6.2 gives a carbon content y of 1.2. As mentionned previously for X70 steel in Chapter 5, Section 5.6.2, it was noted that Topas refinement was not sensitive to C and N composition. Further analysis would be needed to accurately determine the carbon content of these precipitates.

Figure 6.25 presents the comparison between the QXRD and ICP analysis for the Mo and Cr contents in precipitate form. The calculated amounts using QXRD and ICP are in good agreement and the mass balance is closed. The calculated amount of C in precipitate form is 0.0074 wt% (0.25 wt% in the steel composition). Other carbides (such as $Fe_3C$) may have dissolved during matrix dissolution.

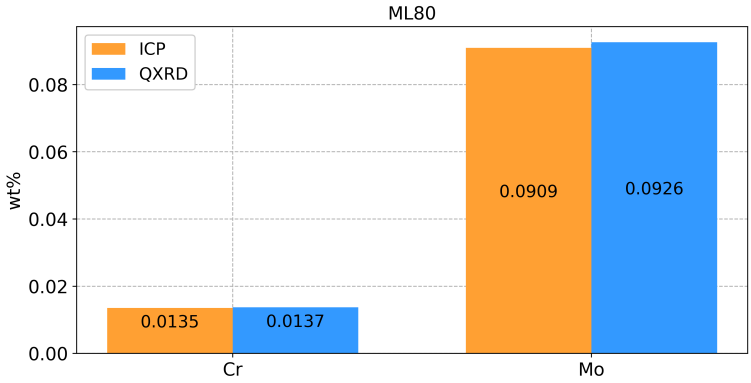


FIG. 6.25 – Comparison between ICP and QXRD results for ML80 steel.

EDX analysis showed that the average Cr content was 0.03 for the small precipitates extracted from ML80 steel. The value calculated with Topas is much higher (0.2). As discussed before, this could be due to the fact that EDX analysis is localized. The number of analyzed precipitates is not statistically relevant compared to QXRD analysis. However, EDX analysis is a direct and more accurate analysis. Nevertheless, the lattice parameters calculated with Topas are physically consistent and ICP and QXRD results are in good agreement, i.e., the mass balance is closed.

### 6.6.3 T95 steel

The ICP analysis showed that the two main constituents of the precipitates were Ti and Mo. XRD analysis indicates that three different Ti-rich phases coexist in the collected powder. Two precipitates are close to pure TiN (sharp peaks), while the third precipitate produces broad peaks. Despite the high Cr content in the steel, none appears to be in precipitate form. The solubility of Cr in ferrite is 0.025 wt% at room temperature though. This suggests that other precipitates containing Cr may have dissolved during matrix dissolution. As discussed in Chapter 2, complex (Fe,Cr,Mo)C precipitates may have been present in the steel and may have dissolved in HCl.

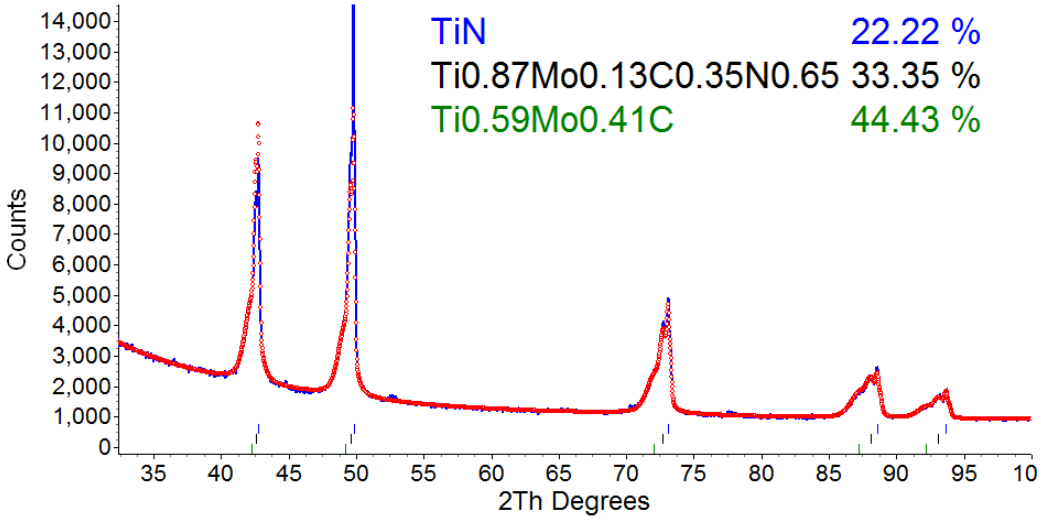


FIG. 6.26 – QXRD analysis for collected precipitates from T95 steel.

The Topas refinement for the T95 sample is presented in Figure 6.26 and Table 6.11. The same issue with the intensity of the TiN (111) and (002) peaks was encountered (see L80 XRD pattern in Figure 6.21). The only way to provide a consistent refinement was to ignore the high intensity (002) diffraction peak. However, the (111) TiN peak is here over-fit, which could lead to an overestimation of the Ti amount in the precipitates.

The precipitate sizes calculated by Rietveld refinement are in less good agreement with the sizes measured by SEM than for L80 steel and ML80 steel. QXRD analysis gives a mean size of 2.4 nm for the small precipitates. SEM analysis gave a size of 5.2 nm for the small precipitates. The particles that were measured by SEM may be agglomerates of 2 individual precipitates. Even if the suspension was free of any agglomerates it would have been difficult to observe 2 nm precipitates because of the SEM resolution.

TABLE 6.11 – QXRD results for extracted precipitates in T95 steel.

| Precipitate | a (Å) | Strain (%) | $L_{vol}$ (nm) | $\bar{R}$ (nm) | wt% |
|---|---|---|---|---|---|
| TiN | 4.25 | 0.053 | 4000 | - | 22.2 |
| $Ti_{0.87}Mo_{0.13}C_{0.35}N_{0.65}$ | 4.27 | 0.152 | 4000 | - | 33.4 |
| $Ti_{0.59}Mo_{0.41}C$ | 4.30 | - | 6.2 | 2.4 | 44.4 |

A single pure nitride phase, a single carbonitride phase and a single pure carbide phase are determined by Rietveld refinement. Figure 6.27 shows the comparison between the lattice parameters of the different phases and their Ti atomic contents. The three precipitate types are within the range of the allowed lattice parameters. The first large precipitate type is consistent with a pure TiN phase. The second large precipitate type is consistent with a carbonitride phase. The small precipitate type is consistent with an almost pure carbide phase. As mentionned previously for X70 steel in Chapter 5, Section 5.6.2, it was noted that Topas refinement was not sensitive to C and N composition. A more precised analysis such as TEM-EDX analysis is required to validate these compositions.

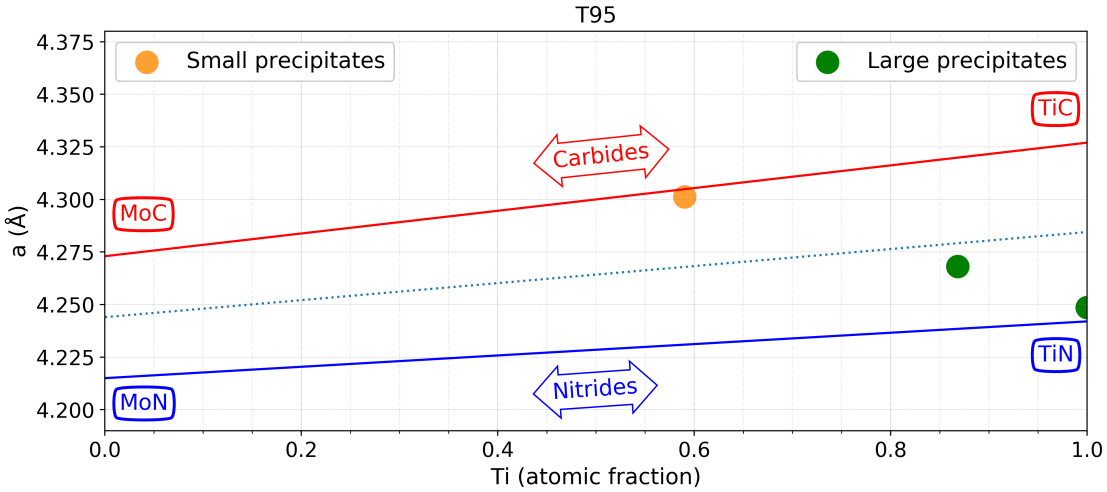


FIG. 6.27 – Lattice parameters for precipitates as a function of Ti contents for T95 steel.

Figure 6.28 shows the comparison between the ICP and QXRD analyses. As expected the amount of Ti is over-estimated by 25%. The mass balance is closed for Mo. It is more difficult to state that the mass balance is closed for Ti. The calculated amount of C in precipitate form is 0.0084 wt% (0.27 wt% in the steel composition). Other carbides (such as $Fe_3C$) may have dissolved during matrix dissolution.

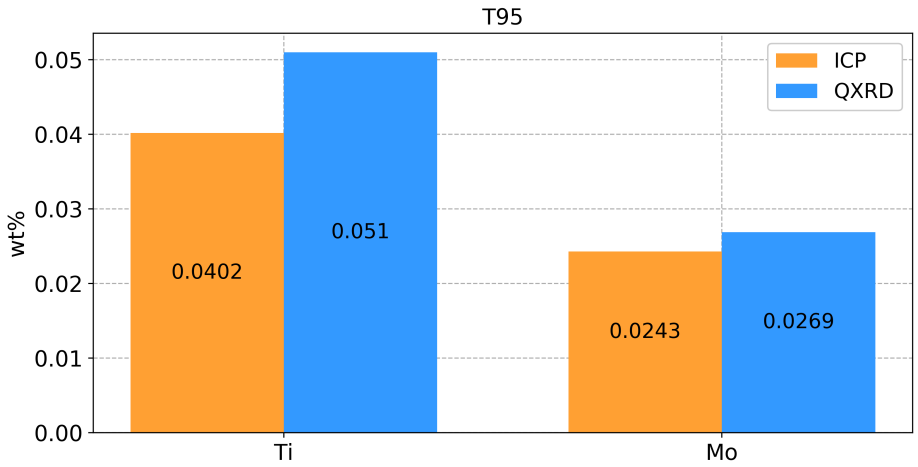


FIG. 6.28 – Comparison between ICP and QXRD results for T95 steel.

EDX analysis showed that the average Mo content for the small precipitates was 0.2. QXRD analysis shows that the average Mo content is 0.41 for the small precipitates. The difference between the two analyses is quite huge. Again, the two techniques are different, i.e., QXRD analysis is an indirect and global analysis, while EDX is a direct and localized analysis. In this case, the mass balance is not as closed as the one for L80 steel or ML80 steel. Therefore, the QXRD results are less supported by the mass balance. In addition, EDX analysis also showed that Cr was present in the small precipitates. Even though ICP analysis showed that all the Cr remained in acidic solution after matrix dissolution.

## 6.7 Summary

Table 6.12 presents a summary of the results for the nanoscale precipitates (less than 10 nm in radius) for the L80, ML80 and T95 steels. Table 6.13 presents a summary of the results for the large precipitates for the L80 and T95 steels. QXRD results were consistent with the ICP analysis and the mass balance was closed for L80 steel and ML80 steel. The results are less good for T95 steel. EDX analysis confirmed the qualitative compositions calculated by QXRD. However, the compositions measured by EDX are quite different from the compositions calculated by Rietveld refinement. SEM analysis confirmed the order of magnitude of the size distribution

of the large and small precipitates for the three steels. All the aforementioned results will be discussed in Chapter 7.

TABLE 6.12 – Nanosize precipitates characteristics for the L80, ML80 and T95 steels.

| Steel | Composition | a or (a, b, c) (Å) | $\bar{R}_{QXRD}$ (nm) | $\bar{R}_{SEM}$ (nm) | $f_v$ (%) |
|---|---|---|---|---|---|
| L80 | $Ti_{0.71}Mo_{0.29}C_{0.5}N_{0.5}$ | 4.28 | 4.5 | 4.4 | 0.005 |
| ML80 | $Mo_{1.57}Cr_{0.43}C$ | (2.99, 2.99, 4.72) | 10.3 | 8.6 | 0.10 |
| T95 | $Ti_{0.59}Mo_{0.41}C$ | 4.30 | 2.4 | 5.2* | 0.050 |

* may be agglomerates of 2 individual precipitates

TABLE 6.13 – Large precipitates characteristics for the L80 and T95 steels.

| Steel | Composition | a (Å) | $\bar{R}_{QXRD}$ (nm) | $\bar{R}_{SEM}$ | $f_v$ (%) |
|---|---|---|---|---|---|
| L80 | TiN | 4.25 | 1500 | 1-4 µm | 0.008 |
| T95 | TiN | 4.25 | 1500 | 1-4 µm | 0.031 |
| | $Ti_{0.87}Mo_{0.13}C_{0.35}N_{0.65}$ | 4.27 | 1500 | 1-4 µm | 0.043 |

# Chapter 7

# Discussion

All the precipitation analysis results were presented in Chapter 5 (X70 and TWX70 steels) and Chapter 6 (L80, ML80 and T95 steels). The purpose of the present chapter is to answer the two questions stated at the beginning of this work, i.e., how Mo and Cr affect precipitation in the heat-treated steels and how the steel thickness affects precipitation in X70 steels.

The different experimental improvements developed in this research work, i.e., modification of the dissolution set-up, the 'multi-peaks' technique during Rietveld refinement and precipitate suspension analysis are considered initially. Then the effect of Mo and Cr on precipitation in L80, ML80 and T95 steels is analyzed. Finally the two X70 steels are compared by considering the precipitation analysis results and the precipitation predictions obtained from NbC precipitation modeling. The model prediction is compared with the experimental results obtained from chemical dissolution.

## 7.1 Modification of the dissolution set-up

As presented in Chapter 3, the experimental set-up as proposed by Lu [2] had an issue. Lu observed the presence of amorphous $SiO_2$ in the collected residues. This amorphous phase was a problem for further analysis. Its presence makes SEM/TEM and XRD analysis more difficult and makes QXRD analysis less accurate.

The present work provides a simple solution to the issue. The idea was to deprive the

system (acid solution and a piece of steel) of $O_2$. Without $O_2$ in solution, Si would not be able to precipitate and form the amorphous $SiO_2$ phase. Nitrogen was injected directly into the acid solution (before and during the steel dissolution), instead of only exposing the solution to a nitrogen atmosphere. Bubbling nitrogen allows for the removal of dissolved oxygen.

Because it would have been time-consuming, no study concerning the flow rate of $N_2$ or the duration of bubbling upstream from the start of the dissolution experiment was conducted. An arbitrary flow rate of one bubble per second, 20 minutes before starting the steel dissolution, was chosen. These parameters prevented the formation of amorphous $SiO_2$. A comparison between the two different dissolution methods is detailed in Chapter 3. Different parameters could be found in order to optimize $N_2$ consumption.

In conclusion, the experimental set-up improvement allowed for the collection of a residual powder free of amorphous $SiO_2$. SEM/TEM and QXRD analyses were therefore facilitated and much more reliable.

## 7.2 Rietveld refinement 'multi-peaks' technique

This section deals with the Rietveld refinement procedure for the X70 steel XRD patterns. As presented in Chapter 5, a closer examination of the different diffraction peaks revealed that they were a superposition of many peaks (especially for the TiN-rich peaks). A classical method for Rietveld refinement, i.e., one phase per set of diffraction peaks, could not be used. Hence a different technique, referred as the 'multi-peaks' technique, was introduced.

In the 'multi-peaks' technique a diffraction peak is deconvoluted into many diffraction peaks. In the example presented in Chapter 5, the number of phases was determined based on the $2\theta$ range of the peak. A phase was chosen for every $0.1^\circ$ increment. For the X70 example, 9 phases were initially introduced and, at the end of the refinement, only 5 phases were really useful (4 phases had a weight fraction of 0%). This approach was the only way to assess correctly the relative abundance of each particular phases, with particular compositions. The

results obtained for the X70 steels were confirmed by SEM-EDX analysis, where ranges of compositions were found for the TiN-rich and NbC-rich precipitates, and were consistent with the results provided by ICP analysis.

## 7.3 Precipitate suspension analysis

Dissolution of the microalloyed steel allows for the collection of precipitate powders. During the collection process, the particles agglomerate. This agglomeration is not an issue regarding XRD/QXRD analysis; however, it is a problem for SEM analysis. Because of agglomeration, it was not possible to analyze individually small or large particles. In addition, small particles were not discernable, so that their size distribution was not quantifiable. Agglomerates of small particles trap larger particles, making size and composition analysis more difficult. To remedy this problem, a mixture of a small amount of residual powder and ethanol, followed by 20 minutes in an ultrasonic bath, provided a suspension that could be deposited onto carbon tape or carbon grid. This technique was shown in Chapters 5 and 6 to be efficient to quantify particle size distributions and compositions, but still very good for the smallest precipitates.

## 7.4 Effect of Mo and Cr on precipitation in heat treated steels

The first objective was to determine the effect of Mo and Cr contents on precipitation in heat treated steels. Chapter 6 provided the experimental results obtained for the L80, ML80 and T95 steels. The steels were all heat treated steels with different quench and temper conditions. The conditions and steel compositions are detailed in Chapter 3.

### 7.4.1 L80 precipitate analysis

L80 was tempered for 2 h at 680°C and then air cooled. Table 7.1 presents a summary of the L80 precipitates collected after HCl dissolution. R is the radius of the particle, a is the lattice paramter and $f_v$ is the volume fraction. TiN was certainly formed during casting, based on its

solubility [22] and the size of the particles (several microns), as detailed in Chapter 2, Section 2.2. $Ti_{0.71}Mo_{0.29}C_{0.5}N_{0.5}$ is believed to form before quenching and tempering and during the formation of the pipe, because of the solubility of Ti in the presence of N. In addition, the tempering temperature (680°C) does not allow for the formation of TiN-rich particles. It is important to note that the volume fraction of TiN (large particles) is higher than the volume fraction of the nanoscale particle $Ti_{0.71}Mo_{0.29}C_{0.5}N_{0.5}$.

TABLE 7.1 – Characteristics of precipitates collected from L80 steel.

| Composition | a (Å) | $\bar{R}_{QXRD}$ (nm) | $\bar{R}_{SEM}$ | $f_v$ (%) |
|---|---|---|---|---|
| TiN | 4.25 | 1500 | 1-4 µm | 0.008 |
| $Ti_{0.71}Mo_{0.29}C_{0.5}N_{0.5}$ | 4.28 | 4.5 | 4.4 nm / 13.8 nm | 0.005 |

EDX analysis showed that the average Mo content was 0.1 for the small precipitates. QXRD analysis combined with ICP analysis shows that the average Mo content is 0.3 for the small precipitates. Therefore, there is a great difference between the two analyses. This could be due to the fact that EDX analysis is localized and the number of analyzed precipitates is low compared to QRXD analysis where the whole sample is accounted for. In addition, EDX analysis does not use standards; therefore, it is difficult to provide the exact composition of the particles. However, EDX analysis is a direct analysis and is therefore more reliable. Nevertheless, QXRD and ICP analyses are in good agreement and QXRD results are physically acceptable (lattice parameters as a function of Ti content).

TiN and $Ti_{0.71}Mo_{0.29}C_{0.5}N_{0.5}$ are thus the only precipitates that were collected according to ICP and QXRD analyses. However, this does not mean that they were the only precipitates in L80 steel. The calculated amount of C in precipitate form is 0.0003 wt% (0.254 wt% in the steel composition). Therefore, C must have been in other precipitate forms (0.2537 wt% is higher than the solubility of C in iron). It was shown through ICP analysis that 100% of Cr remains in solution after dissolution, as does 90% of Mo, 79% of Ti. It is possible that part of Cr and Mo that remain in solution after dissolution were in precipitate form, such as $(Fe_xCr_yMo_z)C_n$ as reported by Hou [18] and Depinoy [13] which is unstable in HCl. No clear Cr precipitates were observed when the steel sample was imaged in the SEM before dissolution. ThermoCalc

simulation predicts formation of complex (Fe,Mo,Cr,Ti)3C2 and MoC precipitates for L80 steel (Fe-Mo-Cr-Ti-C system using the database TCFE6: Steels/Fe-alloys). The calculated phase diagram can be found in Appendix D.

### 7.4.2 ML80 precipitate analysis

ML80 was tempered for 3 h at 690°C and then air cooled. Table 7.2 presents a summary of the ML80 precipitates collected from HCl dissolution. SEM analysis and QXRD analysis were consistent regarding the size of the precipitates. A mean radius size of 8.6 nm was determined by SEM and a mean radius size fo 10.3 nm was calculated by Rietveld refinement. Only nanoscale particles were observed. EDX and QXRD analysis were not consistent though regarding the compositions of the precipitates. Both analyses suggest that the precipitates are Mo/Cr-rich particles. However, the amount of Cr predicted by QXRD analysis (0.215 atom fraction) is much higher than the one determined through EDX (0.03 atom fraction). Nevertheless, the semi-quantitative EDX analysis was only done on 18 agglomerates and may not be representative of the whole sample. As detailed in Chapter 6, the lattice parameters determined by QXRD analysis are in good agreement with the Cr content (0.215 atom fraction) also determined by Rietveld analysis, based on a work by Knepfler [19]. This Cr content also permitted to close the mass balance. ICP and QXRD analyses were in good agreement.

TABLE 7.2 – Characteristics of precipitates collected from ML80 steel.

| Composition | (a, b, c) (Å) | $\bar{R}_{QXRD}$ (nm) | $\bar{R}_{SEM}$ (nm) | $f_v$ (%) |
|---|---|---|---|---|
| $Mo_{1.57}Cr_{0.43}C$ | (2.99, 2.99, 4.72) | 10.3 | 8.6 | 0.099 |

Due to the very low Ti and N content, no TiN particles were formed during casting. All the collected precipitates ($Mo_{1.57}Cr_{0.43}C$) were formed during quenching and tempering, based on the precipitate sequence in Cr-Mo steels reported by Lee [17]. The solubility products proposed by Pavlina [23] suggest that, for the ML80 composition, Mo carbides cannot form in austenite and ferrite at temperatures above 830°C. Therefore, the austenization step that precedes Q&T allows for dissolution of any pre-existing Mo carbides.

The solubility products also permit estimation of the volume fraction of $Mo_2C$ at equilibrium (at 690°C). The calculation predicts a volume fraction of 0.38%, which is higher than the experimental value ($\simeq$ 0.1%) obtained for the $Mo_{1.57}Cr_{0.43}C$ particles. This suggests that Mo formed other precipitates. Based on the ICP analysis, 94% of Cr and 79% of Mo remained in solution after dissolution. As for L80 steel, it is possible that a part of Cr and Mo that remained in solution after dissolution was in precipitate form such as $(Fe_xCr_yMo_z)C_n$ [18, 13], which are unstable in HCl. ThermoCalc simulation predicts formation of complex (Cr,Fe,Mo,Ti)3C2, MoC and (Mo,Cr)3C2 precipitates for ML80 steel (Fe-Mo-Cr-Ti-C system using the database TCFE6: Steels/Fe-alloys). The calculated phase diagram can be found in Appendix D.

### 7.4.3 T95 precipitate analysis

T95 steel was tempered for 2 h at a temperature lower than 680°C and then air cooled. Table 7.3 presents a summary of the T95 precipitates collected from HCl dissolution. TiN and $Ti_{0.87}Mo_{0.13}C_{0.35}N_{0.65}$ are assumed to form during casting and/or pipe formation because of the size of the particles and solubility of TiN-rich particles [22, 1]. $Ti_{0.59}Mo_{0.41}C$ is believed to form before quenching and tempering and during TMCP, because of the solubility of Ti in the presence of C [22, 1]. Tempering temperature around 600-700°C is too low for formation of TiC-rich particles. Austenitization temperature around 900°C is not high enough to dissolve these kind of precipitates.

TABLE 7.3 – Characteristics of precipitates collected from T95 steel.

| Composition | a (Å) | $\bar{R}_{QXRD}$ (nm) | $\bar{R}_{SEM}$ | $f_v$ (%) |
|---|---|---|---|---|
| TiN | 4.25 | 1500 | 1-4 µm | 0.031 |
| $Ti_{0.87}Mo_{0.13}C_{0.35}N_{0.65}$ | 4.27 | 1500 | 1-4 µm | 0.043 |
| $Ti_{0.59}Mo_{0.41}C$ | 4.30 | 2.4 | 5.2 nm | 0.050 |

The particle size analysis showed a mean radius almost twice as large as the value calculated by QXRD analysis. This could be due to the fact that the observed particles were agglomerates of smaller particles. The SEM resolution did not allow for the distinction between individual precipitates of 2.4 nm in size and small agglomerates. In addition, ultrasonic bath may not be

able to break this kind of small agglomerates. EDX analysis showed that the average Mo content for the small precipitates was 0.2. QXRD analysis shows that the average Mo content is 0.41 for the small precipitates. The difference between the two analyses is quite huge. Again, the two techniques are different, i.e., QXRD analysis is an indirect and global analysis, while EDX is a direct and localized analysis. In this case, the mass balance was not as closed as the one for L80 steel or ML80 steel. Therefore, the QXRD results are less supported by the mass balance. In addition, EDX analysis also showed that Cr was present in the small precipitates. Even though ICP analysis showed that all the Cr remained in acidic solution after matrix dissolution.

ICP analysis showed that 100% of Cr remained in solution after dissolution, as does 87% of Mo and 2% of Ti. A part of the Cr and Mo that remained in solution after dissolution likely were in precipitate form such as $(Fe_xCr_yMo_z)C_n$ as reported in [18, 13] which is unstable in HCl. ThermoCalc simulation predicts formation of complex (Cr,Fe,Mo,Ti)C, MoC and (Cr,Mo)3C2 precipitates for T95 steel (Fe-Mo-Cr-Ti-C system using the database TCFE6: Steels/Fe-alloys). The calculated phase diagrams can be found in Appendix D.

### 7.4.4 Carbide precipitation in Mo-Cr heat treated steels

The previous analysis showed that only the dissolution of the ML80 steel exhibits the presence of Mo-Cr carbides. Dépinoy showed [13] that four types of carbides form during quenching and tempering of a 2.25wt%Cr-1wt%Mo steel, i.e., $M_2C$, $M_3C$, $M_7C_3$ and $M_{23}C_6$, with M = Fe, Cr and/or Mo. The precipitation sequence was also determined. $M_3C$ (Fe-rich with Cr) precipitates first due to decomposition of retained austenite, followed by the nucleation of $M_7C_3$ (Cr-rich with Fe) at the interface of $M_3C$ and the matrix. Then $M_2C$ (Mo-rich with Cr) precipitates homogeneously from the matrix. Finally $M_{23}C_6$ (Fe-rich with Cr) precipitates at the interfaces between other precipitates and the matrix. This latter phase appears to be the most stable one. With increasing time and temperature $M_{23}C_6$ particles coarsen while the other phases dissolve because of their lower stability. Dépinoy [13] also showed that heating prior to the isothermal step of quenching and tempering noticeably affects the precipitation, since all carbides have already precipitated before the isothermal holding begins.

Dépinoy studied a 2.25wt%Cr-1wt%Mo steel [13], which has a Cr content twice as high as in the T95 steel, and a Mo content twice as high as in the ML80 steel. It is then difficult to ensure that the same sequence appeared in the L80, ML80 and T95 steels. However, it is reasonable to assume that the tempering time, tempering temperature and steel composition (Mo and Cr) affect the precipitation sequence, the type of precipitates and their composition.

In this work, unfortunately, it was only possible to collect $M_2C$ (Mo-rich with Cr) phases because of their stability in HCl solution. Cr [37] and Mo [36] carbides are supposed to be stable in HCl. However, they are not observed in the heat treated steels. It is possible that other Mo and Cr precipitates are present in the L80, ML80 and T95 steels in form of Fe based carbides which are not stable in HCl; nevertheless, it was not possible to collect them and analyze them. ThermoCalc simulations as presented in Appendix D show that complex $(Fe_xCr_yMo_z)C_n$ precipitates can form in L80, ML80 and T95 steels.

It would be of interest to combine HCl dissolution with another chemical/electrochemical dissolution method to collect the precipitates that are unstable in HCl, such as a halogen-based solution ($Br_2$ of $I_2$ in ethanol) [2, 33]. This would be the only way to assess the effect of Mo and Cr on precipitation in L80, ML80 and T95 steels.

## 7.5 Effect of wall thickness on precipitation in X70 steels

The second objective of this work was to determine the effect of pipe wall thickness on nano-precipitation of NbC-rich particles. Two X70 steels were analyzed in this work, a regular X70 steel (11 mm thick) and a thick wall X70 steel (TWX70 - 17 mm thick).

The processing conditions were assumed to be similar, i.e., the steels had the same finish rolling temperature (ca. 790°C), the same cooling rate during laminar cooling (ca. 15°C/s) and the same coiling temperature (ca. 575°C). Because of different thicknesses, the accelerated coolings are different in order to achieve a similar cooling rate. The only two differences are their compositions and their thicknesses.

The difference in composition constitutes an obstacle to the assessment of the true effect

of the thickness. First of all, the experimental results presented in Chapter 5 concerning the large precpitates will be discussed. Then the modeling results for both Lu's steels [2] and the X70/TWX70 steels will be discussed and compared to the experimental results for the nanoscale precipitates.

### 7.5.1 Effect of the thickness on the precipitation of large particles

Table 7.4 presents a summary of large precipitates in X70 steel, by QXRD and SEM analysis. The size and compositions predicted by QXRD analysis were consistent with the SEM observations and the EDX measurements, where a range of compositions was found. The total volume fraction of large precipitates was calculated as 0.037%.

TABLE 7.4 – Characteristics of large precipitates in X70 steel.

| Composition | a (Å) | $\bar{R}_{QXRD}$ | $R_{SEM}$ | $f_v$ (%) |
|---|---|---|---|---|
| $Ti_{0.97}Nb_{0.03}N_{0.68}C_{0.32}$ | 4.26 | 1.5 µm | 1-4 µm | 0.017 |
| $Ti_{0.86}Nb_{0.14}N_{0.88}C_{0.12}$ | 4.27 | 1.5 µm | 1-4 µm | 0.004 |
| $Ti_{0.64}Nb_{0.36}N$ | 4.30 | 1.5 µm | 1-4 µm | 0.007 |
| $Ti_{0.50}Nb_{0.50}N$ | 4.32 | 1.5 µm | 1-4 µm | 0.002 |
| $Ti_{0.30}Nb_{0.70}N$ | 4.35 | 1.5 µm | 1-4 µm | 0.007 |

Table 7.5 presents a summary of large precipitates in TWX70 steel, by QXRD and SEM analysis. The size and compositions predicted by QXRD analysis were consistent with SEM observations and EDX measurements, where a range of compositions was found. The total volume fraction of large precipitates is calculated as 0.070%.

The total volume fraction calculated by QXRD analysis for large precipitates in TWX70 steel is more than twice as high (0.070 %) as the volume fraction for large precipitates in X70 steel (0.037 %), despite the very similar nominal composition in Ti (0.016 wt% for both steels) an N (0.007 wt% for X70 steel and 0.009 wt% for TWX70 steel). This is the first main difference in terms of the precipitation of large precipitates between X70 and TWX70 steels. Therefore, the thickness of the steel appears to have an effect on microscale precipitation, i.e., the thicker the

TABLE 7.5 – Characteristics of large precipitates in TWX70 steel.

| Composition | a (Å) | $\bar{R}_{QXRD}$ | $R_{SEM}$ | $f_v$ (%) |
|---|---|---|---|---|
| $Ti_{0.86}Nb_{0.14}N$ | 4.26 | 1.5 µm | 1-4 µm | 0.028 |
| $Ti_{0.84}Nb_{0.16}N$ | 4.27 | 1.5 µm | 1-4 µm | 0.009 |
| $Ti_{0.61}Nb_{0.39}N_{0.63}C_{0.37}$ | 4.29 | 1.5 µm | 1-4 µm | 0.009 |
| $Ti_{0.50}Nb_{0.50}N_{0.78}C_{0.22}$ | 4.32 | 1.5 µm | 1-4 µm | 0.009 |
| $Ti_{0.32}Nb_{0.68}N$ | 4.35 | 1.5 µm | 1-4 µm | 0.016 |

wall the higher the volume fraction of large precipitates. However, it is difficult to be certain of that or to know why based only on this analysis. The analysis is not statistically relevant since only a small piece of steel was taken from a single location in the pipe. TMCP is a very complicated process where many parameters can affect precipitation. Further analysis is therefore needed to validate the results, i.e., the thickness affects microscale precipitation. Taking samples at different location and different stage of TMCP can provide more information regarding microscale precipitation.

### 7.5.2 Effect of thickness on nanoprecipitation

Table 7.6 presents a summary of the steel compositions and the QXRD/SEM results obtained for the nanoscale precipitates collected from X70 and TWX70 steels. The same types of precipitates are observed in both steels. The slight difference in composition is due to the amount of Mo present in the steel. TWX70 has a higher Mo content (0.19 wt%), so that its precipitates are richer in Mo. The difference in volume fraction is due to the Nb and C content in the steel. It is possible to estimate the volume fraction of stoichiometric NbC precipitates based on its solubility product in ferrite. Stoichiometric particles are defined by Equation 7.1.

$$\frac{[Nb]_{NbC}}{A_{Nb}} = \frac{[C]_{NbC}}{A_C} \iff \frac{[Nb]_{eq} - [Nb]_o}{A_{Nb}} = \frac{[C]_{eq} - [C]_o}{A_C} \tag{7.1}$$

where $A_{Nb}$ is the molar mass of Nb, $[Nb]_{NbC}$ is the amount of Nb in NbC in wt%, $[Nb]_{eq}$ is the amount of Nb at equlibrium in wt% and $[Nb]_o$ is the initial amount of Nb in solid solution in

wt%. The solubility product $K_S$ is defined by Equation 7.2.

$$K_S = [Nb]_{eq}[C]_{eq} = 10^{\left(B - \frac{A}{T}\right)} \tag{7.2}$$

where T is the temperature, B = 2.26 and A = 6670 K for NbC in ferrite. Combined together, the two previous equations give a new equation (Equation 7.3) that allows for the calculation of the amount of Nb and C in NbC given an initial composition and temperature.

$$\frac{A_C}{A_{Nb}}[Nb]^2_{NbC} - \left([C]_o + \frac{A_C}{A_{Nb}}[Nb]_o\right)[Nb]_{NbC} + [Nb]_o[C]_o - K_S = 0 \tag{7.3}$$

Knowing the amount of Nb and C in NbC, the density of NbC ($\rho_{NbC}$ = 7.8 g.cm$^{-3}$) and the density of ferrite ($\rho_{Fe}$ = 7.9 g.cm$^{-3}$), it is possible to calculate the volume fraction of NbC in ferrite using Equation 7.4.

$$f_v^{NbC}(\%) = \frac{([Nb]_{NbC} + [C]_{NbC}) \cdot \rho_{Fe}}{\rho_{NbC}} \tag{7.4}$$

The thermodynamic calculation (at T = 790°C) based on the solubility product of NbC [1] predicts a volume fraction of 0.10% for the X70 steel and 0.073% for the TWX70 steel. These values are in good agreement with the volume fractions determined by QXRD as shown in Table 7.6.

TABLE 7.6 – QXRD/SEM nanoscale precipitation summary for X70 and TWX70 steels.

| Steel | wt% C | wt% Nb | wt% Mo | Composition | $\bar{R}_{QXRD}$ (nm) | $\bar{R}_{SEM}$ (nm) | $f_v$ (%) | $\Sigma f_v$ (%) | $f_v^{calc}$ (%) |
|---|---|---|---|---|---|---|---|---|---|
| X70 | 0.052 | 0.090 | 0.137 | $Nb_{0.68}Mo_{0.30}Ti_{0.02}C$ | 4.2 | 7.95 | 0.066 | 0.113 | 0.10 |
| | | | | $Nb_{0.85}Ti_{0.15}C$ | 15.6 | | 0.047 | | |
| TWX70 | 0.043 | 0.067 | 0.192 | $Nb_{0.62}Mo_{0.36}Ti_{0.02}C$ | 5.1 | 4.4 | 0.039 | 0.064 | 0.073 |
| | | | | $Nb_{0.84}Ti_{0.16}C$ | 11.1 | 10.0 | 0.025 | | |

The pipe thickness does not seem to affect the volume fraction of nanoscale precipitates, since the thermodynamic calculations provide similar results to the QXRD results.

The NbC precipitation model developed in Chapter 4 allows for the prediction of the volume

fraction and mean radius in X70 steels. Before discussing and comparing the prediction, the assumptions detailed in Chapter 4 are discussed.

### 7.5.3 Discussion of model assumptions

The first assumption is that only stoichiometric NbC particles are considered. The model does not take into account the precipitation of complex phases such as $Nb_xMo_{1-x}C$ (as observed in the collected precipitates), since three elements would increase the complexity of the model significantly. The second assumption is that the precipitates are spherical particles. This assumption is based on experimental observations, where quasi-spherical precipitates were observed. The third is that there is no interaction between the particles, which is reasonable because of the low volume fractions. The particles are uniformly distributed in the ferrite matrix, where each particle only 'sees' a uniform concentration of Nb and C in the matrix.

Assuming that the interfacial energy ($\gamma$) is constant simplifies the model. The temperature dependency and the radius dependency are difficult to take into account. Also in order to simplify the model, dislocations are assumed to have no effect on nucleation. Only homogeneous nucleation is considered. Good agreement between experimental and simulation results were observed [43] while only considering homogeneous nucleation. However, it is legitimitate to think that considering only homogeneous nucleation will result in a lower nucleation rate, because of higher energy barriers. The nucleation barrier is indeed lower for heterogeneous nucleation. Based on the classical nucleation theory equations considering heterogeneous nucleation would improve the nucleation (due to a lower energy barrier) and growth (due to higher diffusion coefficients) rates. No huge difference would be expected regarding the volume fraction or precipitate sizes. However, the kinetics would be expected to be different. Heterogeneous nucleation could be added to an updated version of the model.

The initial compositions in Nb and C are assumed to be the nominal compositions, even though Nb and C could have already formed other precipitates, such as large cubic (Ti,Nb)(N,C) particles. Nevertheless, it is a first and legitimate start because the actual composition is one of the major unknowns.

The last assumption is to consider that ferrite is the only matrix phase present. It is assumed that all the austenite is transformed before laminar cooling. This also simplifies implementation of NbC precipitation. However, it is known that the transformation of $\gamma$-Fe to $\alpha$-Fe occurs during laminar cooling. Nevertheless, the exact evolution of the phase fraction is difficult to assess. A recent research work [48] is about to provide a model of phase transformation during laminar cooling and will be able to predict the actual phase fraction. The implementation of the phase transformation model into the precipitation model could better predict the volume fraction and radii of nanoscale precipitates.

All the aforementioned assumptions were taken into account and the simulations were run for different compositions and different laminar cooling parameters.

### 7.5.4 Comparison between the simulation and experimental results

As was presented beforehand, the initial solid solution concentration, which is not the nominal concentration, is not known. Because it is not possible to estimate the initial concentration, the input composition is assumed to be the nominal composition. Figure 7.1 presents a comparison between the QXRD and Multipreci results for Lu's steels [2] and for the X70 and TWX70 steels. It should be noted that the Multipreci simulation does not account for the thickness of the pipe as an input parameter.

The simulation of the radii gives good results, with an offset, but a correct overall trend. It may be a coincidence that the gap between the simulation results and the QXRD results are about the same. This may be due to the dispersion value (c = 0.2) used to calculate the mean radii from the $L_{vol}$ values. The simulation of the volume fraction for Lu's steels does not correlate well with the QXRD results (Figure 7.1). This could be due to the 'quality' of the collected precipitates, where a large amount of amorphous $SiO_2$ was present and could make quantification difficult [25]. A similar trend is observed for the predicted and measured volume fractions of the X70 and TWX70 steels. The 'Multipreci' simulations and the experimental measurements show good agreement for both the mean radius and the volume fraction of the precipitates for both X70 steels considering the assumptions that were made. This is surprising considering

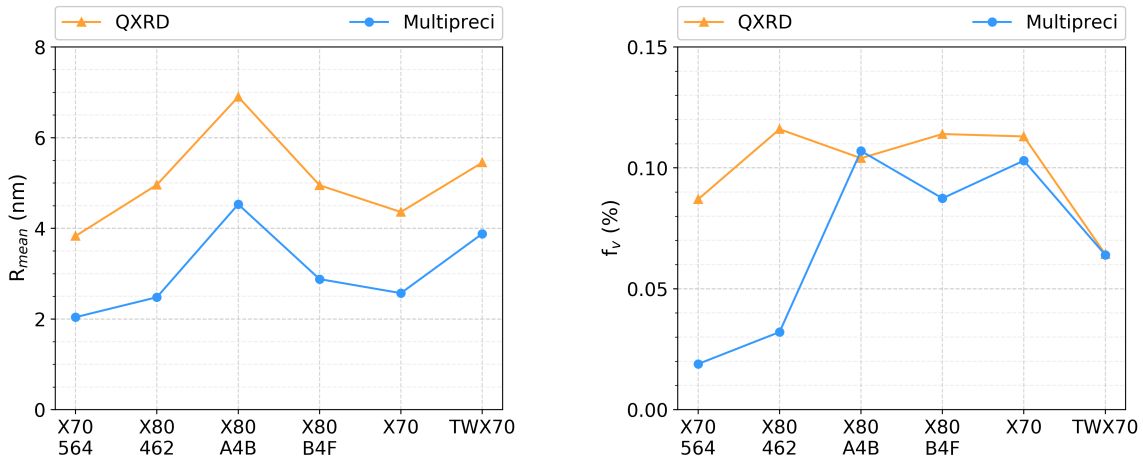


FIG. 7.1 – Comparison between QXRD and simulation results: (A) Mean radius $R_{mean}$ and (B) volume fraction $f_v$.

that only homogeneous nucleation was accounted for.

From the simulations, an estimation of the initial solid solution concentration of Nb and C can be provided. Knowing the experimental volume fractions, it is possible to try and fit the input concentration in order to approach these volume fractions. A total of 10000 simulations was done using the same process conditions used for the X70 and TWX70 steels, i.e., the amount of Nb and C were allowed to vary between 0.001wt% and 0.1wt% with a step of 0.001wt% (hence 10000 simulations).

For each steel, a single initial composition was found that fits the experimental volume fraction. Figure 7.2 presents the nominal compositions ($[Nb]_o$ and $[C]_o$) and initial calculated (by the model) compositions ($[Nb]_o^{calc}$ and $[C]_o^{calc}$) for X70 and TWX70 steels. Figure 7.3 shows the mean radii and volume fractions associated with these compositions, and their agreement with the experimental ones. For the precipitate size the comparison between the QXRD results and the simulation results shows a better agreement than the results that were previously presented (Figure 7.1).

The initial compositions calculated with the Multipreci algorithm are logically lower than the nominal composition of the steels. This is not surprising as some Nb and C already precipitated into the Ti/Nb-rich precipitates or other carbides. Therefore, it is possible to estimate the

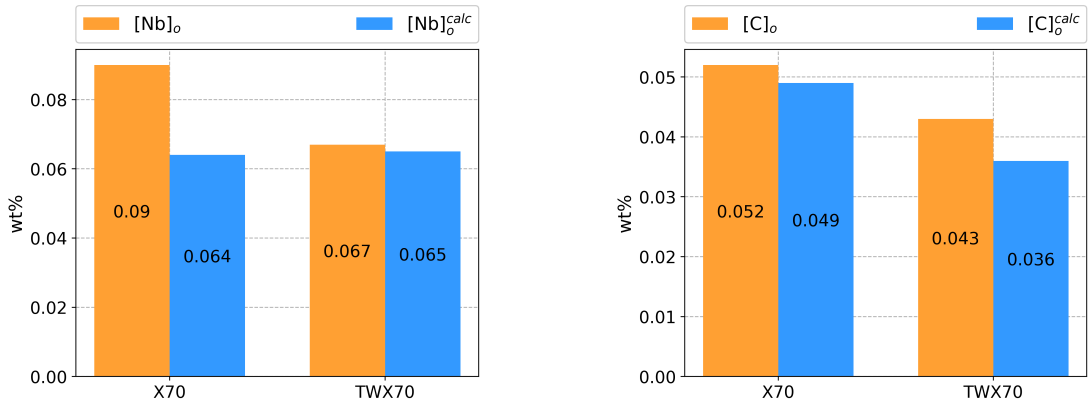


(A) (B)

FIG. 7.2 – Nominal and initial calculated concentrations for X70 and TWX70 steels: (A) wt% Nb and (B) wt% C.

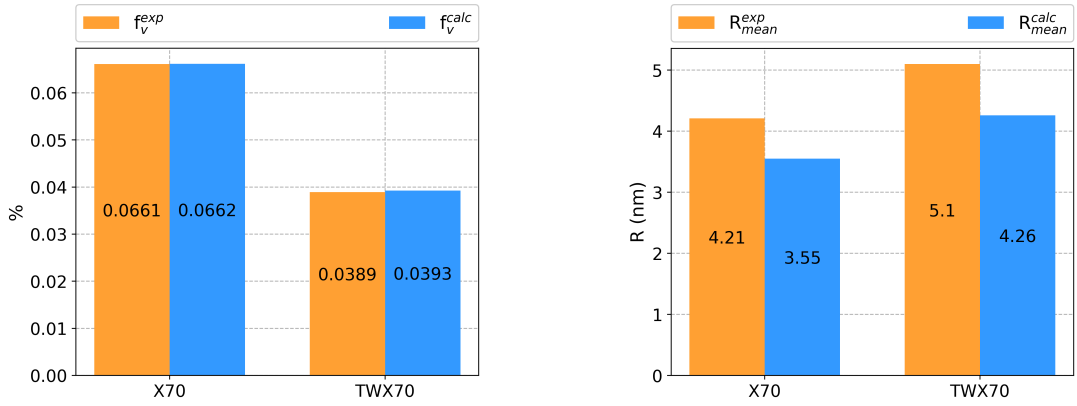


(A) (B)

FIG. 7.3 – Comparison between QXRD and simulation results: (A) Volume fraction $f_v$ and (B) mean radius $R_{mean}$.

amount of Nb and C that would be actually available for the nano-precipitation. The correlation between the experimental results and the prediction seems to be quite good. However, the initial amount of Nb predicted by the simulations does not make sense for TWX70 steel. Based on QXRD analysis, 0.023 wt% of Nb has already been precipitated in larger Ti-rich precipitates. Therefore, only 0.044 wt% of Nb would remain available for NbC nanoprecipitation, which is lower than the prediction (0.065 wt%). Concerning X70 steel, based on QXRD analysis, 0.009 wt% of Nb has already been precipitated in larger precipitates. Therefore, 0.081 wt% of Nb would remain available for NbC nanoprecipitation, which is higher than the prediction (0.064 wt%). The model is therefore not able to predict accurately the initial amount of Nb and C

available for NbC nanoprecipitation.

Only one issue remains Mo is present in the precipitates and its precipitation is not taken into account in the simulations. The current state of the model does not allow for Mo participation. However, Mo and Nb are similar and tend to precipitate together only in very fine precipitates. Thus it could be of interest to consider that the aforementioned initial composition could be a composition associated with Nb and Mo at the same time.

To this point of the analysis, the thickness of the pipe has not been accounted for. All the calculations were based only on thermodynamics and are in good agreement with the experimental (QXRD) results. Therefore it is fair to consider that the thickness of the pipe has no particular effect on nanoprecipitation because it was not used as a relevant parameter to explain the differences between the two X70 steels in terms of nanoprecipitation, except if the composition varied from the surface of the pipe to the centerline. This study does not provide local precipitation results.

## 7.6 Temperature optimization

NbC precipitation model can be used to find the temperature at which the precipitation is optimized, i.e., where the volume fraction is the highest for the smallest particles.

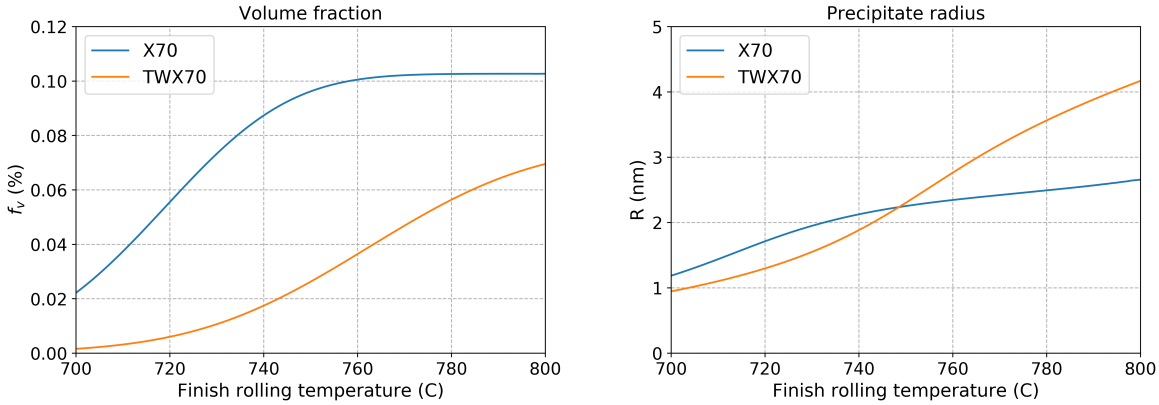


(A) (B)

FIG. 7.4 – Mean precipitate radius and volume fraction as a function of finish rolling temperature: (A) Volume fraction and (B) mean radius.

Figure 7.4 presents the the simulation results of the mean precipitate radius and the volume fraction of precipitates as a function of finish rolling temperature. A constant cooling rate of 15°C/s was chosen, i.e., when the finish rolling temperature changes, the coiling temperature changes as well. It is then possible to calculate the precipitation strengthening defined by Equation 4.15 [1] in Chapter 2, Section 2.3. Figure 7.5 presents the simulation results of precipitation strengthening as a function of finish rolling temperature.

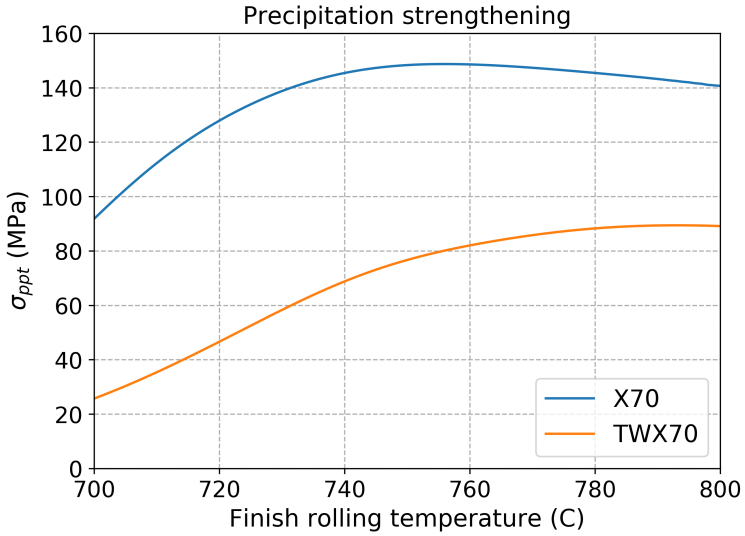


FIG. 7.5 – Precipitation strengthening as a function of finish rolling temperature.

A maximum for the precipitation strengthening is found for X70 steel at T = 756°C ($\sigma_{\text{ppt}}$ = 149 MPa) and for TWX70 steel at T = 793°C ($\sigma_{\text{ppt}}$ = 89 MPa). It is also possible to determine the effect of coiling interupt temperature. A constant finish rolling temperature (FRT = 790°C) was chosen for the subsequent simulations. Figure 7.6 presents the simulation results for the precipitation strengthening as a function of coiling interupt temperature. It appears that CIT does not have a significant impact on $\sigma_{\text{ppt}}$.

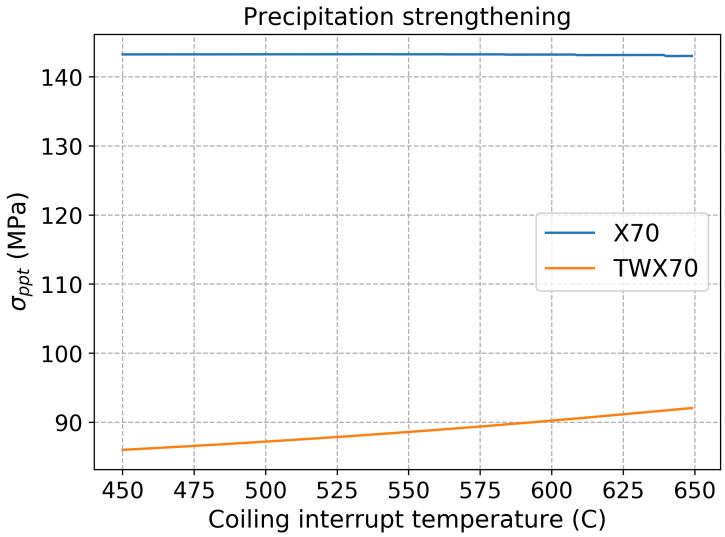


FIG. 7.6 – Precipitation strengthening as a function of coiling interupt temperature.

## 7.7 Summary

In this chapter the following questions were raised: How can the Mo and Cr compositions affect precipitation in the L80, ML80 and T95 steels? How does the thickness of an X70 pipe affect precipitation? It is possible that the technique used to collect the precipitates did not allow collection of all precipitate phases in the heat treated steels. In order to truly assess the effect of Mo and Cr on precipitation in heat treated steels, a different extraction technique has to be applied. Concerning the X70 steels, a clear difference in precipitation of large particles was found. The volume fraction in TWX70 steel appeared to be more than twice as high as the volume fraction in X70 steel. However, it is not possible to provide a reason why there is a difference in microscale precipitation. Further statistical analysis is needed. Based on the experimental results and the 'Multipreci' algorithm adapted to laminar cooling (based on thermodynamics and processing conditions), it was determined that the thickness of an X70 pipe had no particular effect on nanoscale precipitation. The NbC precipitation model in its current state simplifies many of the real processing conditions. Some amelioration could be achieved such as the implementation of a phase transformation model.

# Chapter 8

# Conclusions and future work

The purpose of this work was to apply matrix dissolution techniques on different steels in order to collect information regarding their precipitates. The goal was also to modify pre-existing precipitation kinetics models to take into account the processing conditions. Together these results should aid in understanding how different parameters such as the thickness of the pipe or its chemistry can affect precipitation and properties.

First of all, both the experimental and computational improvements brought by this work will be summarized, followed by the conclusions regarding the effect of wall thickness and chemistry on precipitation. Finally some recommendations and future work will be suggested.

## 8.1 Experimental and computational improvements

The present work improved two different experimental procedures as detailed in Chapter 3, and introduced two other computational techniques in Chapters 4 and 5:

1. Modification of Lu's [2] experimental set-up: $N_2$ was injected directly into the acid solution, in order to avoid the formation of amorphous $SiO_2$. $SiO_2$ was an issue for further SEM and QXRD analysis.

2. Particle suspension analysis: In order to quantify the particle size distribution of nano-sized precipitates and to isolate larger precipitates, an ethanol solution containing the

precipitates in suspension was deposited onto carbon tape for SEM analysis.

3. Rietveld refinement of X70 XRD patterns: On closer examination of the X70 precipitate diffraction peaks, it was realized that the peaks could be deconvoluted into many peaks. The deconvolution allowed for the determination of the composition and volume fraction of the different phases.

4. A new precipitation model was introduced and developed in this research work. Based on the Lagrange 'Multipreci' approach, this model takes into account the processing conditions encountered in TMCP laminar cooling, i.e., finish rolling temperature, cooling rate and coiling temperature. It was shown that experimental and simulation results were in good agreement for the two X70 steels studied, and for other previously studied X80 steels.

## 8.2 Effects of wall thickness and composition

Based on the results stated in Chapters 5 and 6 and the discussion presented in Chapter 7, the following conclusions can be made:

1. L80, ML80 and T95 steels:
   (a) There were several types of precipitates:
      i. TiN-rich and TiMoN-rich for L80 and T95 steels.
      ii. $Mo_2C$-rich for ML80 steel.
   (b) Cr is not one of the main constituents of the extracted precipitates.
   (c) Cr and Mo may be present in (Fe,Cr,Mo)C phases, which are unstable in HCl solutions.

2. X70 and TWX70 steels:
   (a) The same types of precipitates (TiN-rich, NbC-rich and NbMoC-rich) were detected.
   (b) The thickness of the steel appears to affect microscale precipitation.

(c) The thickness of the steel does not seem to affect nanoscale precipitation.

3. NbC precipitation in TMCP X70 steels during laminar cooling:

   (a) There was good agreement between the preliminary results and experimental results, despite the assumptions made.

   (b) Once improved, the model may provide a way to estimate the amount of Nb and C that is left in the steel when it enters the runout table.

## 8.3 Recommendations and future work

### 8.3.1 Improvements to the model

As stated in Chapter 7, the model's assumptions are still too restrictive and simplistic. One idea is to add Mo as a possible constituent of nanosized precipitates. The current version of the model only allows for stoichiometric NbC precipitates. An updated version could allow precipitates to be of the form $Nb_xMo_{1-x}C$. A second idea is to consider phase transformation during laminar cooling. In the current version, the matrix is considered to be only ferrite. However, it is known that austenite is still the major phase when the steel enters the runout table. Implementing a phase transformation model as developed in [48] could improve the NbC precipitation model.

### 8.3.2 Validation of the model

Further investigations are needed to validate the new model of NbC precipitation during laminar cooling presented in this work. One idea is to do differential scanning calorimetry (DSC) analysis of steels with different Nb and C contents at different annealing temperatures. Different cooling rates could be used to simulate laminar cooling on the runout table. After each DSC run, a matrix dissolution technique could be used to collect the precipitates. A similar analysis as the one presented in this work could be done and the results compared with the simulations. A second idea is to utilize some samples at different stages of TMCP (e.g., just after finish

rolling, just before the runout table and just before coiling), quench them and analyze their precipitates. Such analysis would provide insight on the precipitation sequence that occurs during the last stage of TMCP.

### 8.3.3 Site specific dissolution

In this work, the location of each sample was not a parameter. Each sample undergoing dissolution was a piece of pipe, from the inner wall to the outside wall. It may be of interest to analyze the precipitates at precise depths in the pipe, i.e., close to the surface, close to the centerline and quarter distance from the surface. Because the cooling rates are different in those regions, it is fair to assume that precipitation could be different. Taking samples at different location and stage of processing allows for statistical analyses.

### 8.3.4 Determination of the role of Cr and Mo in precipitation

It is known that Cr can improve the corrosion resistance of steels. It is also known that Cr and Mo precipitate into (Fe,Cr,Mo)C phases in quenched and tempered steels. Unfortunately, HCl dissolution does not allow for the collection of these types of precipitates. It may be relevant to find a different dissolution technique (such as a halogen-based solution) that enables collection of these precipitates. It may then be possible to determine the effect of composition on the shape, size, composition and volume fraction of iron carbides. It could also be interesting to study more deeply the effect of Cr and Mo by analyzing a whole range (more than three) of compositions from a Cr-free steel or Mo-free steel to a high-Cr steel (such as T95 steel) or a high-Mo steel (such as ML80 steel).

# Bibliography

[1] T. Gladman. *The Physical Metallurgy of Microalloyed Steels*. London, UK: The Institute of Materials, 1997.

[2] Junfang Lu. "Quantitative Microstructural Characterization of Microalloyed Steels". PhD thesis. University of Alberta, 2009.

[3] J. Lu, J.B. Wiskel, O. Omotoso, H. Henein, and D.G. Ivey. "Matrix Dissolution Techniques Applied to Extract and Quantify Precipitates from a Microalloyed Steel". In: *Metallurgical and Materials Transactions A* 42A (July 2011), pp. 1767–1784.

[4] L.E. Collins. "Processing of Nb-containing steels by Steckel mill rolling". In: *Niobium Science and Technology: Proceedings of the International Symposium Niobium 2001* (2001), pp. 527–542.

[5] D. Bai, M.A. Cooke, J. Asante, and J. Dorricott. *Process for making high strength micro-alloy steels*. US Patent 6,682,613. 2004.

[6] M. Kutz. *Handbook of Materials Selection*. New York, USA: John Wiley and Sons Inc., 2002, p. 44.

[7] F. Liu, J. Wang, Y. Liu, R.D.K. Misra, and C. Liu. "Effects of Nb and V on Microstructural Evolution, Precipitation Behavior and Tensile Properties in Hot-rolled Mo-bearing Steel". In: *Journal of Iron and Steel Research International* 23.6 (June 2016), pp. 559–565.

[8] M.G. Akben, B. Bacroix, and J.J. Jonas. "Effect of V and Mo addition on high temperature recovery, recrystallization and precipitation behavior of Nb-based steels". In: *Acta Metallurgica* 31.5 (May 1983), pp. 161–174.

[9] H.G. Lambers, S. Tschumak, H.J. Maier, and D. Canadinc. "Role of Austenitization and Pre-Deformation on the Kinetics of the Isothermal Bainitic Transformation". In: *Metallurgical and Materials Transactions A* 40.6 (Apr. 2009), pp. –.

[10] G. Krauss. *Steels: Processing, Structure, and Performance (Chapter 16)*. Materials Park, OH: ASM International, 2015, pp. 335–369.

[11] G. Krauss. *Steels: Processing, Structure, and Performance (Chapter 17)*. Materials Park, OH: ASM International, 2015, pp. 373–379.

[12] G. Krauss. *Steels: Processing, Structure, and Performance (Chapter 17)*. Materials Park, OH: ASM International, 2015, pp. 380–394.

[13] S. Dépinoy, C. Toffolon-Masclet, S. Urvoy, J. Roubaud, and B. Marini. "Carbide precipitation in 2.25 Cr-1 Mo bainitic steel : effect of heating and isothermal tempering conditions". In: *Metallurgical and Materials Transactions A* 48A (May 2017), pp. 2164–2178.

[14] G.R. Speich and W.C. Leslie. "Role of Austenitization and Pre-Deformation on the Kinetics of the Isothermal Bainitic Transformation". In: *Metallurgical and Materials Transactions A* 40.6 (Apr. 2009), pp. –.

[15] *International Center for Diffraction Data (ICDD)*.

[16] J. Jung, E. Shin, and Y. Lee. "Separate Evaluation of the Kinetics of Carbide Precipitation Occurring at the Interface of Preexisting Particles and Within the Austenitic Matrix in a Microalloyed Steel". In: *Metallurgical and Materials Transactions A* 48A (Jan. 2017), pp. 76–85.

[17] Y.J. Lee, P.R. Miller, and B.C. Muddle. "Identification of Carbonitride Precipitates in a lwt.Cr-0.5wt.Mo Steel using Analytical Electron Microscopy". In: *Materials Science and Engineering* A131 (1991), pp. 123–132.

[18] T.P. Hou and K.M. Wu. "Alloy carbide precipitation in tempered 2.25 Cr-Mo under high magnetic fiels". In: *Acta Materialia* 61 (Jan. 2013), pp. 2016–2024.

[19] C.A. Knepfler, K.T. Faber, J. Weertman, G.B. Olson, C.R. Hubbardb, O.B. Cavinb, and N. Packenb. "High temperature stability and thermal expansion behavior of molybdenum-chromium M2C carbides". In: *Journal of Alloys and Compounds* 248 (June 1996), pp. 139–142.

[20] B.D. Ozsdolay, K. Balasubramanian, and D. Gall. "Cation and anion vacancies in cubic molybdenum nitride". In: *Journal of Alloys and Compounds* 705 (Feb. 2017), pp. 631–637.

[21] G. Kaye. "Face-centred Cubic Molybdenum Monocarbide". In: *Nature* 195 (Sept. 1962), pp. 1195–1196.

[22] J. Kunze. "Solubility product og TiN in $\gamma$-iron". In: *Metal Science* 16.4 (1982), pp. 217–218.

[23] E.J. Pavlina, J.G. Speer, and C.J. Van Tyne. "Equilibrium solubility products of molybdenum carbide and tungsten carbide in iron". In: *Scripta Materialia* 66 (2012), pp. 243–246.

[24] A.J. Ardell. "Precipitation hardening". In: *Metallurgical and Materials Transactions A* 16A (1985), pp. 2131–2165.

[25] J. Lu, O. Omotoso, J.B. Wiskel, D.G. Ivey, and H. Henein. "Strengthening Mechanisms and Their Relative Contributions to the Yield Strength of Microalloyed Steels". In: *Metallurgical and Materials Transactions A* 43A (Sept. 2012), pp. 3043–3061.

[26] A. M. Elwazri, R. Varano, F. Siciliano, D. Bai, and S. Yue. "Characterisation of precipitation of niobium carbide using carbon extraction replicas and thin foils by FESEM". In: *Materials Science and Technology* 22.5 (July 2006), pp. 537–541.

[27] M. Kapoor, R. O'Malley, and G.B. Thompson. "Atom Probe Tomography Study of Multi-microalloyed Carbide and Carbo-Nitride Precipitates and the Precipitation Sequence in Nb-Ti HSLA Steels". In: *Metallurgical and Materials Transactions A* 47A (May 2016), pp. 1984–1995.

[28] A.J. Breen, .Y. Xie, M.P. Moody, B. Gault, H. Yen, C.C. Wong, J.M. Cairney, and S.P. Ringer. "Resolving the Morphology of Niobium Carbonitride Nano-Precipitates in Steel Using Atom Probe Tomography". In: *Microscopy and Microanalysis* 20 (June 2014), pp. 1100–1110.

[29] J.Barry Wiskel, Douglas G. Ivey, and H. Henein. "The Effects of Finish Rolling Temperature and Cooling Interrupt Conditions on Precipitation in Microalloyed Steels Using Small Angle Neutron Scattering". In: *Metallurgical and Materials Transactions A* 39B (Feb. 2008), pp. 116–124.

[30] P. Staron, B. Jamnig, H. Leitner, R. Ebner, and H. Clemens. "Small-angle neutron scattering analysis of the precipitation behavior in a maraging steel". In: *Journal of Applied Crystallography* 36 (2003), pp. 415–419.

[31] F. Perrard, A. Deschamps, and P. Maugis. "Modelling the precipitation of NbC on dislocations in ferrite". In: *Acta Materialia* 55.4 (2007), pp. 1255–1266.

[32] A.L. Rivas, E. Vidal, D.K. Matlock, and J.G. Speer. "Electrochemical extraction of microalloy carbides in Nb-steel". In: *Revista de Metalurgia* 44.5 (Sept. 2016), pp. 447–456.

[33] Y. Ishiguro, T. Murayama, A. Chino, K. Sato, Y. Shima, A. Kido, and M. Morita. "A precise quantitative analysis of precipitates in Ti-bearing interstitial-free steel". In: *39th Mechanical Working and steel Processing Conference, Iron and Steel Society of AIME* (1998), pp. 255–264.

[34] *Standard Test Method for Acid-Insoluble Content of Copper and Iron Powders*. Pennsylvania, US, 2015.

[35] T. Mori and K. Fujita. "Behaviour of niobium carbides and nitrides in steel". In: *Journal of the Iron and Steel Institute of Japan* 50 (1964), pp. 911–917.

[36] S. Kanazawa, A. Nakashima, K. Okamoto, K. Tanabe, and S. Nakazawa. "On the behavior of precipitates in the Nb-Mo heat treated high strength steel having 80 kg/mm2 tensile strength". In: *Transactions of the Japan Institute of Metals* 8.2 (1967), pp. 113–119.

[37] V. Klimenko. "The stregth of chromium carbide hard alloys". In: *Poroshkovaya Metallurgiya* 23.5 (1964), pp. 52–56.

[38] H.M. Rietveld. "Line profiles of neutron powder-diffraction peaks for structure refinement". In: *Acta Crystallographica* 22 (1967), pp. 151–152.

[39] H.M. Rietveld. "A profile refinement method for nuclear and magnetic structures". In: *Journal of Applied Crystallography* 2 (1969), pp. 65–71.

[40] N.C. Popa and D. Balzar. "An analytical approximation for a size-broadened profile given by the lognormal and gamma distributions". In: *Journal of Applied Crystallography* 35 (2002), pp. 338–346.

[41] D. Balzar, N. Audebrand, M. R. Daymond, A. Fitch, A. Hewat, J. I. Langford, A. Le Bail, D. Louer, O. Masson, C. N. McCowan, N. C. Popa, P. W. Stephensj, and B. H. Tobykr. "Size–strain line-broadening analysis of the ceria round-robin sample". In: *Journal of Applied Crystallography* 37 (Feb. 2004), pp. 911–924.

[42] J.B. Wiskel, J. Lu, Oladipo Omotoso, D.G. Ivey, and H. Henein. "Characterisation of precipitation of niobium carbide using carbon extraction replicas and thin foils by FESEM". In: *Metals* 90.6 (Apr. 2016), pp. 1–13.

[43] Dominique Gendt. "Cinétique de précipitation du carbure de niobium dans la ferrite". PhD thesis. CEA Saclay - Usinor, 2001.

[44] M. Perez, M. Dumont, and D. Acevedo-Reyes. "Implementation of classical nucleation and growth theories for precipitation". In: *Acta Materialia* 56 (Mar. 2008), pp. 2119–2132.

[45] R. Wagner and R. Kampmann. *Materials Science and Technology : a comprehensive treatment*. Vol. 5. 1991.

[46] P. Maugis and M. Gounè. "Kinetics of vanadium carbonitride precipitation in steel: A computer model". In: *Arcelor Research* 53 (May 2005), pp. 3359–3367.

[47] N. Fujita, H.K.D.H Bhadeshia, and K. Kikuchi. "Modeling M6C Precipitation in Niobium-Alloyed Ferritic Stainless Steel". In: *Metallurgical and Materials Transactions A* 33A (Nov. 2002), pp. 3339–3347.

[48] A. Van der Laan. "The Effect Of Runout Table Cooling On The Microstructure Of Thick Walled X70 Skelp". MA thesis. University of Alberta, 2017.

[49] *Standard Test Methods for Determining Average Grain Size Using Semiautomatic and Automatic Image Analysis*. Pennsylvania, US, 2015.

[50] B.H. Toby. "R factors in Rietveld analysis: How good is good enough?" In: *Powder Diffraction* 21 (Mar. 2006), pp. 67–70.

[51] R.J. Hill and C.J. Howard. "Quantitative phase analysis from neutron powder diffraction data using the Rietveld method". In: *Journal of Applied Crystallography* 20 (1987), pp. 467–474.

[52] P. Zhao, X. Liu, A.G. De La Torre, L. Lu, and K. Sobolevd. "Assessment of the quantitative accuracy of Rietveld/XRD analysis of crystalline and amorphous phases in fly ash". In: *Analytical Methods* 9 (Feb. 2017), pp. 2415–2424.

[53] R. Kampmann and R. Wagner. *Decomposition of alloys: the early stages. (Chapter Kinetics of precipitation in metastable binary alloys).* Pergamon Press., 1984, pp. 91–103.

[54] K. Russell. "Nucleation in Solids : the Induction and Steady State Effects." In: *Advanced in Colloid and Interface Science* 13 (1980), pp. 205–218.

[55] Y. Zeldovich. "On the theory of new phase formation: cavitation". In: *Acta Physicochim USSR* 18 (1943), pp. 1–22.

[56] K. Russell. *Phase transformations (Chapter Nucleation in solids).* American Society for Metals, 1968, pp. 219–68.

[57] C. Zener. "Theory of growth of spherical precipitates from solid solution". In: *Journal of Applied Physics* 20 (1949), pp. 950–953.

[58] *PDF 00-038-1420 and PDF 98-000-0339*.

# Appendix A

# Modeling of NbC precipitation: python implementation

```
# MAIN CODE MULTIPRECI ########

print('Precipitation of nano-NbC in the Fe-Nb-C system')
print('by Corentin Chatelier - University of Alberta')

import matplotlib

from matplotlib.pylab import axis, tight_layout, subplots, scatter, plot,
    subplot, semilogx, xlabel, ylabel, title, legend,  suptitle, grid, clf,
     cla #, axes, subplots_adjust,gcf

from math import  log,  pi
from numpy import subtract, multiply, array, sqrt, exp, expm1 #, seterr,
    finfo

# Data import ########
def lecture_data(file) :
    try:
        data = open(file,'r')
        full_data = data.read().split()[:24]

        dt = float(full_data[1])
        t_end = float(full_data[3])
        t_cool = float(full_data[5])
        t_stop = float(full_data[7])

        T_frt = float(full_data[9])
        T_ct = float(full_data[11])

        gammma = float(full_data[13])
        rho = float(full_data[15])

        A = float(full_data[17])
```

```
31          B = float(full_data[19])
32
33          w0_Nb = float(full_data[21])
34          w0_C = float(full_data[23])
35
36          return dt, t_end, t_cool, t_stop, T_frt, T_ct, gammma, rho, A, B,
                w0_Nb, w0_C
37
38      except FileNotFoundError:
39          print('File not found')
40
41      except IOError:
42          print('File error')
43
44  def multipreci(file_data):
45      #file_data = input("Data file name (.txt) :  ")
46      dt, t_end, t_cool, t_stop, T_frt, T_ct, gammma, rho, A, B, w0_Nb, w0_C
            = lecture_data(file_data + '.txt')
47
48      # Discretization ########
49
50      print('Time Discretization ...')
51
52      nt = int(round(t_end/dt))
53      time = [i*dt for i in range(nt)]
54
55      slope = (T_ct - T_frt)/(t_stop - t_cool)
56
57      print('Cooling Rate (K/s) = ' + str(slope))
58
59      T = []
60
61      for i in range(len(time)):
62          if time[i] <= t_cool :
63              T.append(T_frt+273.15)
64          elif t_cool < time[i] <= t_stop:
65              T.append(dt*slope+T[i-1])
66          else:
67              T.append(T_ct+273.15)
68      T = array(T)
69
70      # Data General ########
71      kB = 1.3806e-23 # Boltzmann constant, in J.K-1
72      Na = 6.023e23 # Avogadro, in mol-1
73
74      aFe = 2.866e-10  # lattice parameter Fe alpha
75      aNbC = 4.47e-10  # lattice parameter NbC
76
77      D0_Nb = 5e-3  # diffusion pre-coefficient in m2/s1
78      Q_Nb = 2.61/(1.04*1e-5)  #  activation energy in ferrite, J/mol
79
80      D0_C = 2e-6  # diffusion pre-coefficient in m2/s
81      Q_C = 0.88/(1.04*1e-5)  # activation energy in ferrite, J/mol
```

```
82
83      v_NbC = (aNbC**3)/4  # atomic volume, m3.at-1
84      v_Fe = (aFe**3)/2  # atomic volume, m3.at-1
85
86      # Composition ########
87      AFe = 55.845 # atomic mass Fe
88      AC = 12.0107 # atomic mass C
89      ANb = 92.90638 # atomic mass Nb
90
91      X0_Nb = (1.0/100.0)*(AFe/ANb)*w0_Nb
92      X0_C = (1.0/100.0)*(AFe/AC)*w0_C
93
94      # MAIN CODE ########
95      print('Variables initialization ...')
96
97      n_Fe_ini = (1-X0_C-X0_Nb)/(v_Fe*(1-X0_C)) # considering Nb
            substitutionnal in Fe-matrix
98      n_Nb_ini = (X0_Nb)/(v_Fe*(1-X0_C)) # considering Nb substitutionnal in
             Fe-matrix
99      n_C_ini = (X0_C)/(v_Fe*(1-X0_C)) # considering C interstitial in the
            Fe-Nb-matrix
100
101     n_Nb_temp = n_Nb_ini # going to change
102     n_C_temp = n_C_ini # going to change
103
104     Xss_Nb = [0 for col in range(nt)] #XNb in solid solution
105     Xss_C = [0 for col in range(nt)] #XC in ss
106     Xss_Nb[0] = X0_Nb
107     Xss_C[0] = X0_C
108
109     Xpp_Nb = 0.5 # in NbC, 0.5 Nb, 0.5 C // 1 according to [Maugis 2005]
110
111     nmax_classes = nt # arbitrary
112
113     Nclasses = 0 # nb classes of precipitate, en size, initially no ppt
114
115     Ngerm = [0 for col in range(nmax_classes)] # nb of nucleus at each
            timestep, matrix nmax_classes * time
116     N = [0 for col in range(nt)] # total number of nuclei
117     N_rate = [0 for col in range(nt)] # nucleation rate over the time
118
119     R = [0 for col in range(nmax_classes)] # radius time i
120     R1 = [0 for col in range(nmax_classes)] # radius time i+1
121     V = [0 for col in range(nmax_classes)] # volume
122
123     f_v = [0 for col in range(nt)] # volume fraction
124
125     Rstar = [0 for col in range(nt)] # critical radius
126     Rmean = [0 for col in range(nt)]
127
128     Ks = [0 for col in range(nt)]
129     D_Nb = [0 for col in range(nt)]
130     D_C = [0 for col in range(nt)]
```

```
131     R0 = [0 for col in range(nt)]
132
133     # Initialisation ########
134     print('Simulation ...')
135
136     N0 = 2.0/(aFe**3.0) # germination site density at.m-3
137
138     # Iterations i for the time, j for the classes of precipitates
139     for i in range(nt-1):
140         Nclasses += 1 # adding a class
141
142         Ks[i] = exp(B - A/T[i])  # solubility product of NbC at T
143         D_Nb[i] = D0_Nb*exp(-Q_Nb/(Na*kB*T[i])) # diffusion coefficient in
                ferrite, m2/s
144         D_C[i] = D0_C*exp(-Q_C/(Na*kB*T[i]))  # diffusion coefficient in
                ferrite, m2/s
145         R0[i] = 2.0*gammma*v_NbC/(kB*T[i])
146         Delta_G0 = (4.0/3.0)*pi*R0[i]**2.0*gammma
147
148         Xss_Nb[i] = n_Nb_temp / (n_Nb_temp + n_C_temp + n_Fe_ini) #
                calculating the new ss
149         Xss_C[i] = n_C_temp / (n_Nb_temp + n_C_temp + n_Fe_ini)
150
151         Rstar[i] = R0[i]/log(Xss_C[i]*Xss_Nb[i]/Ks[i]) # calculating the
                capilarity radius
152         Rprime = Rstar[i] + (1.0/2.0)*sqrt(kB*T[i]/(pi*gammma)) #
                calculating the critical radius
153         Z = (v_NbC/(2.0*pi*Rstar[i]**2.0))*sqrt(gammma/(kB*T[i])) #
                zeldovitch factor
154         beta = 4.0*pi*Rstar[i]**2*D_Nb[i]*Xss_Nb[i]/aFe**4
155         tau = 1.0/(2.0*beta*Z**2.0) # time constant
156
157         Delta_Gstar = Delta_G0/((log(Xss_C[i]*Xss_Nb[i]/Ks[i]))**2.0)
158         N_rate[i] = N0*Z*beta*(-expm1(-time[i]/tau))/exp(Delta_Gstar/(kB*T
                [i]))
159
160         Ngerm[i] = dt*N_rate[i] # germination equation
161         R[i] = Rprime  # initializing to Rprime
162         V[i]= Ngerm[i]*(4.0/3.0)*pi*(R[i])**3.0
163
164         n = (V[i]/v_NbC)
165         n_Nb_temp -= n
166         n_C_temp -= n
167         Vtot = 0
168         W = 0.0
169         for j in range(Nclasses):
170             R = R1
171             if R[j] != 0.0:
172                 X_Nb_interface = (1.0/2.0)*(Xss_Nb[i] - (D_C[i]/D_Nb[i])*
                        Xss_C[i] + sqrt(((D_C[i]/D_Nb[i])*Xss_C[i] - Xss_Nb[i])
                        **2.0 +4.0*Ks[i]*(D_C[i]/D_Nb[i])*exp(R0[i]/R[j])))
173 #                X_C_interface = Ks[i]*exp(R0[i]/R[j])/X_Nb_interface
174                 tempV = V[j]
```

```
175                 # MAIN CODEs
176                 if (Xss_Nb[i] - X_Nb_interface) >= 0: # id est, growth <-
                        Gibbs Thomson Effect
177                     R1[j] = R[j] + dt* (D_Nb[i]*(Xss_Nb[i] -
                            X_Nb_interface)) / (R[j]*Xpp_Nb*((v_Fe/v_NbC) -
                            X_Nb_interface)) #eq growth
178                     V[j] = Ngerm[j]*(4.0/3.0)*pi*(R1[j])**3.0
179
180                     n = ((V[j]-tempV)/v_NbC) # nb of NbC to remove from
                            the solution : n Nb and n C, they are in ppt now
181
182                     n_Nb_temp -= n # removing the atoms from the solution
183                     n_C_temp -= n # removing the atoms from the solution
184
185                 else:  # id est, dissolution <- Gibbs Thomson Effect
186                     n = V[j]/v_NbC # nb of NbC to put back in solution : n
                             Nb and n C
187
188                     n_Nb_temp += n # adding back the atoms in solution
189                     n_C_temp += n # adding back the atoms in solution
190
191                     R1[j] = 0.0 # removing the ppt
192                     Ngerm[j] = 0.0 # removing the ppt
193                     V[j] = 0.0 # removing the ppt
194
195         # Global Variables
196         N[i] = sum(Ngerm) # add all the nuclei, from each classes
197         Vtot = sum(V) # volume total de ppt
198         f_v[i] = Vtot/(Vtot + 1) # volume fraction
199
200         for j in range(Nclasses):
201             W = W + R[j]*Ngerm[j]
202         if sum(Ngerm) == 0:
203             Rmean[i] = R0[i]
204         else:
205             Rmean[i] = W / sum(Ngerm)
206
207     Rmean_final = Rmean[nt-2]
208     f_v_final = f_v[nt-2]
209     sigma_ppt = (10.8*sqrt(f_v_final)/(Rmean_final*1e6))*log(Rmean_final*1
            e6/(6.125e-4)) # US Patent 6682613 B2 2004, Bai, Cooke, Asante,
            Dorricott
210
211     wss_Nb_final = 100*Xss_Nb[nt-2]*ANb/AFe
212     wss_C_final = 100*Xss_C[nt-2]*AC/AFe
213     k_Nb = 2400 #MPa , ref Lu 2012
214     k_C = 5082 #MPa
215     sigma_ss = k_Nb*wss_Nb_final + k_C*wss_C_final
216
217     return  Rmean_final, f_v_final, sigma_ppt, sigma_ss
```

# Appendix B

# QXRD Results

## B.1 TWX70

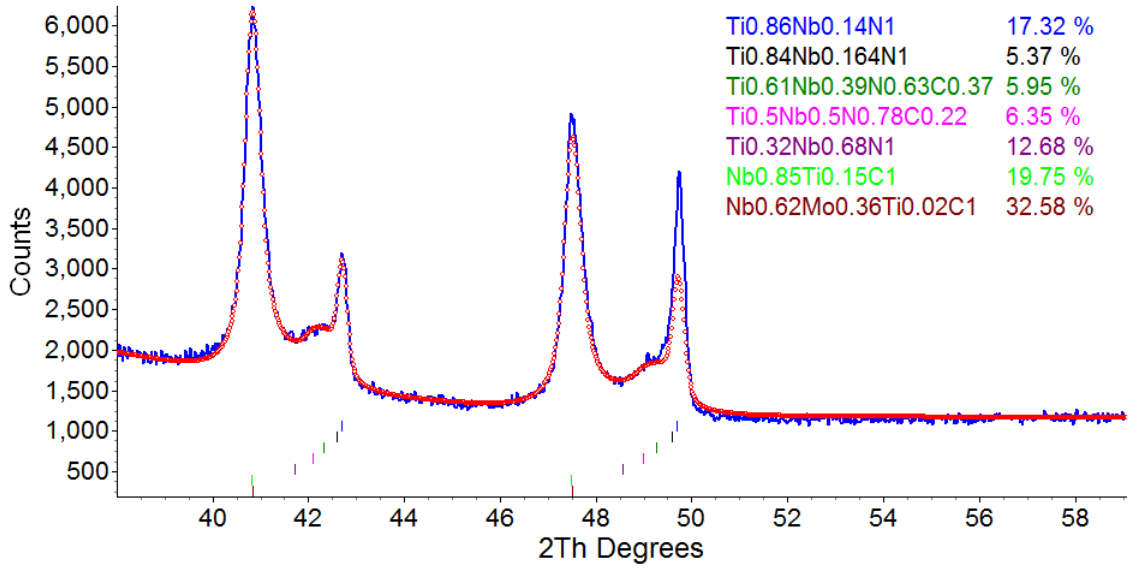


FIG. B.1 – QXRD analysis for precipitates in TWX70 steel.

## B.2 X70

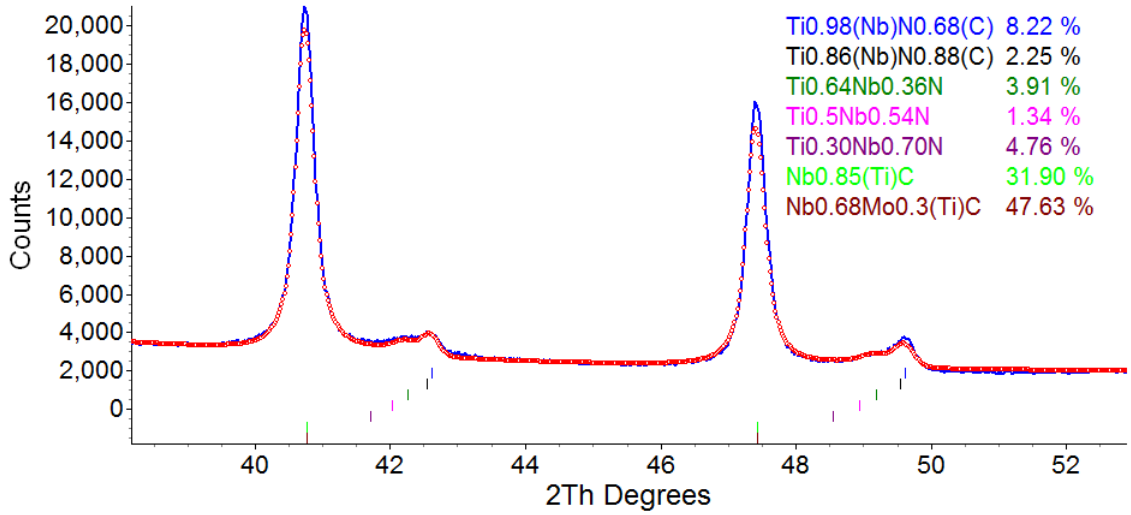


FIG. B.2 – QXRD analysis for precipitates in X70 steel.

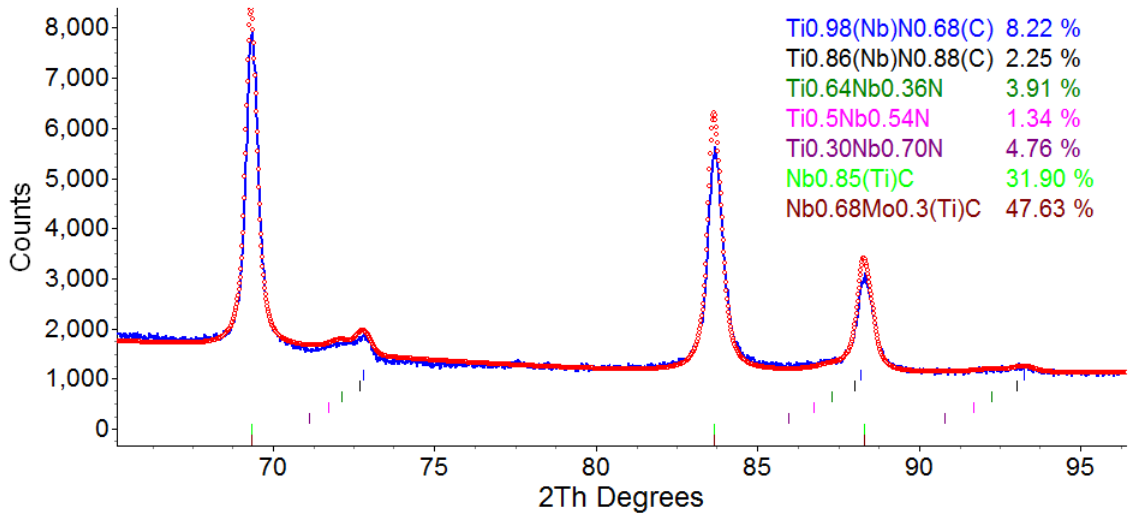


FIG. B.3 – QXRD analysis for precipitates in X70 steel.

## B.3 L80

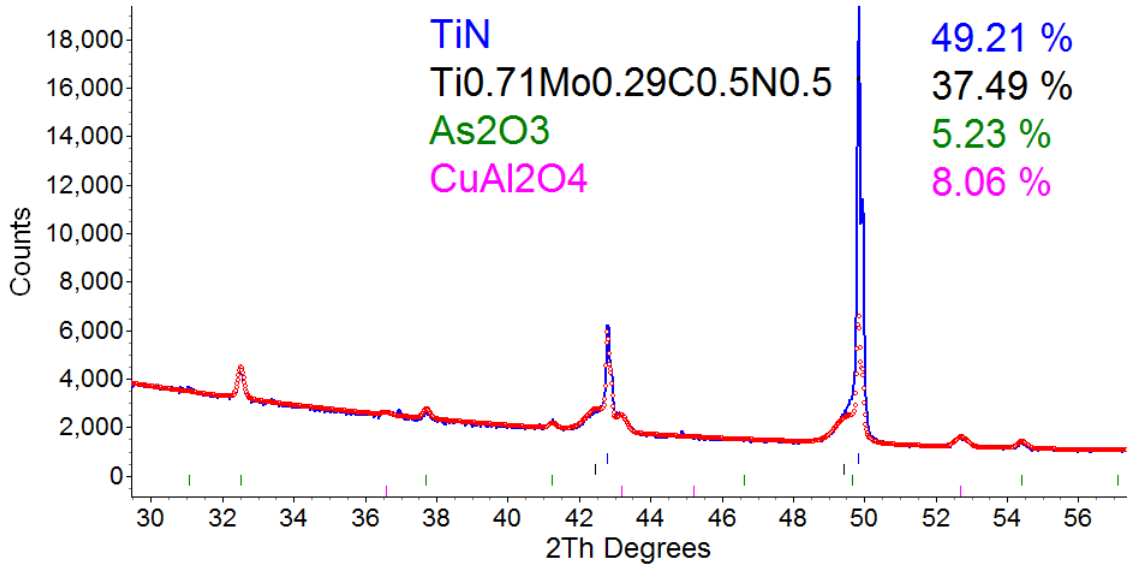


FIG. B.4 – QXRD analysis for precipitates in L80 steel.

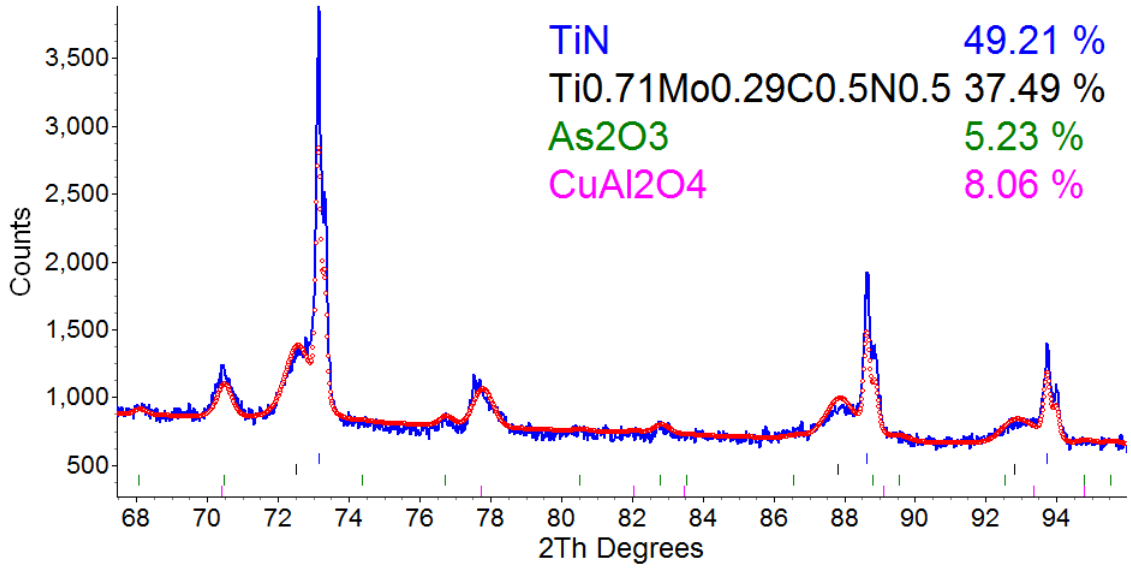


FIG. B.5 – QXRD analysis for precipitates in L80 steel.

## B.4 T95

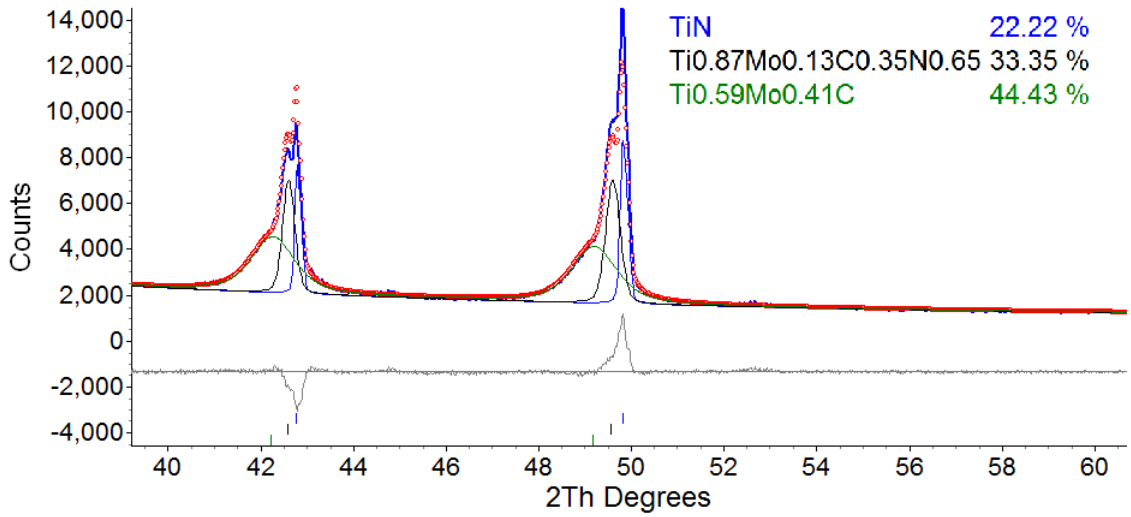


FIG. B.6 – QXRD analysis for precipitates in T95 steel.

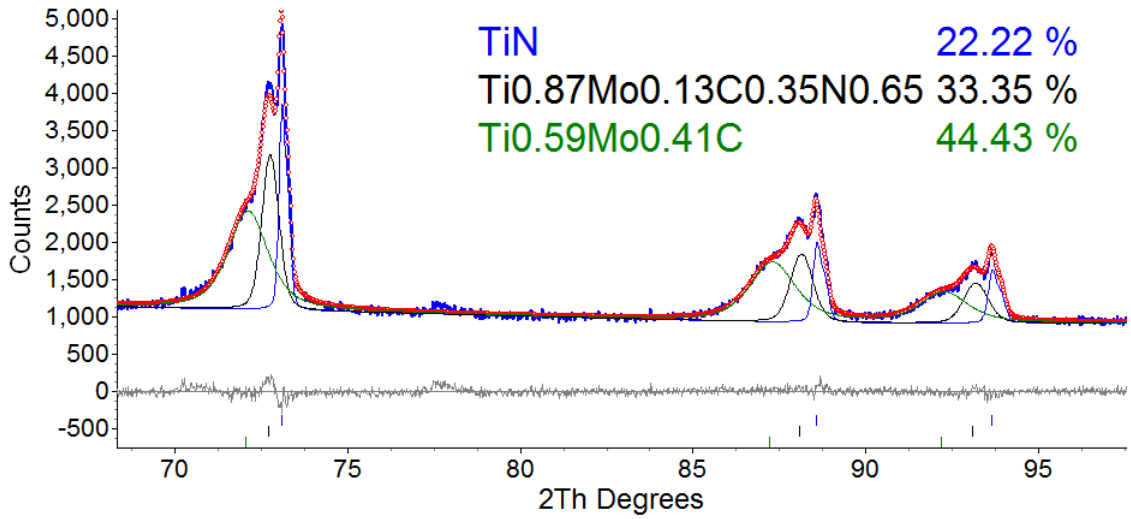


FIG. B.7 – QXRD analysis for precipitates in T95 steel.

## B.5 Mass balance calculation example

This section presents the different steps of a mass balance calculation. Assuming a precipitate $(Ti_xNb_yMo_{1-x-y})(N_zC_{1-z})$, referred as $\varphi$, its molar mass $M_\varphi$ is defined by Equation B.1.

$$M_\varphi = xM_{Ti} + yM_{Nb} + (1-x-y)M_{Mo} + zM_N + (1-z)M_C \tag{B.1}$$

where $M_i$ are the molar masses of the different elements. The amount of $\varphi$, $n_\varphi$ (in mol), in the collected powder is defined by Equation B.2.

$$n_\varphi = \frac{m_\varphi}{M_\varphi} = \frac{m_{residues} \cdot w_\varphi}{100 \cdot M_\varphi} \tag{B.2}$$

where $m_\varphi$ is the mass of phase $\varphi$, $m_{residues}$ is the mass of the collected residues and $w_\varphi$ is the relative abundance of $\varphi$ calculated by Topas. The mass of Nb in $\varphi$, $m_{Nb,\varphi}$, is defined by Equation B.3.

$$m_{Nb,\varphi} = y \cdot n_\varphi \cdot M_{Nb} \tag{B.3}$$

Assuming that i phases $\varphi_i$ were determined by QXRD analysis, the total mass of Nb $m_{Nb}$ in precipitate form is defined by Equation B.4.

$$m_{Nb} = \sum_i m_{Nb,\varphi_i} \tag{B.4}$$

The total wt% of Nb in precipitate form is then defined by Equation B.5.

$$wt\%(Nb) = \frac{100 \cdot m_{Nb}}{m_{steel}} \tag{B.5}$$

where $m_{steel}$ is the mass of the dissolved piece of steel. Table B.1 presents the data that was used to do the calculations, i.e., molar masses of Ti, Nb, Mo, C, N, mass of dissolved steel and

mass of collected residues.

TABLE B.1 – Data used for X70 mass balance calculations.

| Element | Ti | Nb | Mo | C | N | $m_{steel}$ (g) | $m_{residues}$ (g) |
|---|---|---|---|---|---|---|---|
| M (g/mol) | 47.867 | 92.906 | 95.94 | 12.01 | 14 | 48.1474 | 0.0671 |

Table B.2 presents the calculations based on the previous mathematical development (Equation B.1 to B.5). Only the Nb calculations are shown as an example. The final mass of Nb in precipitate form is 0.041 g, which gives a wt% of Nb in precipitate form of 0.0846 wt% (using Equation B.5). Based on ICP analysis, the amount of Nb in precipitate form is 0.0847 wt%. QXRD and ICP analysis are in good agreement.

TABLE B.2 – Mass balance calculations for precipitates collected from X70 steel. Only the Nb calculations are shown as an example.

| Phase | % | m (g) | Ti (x) | Nb (y) | Mo (1-x-y) | C (1-z) | N (z) | $M_{\varphi}$ (g/mol) | $n_{\varphi}$ (mol) | $m_{Nb,\varphi}$ (g) |
|---|---|---|---|---|---|---|---|---|---|---|
| TiNbCN | 8.22 | 0.0055 | 0.97 | 0.03 | 0 | 0.32 | 0.68 | 62.60 | 8.8E-05 | 2.5E-04 |
| TiNbCN | 2.25 | 0.0015 | 0.86 | 0.14 | 0 | 0.12 | 0.88 | 67.97 | 2.2E-05 | 2.9E-04 |
| TiNbN | 3.91 | 0.0026 | 0.64 | 0.36 | 0 | 0 | 1 | 78.02 | 3.4E-05 | 1.1E-03 |
| TiNbN | 1.34 | 0.0009 | 0.50 | 0.50 | 0 | 0 | 1 | 84.36 | 1.1E-05 | 4.9E-04 |
| TiNbN | 4.76 | 0.0032 | 0.30 | 0.70 | 0 | 0 | 1 | 93.37 | 3.4E-05 | 2.2E-03 |
| NbTiC | 31.9 | 0.0214 | 0.15 | 0.85 | 0 | 1 | 0 | 98.06 | 2.2E-04 | 1.7E-02 |
| NbMoTiC | 47.63 | 0.0320 | 0.02 | 0.68 | 0.30 | 1 | 0 | 104.71 | 3.1E-04 | 1.9E-02 |
| Sum | 100 | 0.0671 | - | - | - | - | - | - | - | 4.1E-02 |

# Appendix C

# SEM SE images and EDX spectra

## C.1 SEM

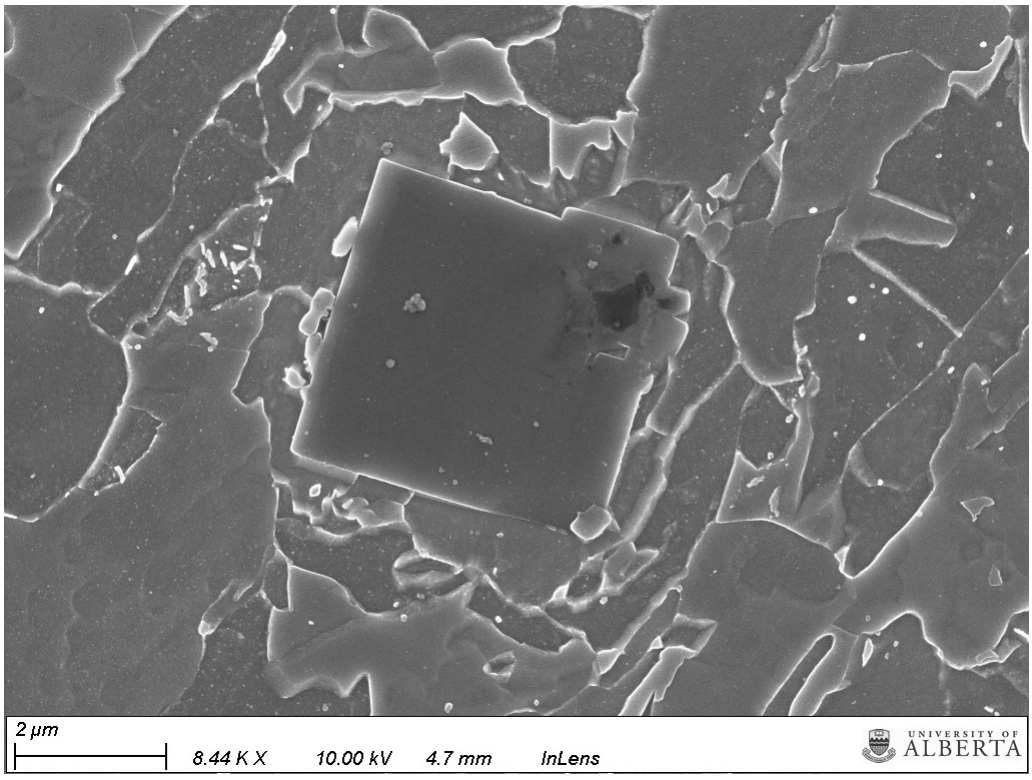


FIG. C.1 – SEM SE image of a large TiN particle in X70 steel.

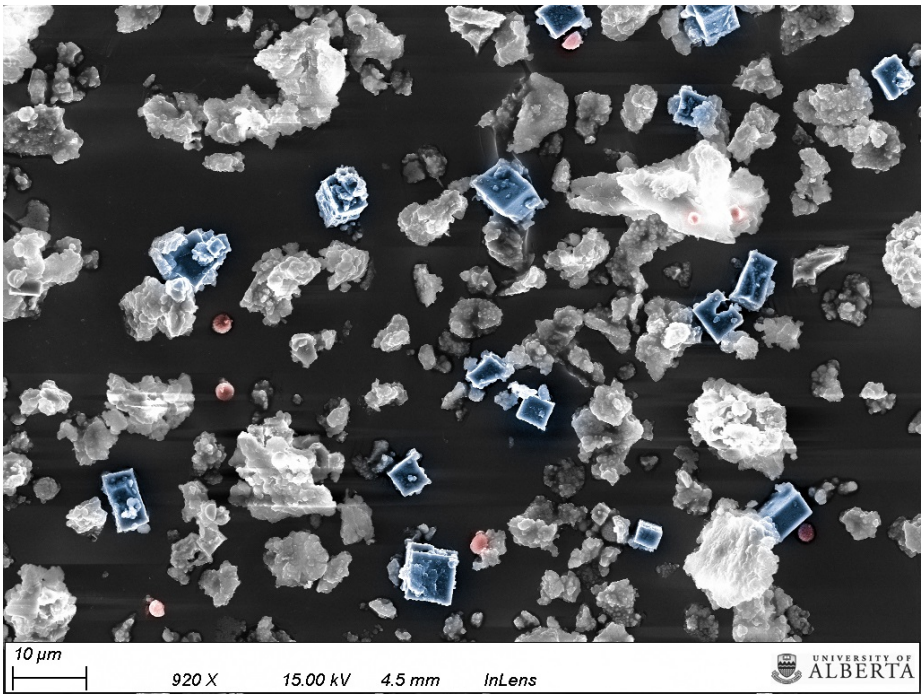


FIG. C.2 – SEM SE image of precipitates collected from L80 steel (TiN precipitates are in blue, oxides particle in are red).

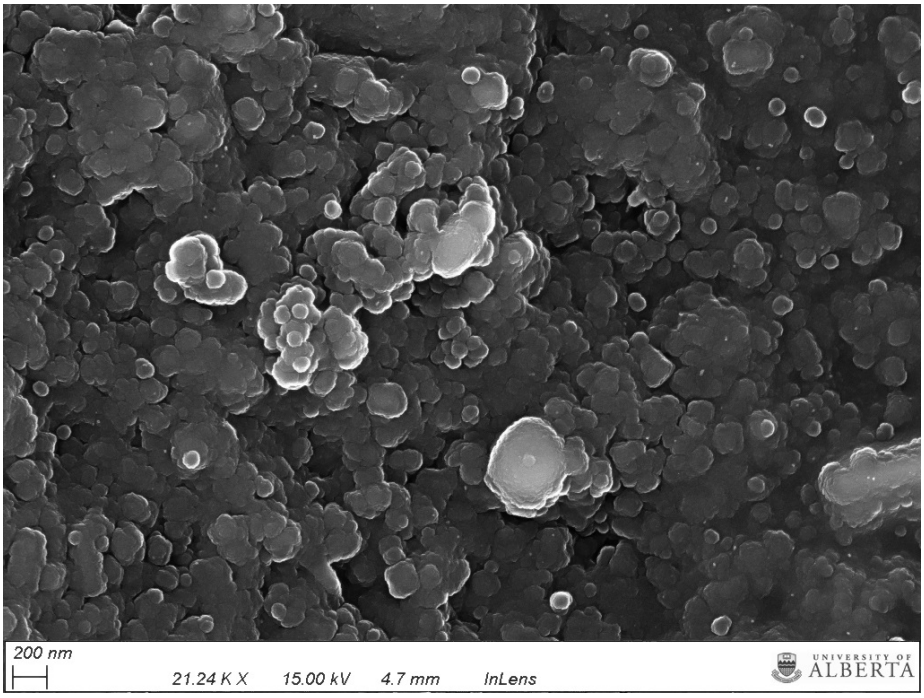


FIG. C.3 – SEM SE image of small precipitates collected from T95 steel.

## C.2 EDX

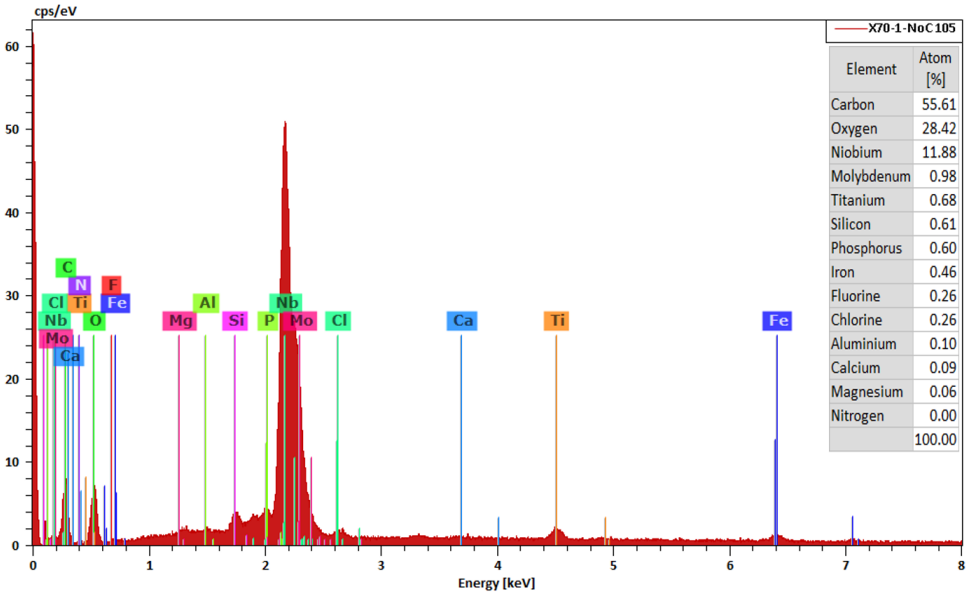


FIG. C.4 – EDX spectrum of an agglomerate of small precipitates from X70 steel.

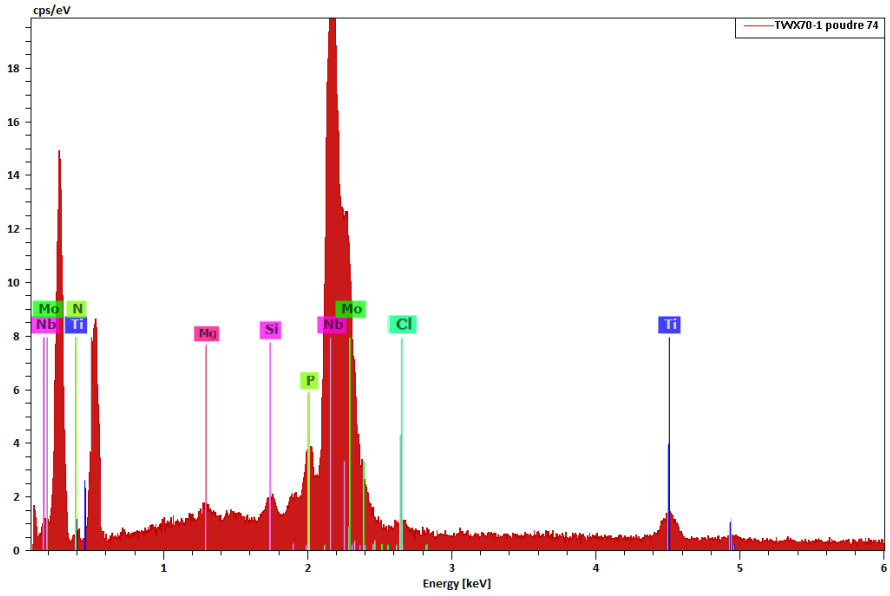


FIG. C.5 – EDX spectrum of an agglomerate of small precipitates from TWX70 steel.

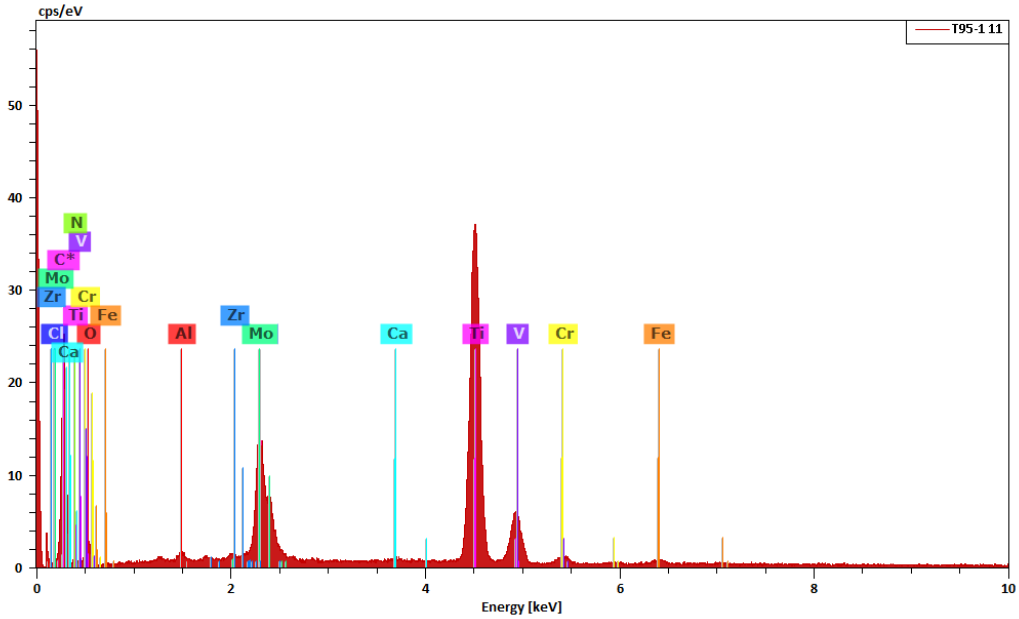


FIG. C.6 – EDX spectrum of an agglomerate of small precipitates from T95 steel.

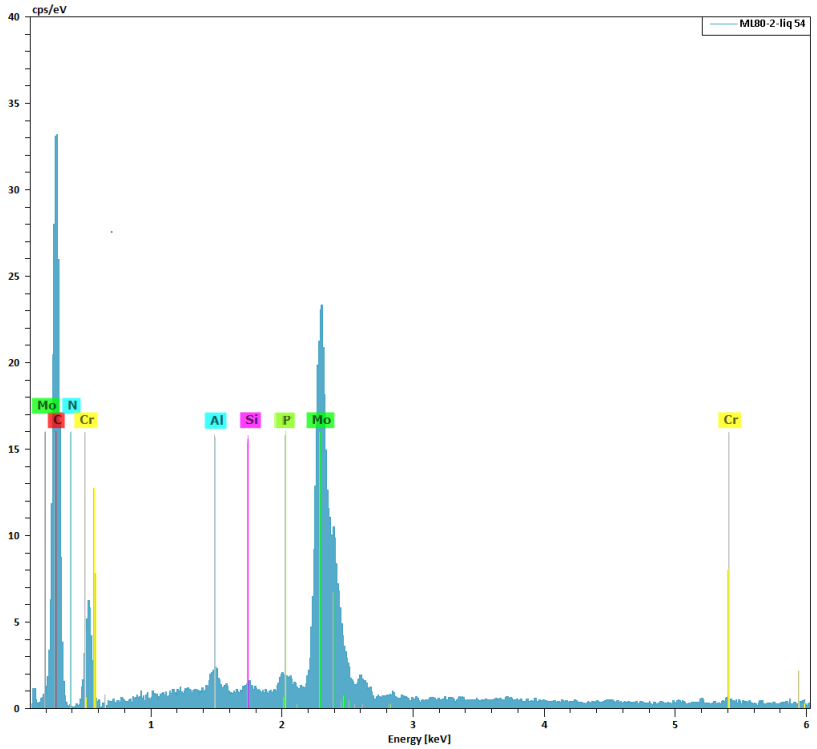


FIG. C.7 – EDX spectrum of an agglomerate of small precipitates from ML80 steel.

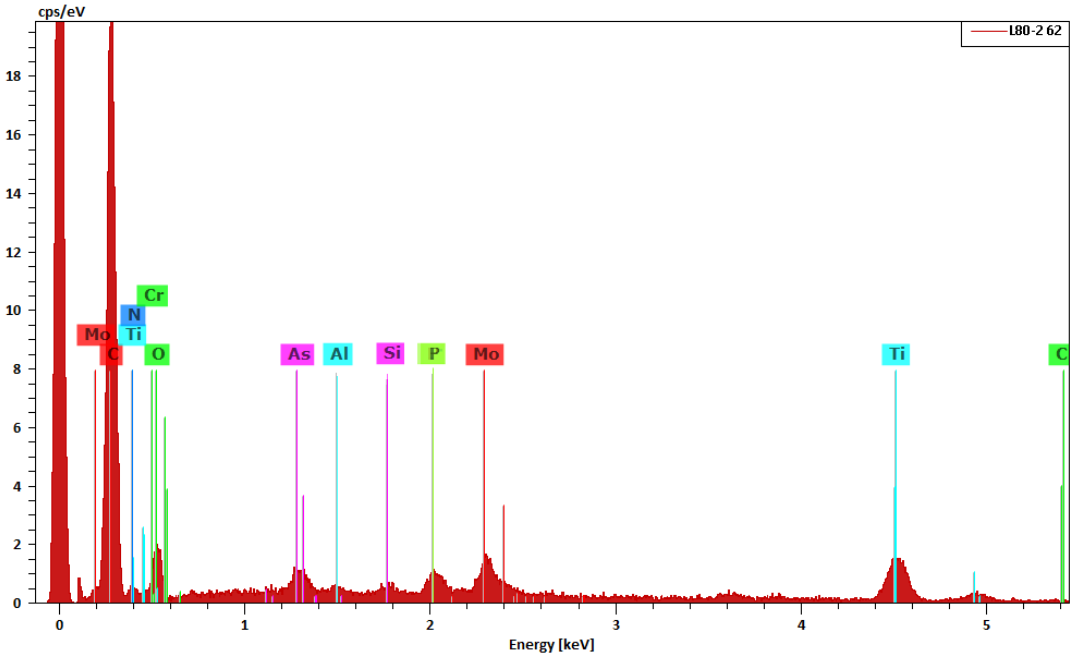


FIG. C.8 – EDX spectrum of an agglomerate of small precipitates from L80 steel showing the presence of As and O.

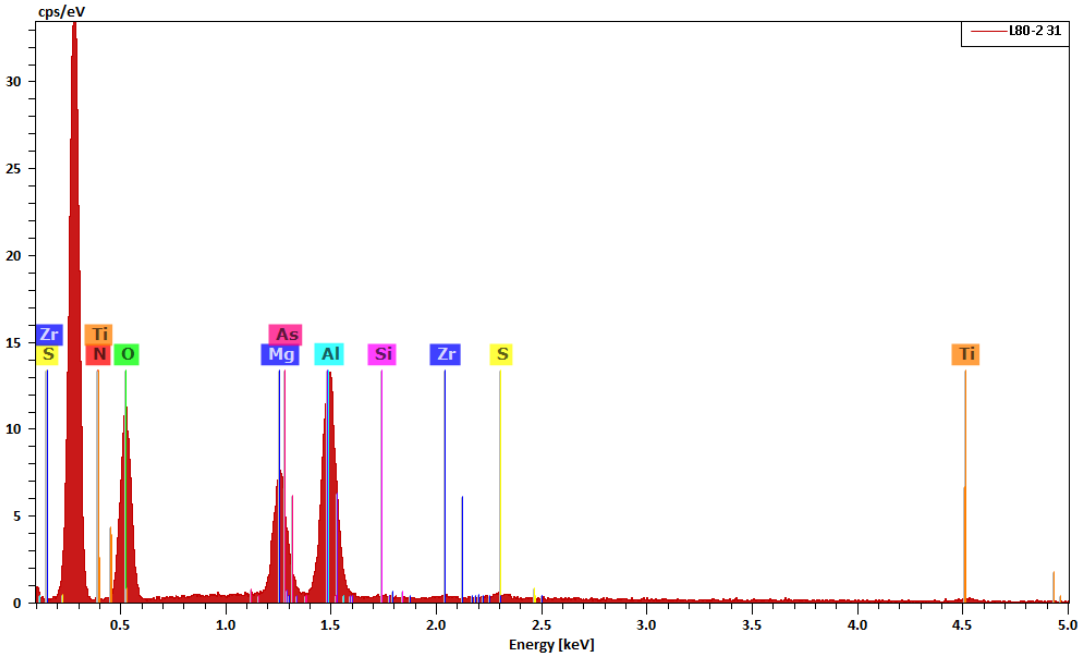


FIG. C.9 – EDX spectrum of an agglomerate of small precipitates from L80 steel showing the presence of As, Al and O.

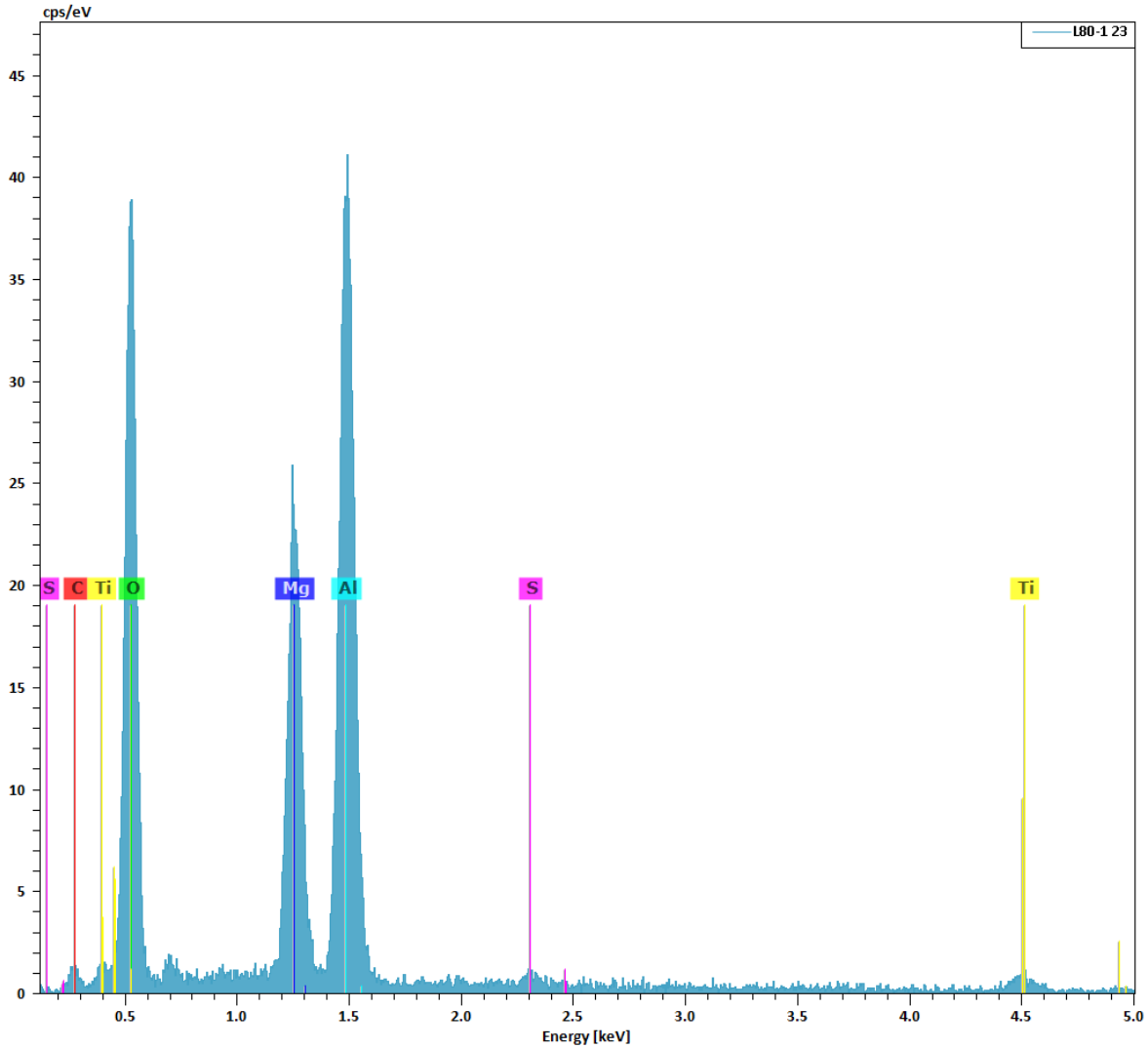


FIG. C.10 – EDX spectrum of an agglomerate of small precipitates from L80 steel showing the presence of Al, Mg and O (one unknown peak at 0.7 keV).

# Appendix D

# ThermoCalc simulations

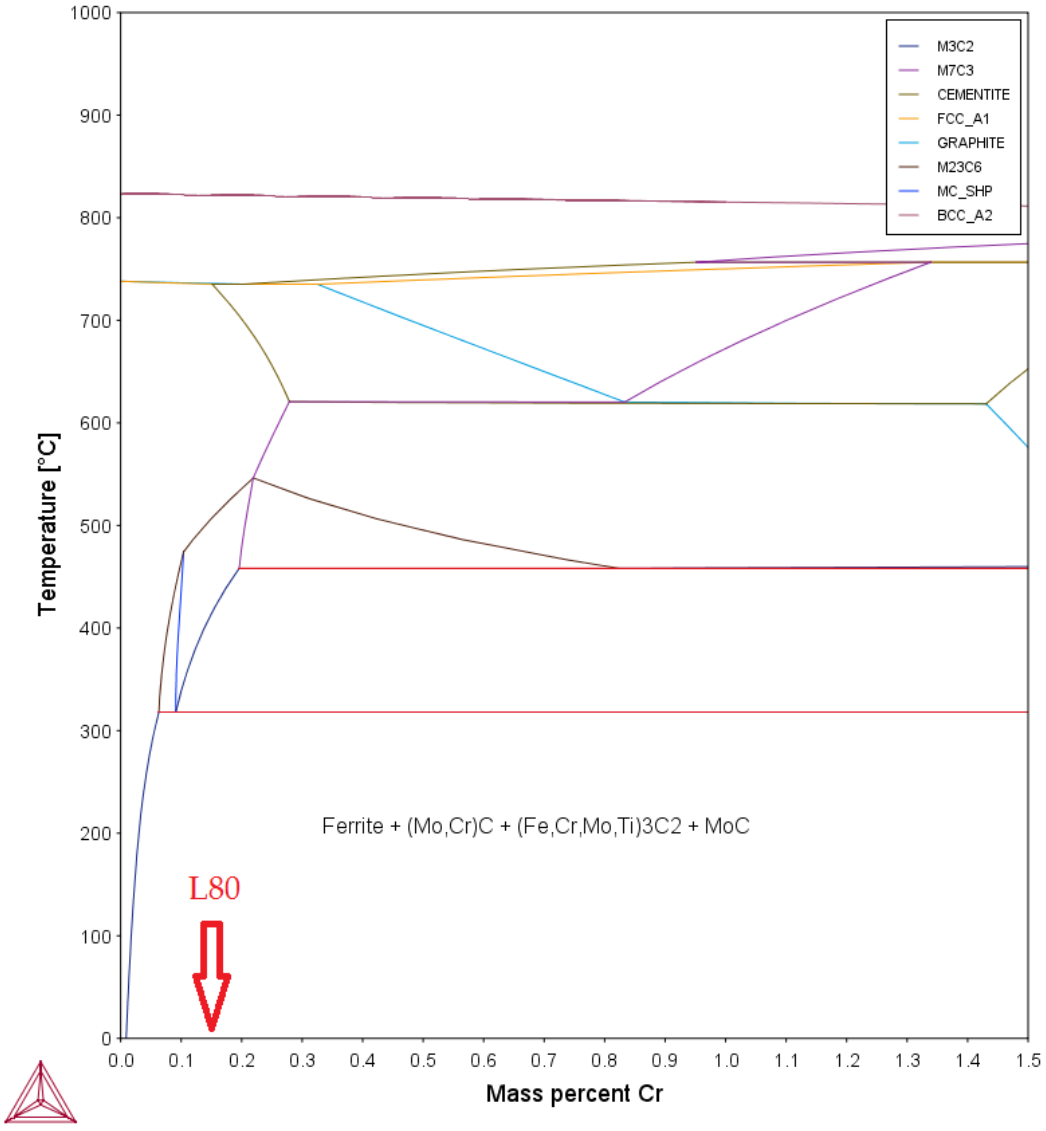


FIG. D.1 – Phase diagram of the system Fe-Mo-Cr-Ti-C calculated with ThermoCalc for L80 steel. L80 Cr composition is 0.14 wt%. For this composition, (Fe,Mo,Cr,Ti)3C2 phase exists. Database : TCFE6.

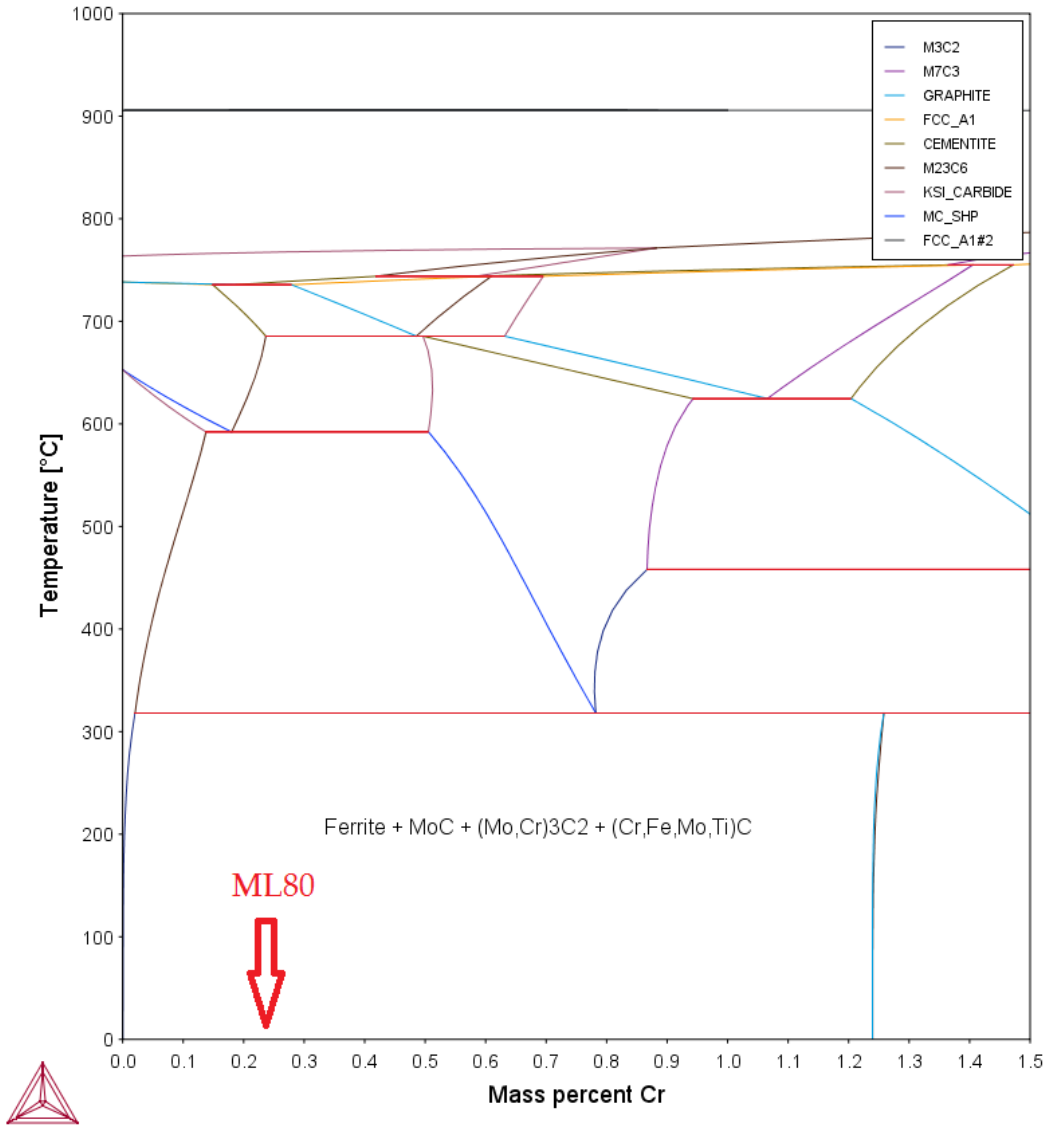


FIG. D.2 – Phase diagram of the system Fe-Mo-Cr-Ti-C calculated with Thermo-Calc for ML80 steel. ML80 Cr composition is 0.22 wt%. For this composition, (Cr,Fe,Mo,Ti)C and (Mo,Cr)3C2 phases exist. Database : TCFE6.

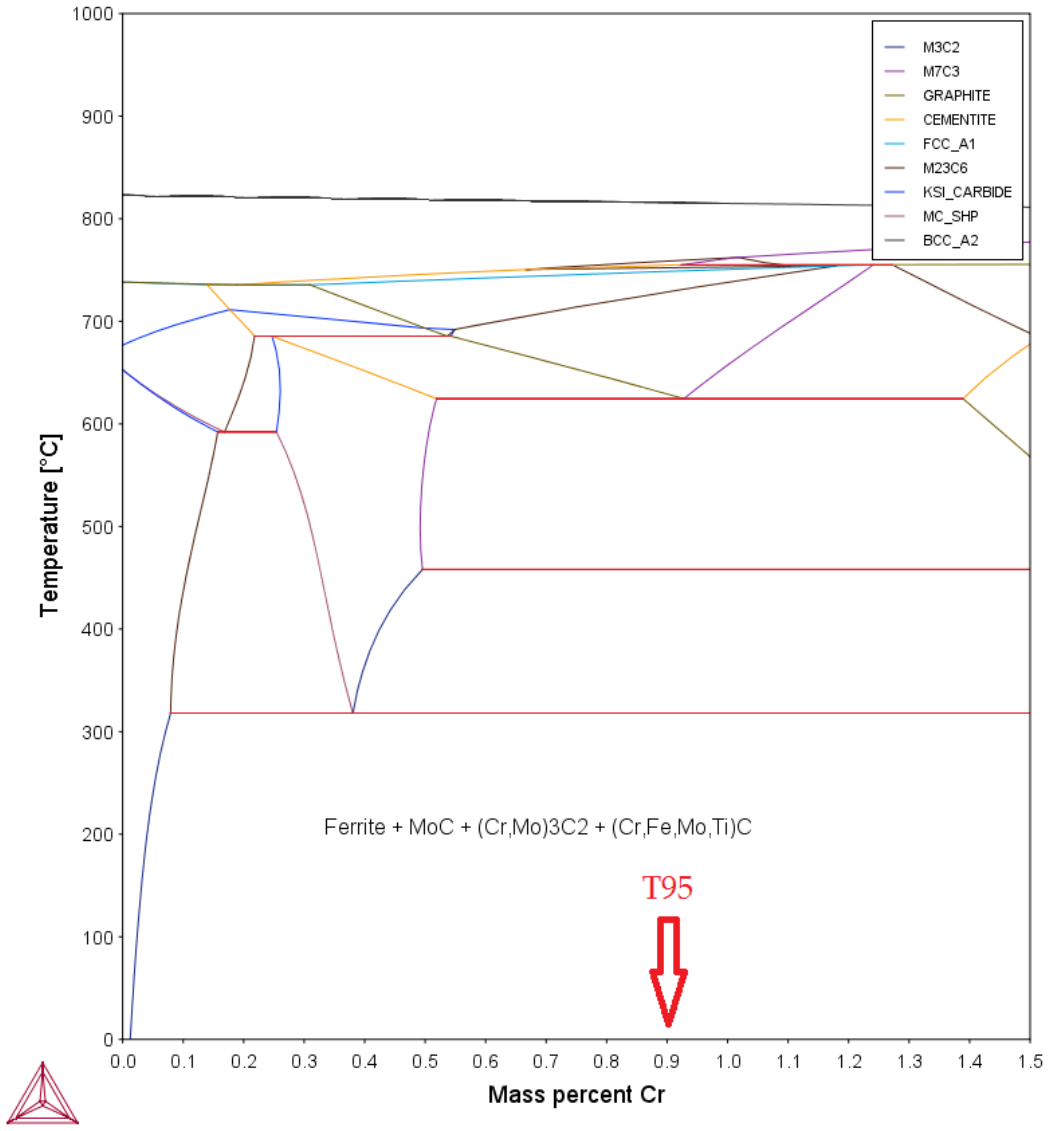


FIG. D.3 – Phase diagram of the system Fe-Mo-Cr-Ti-C calculated with ThermoCalc for T95 steel. T95 Cr composition is 0.9 wt%. For this composition, (Cr,Fe,Mo,Ti)C and (Cr,Mo)3C2 phases exist. Database : TCFE6.